MRI Studies of Appetite Centre Function in Rodents

Mr Nachiket Abhay Nadkarni 00419316

Metabolic and Molecular Imaging Group

MRC Clinical Sciences Centre and Imaging Sciences Department

Imperial College London

A3Z1DC Clinical Medicine Research (Clinical Sciences) MPhil/PhD

Abstract

Many different regions of the brain are involved in appetite control. A full understanding of their function and interaction requires studying neuronal activity at high resolution simultaneously in space and time. Two Magnetic Resonance Imaging (MRI) methods can potentially achieve this goal. Manganese-Enhanced (MEMRI) uses the accumulation of administered Mn^{2+}, which is paramagnetic (hence MRI visible) and taken up by active neurons through voltage-gated Ca^{2+} channels during action potentials. Haemodynamic methods use one or more of many MRI-visible changes that occur to circulating blood in a brain region when it changes activity. These include blood-oxygenation level dependent (BOLD) and cerebral blood volume weighted (CBV) MRI. The aim of this project was to further develop, adapt and then use these methods to study the effects on neuronal activity of stimuli related to appetite and energy balance. The majority of work went towards adapting MEMRI for this. Amongst many tested changes, improvements were made to the MRI acquisition protocol (specifically using fast spin echo rather than spin-echo acquisition) to make it more sensitive to Mn-induced signal changes, increase spatial coverage from partial to whole brain and rostro-caudal spatial resolution from 1 to 0.4mm, all while maintaining the same temporal resolution. Most importantly, the neuroimaging analysis framework used in haemodynamic functional MRI was adapted for use with MEMRI. This included the adaptation of spatial normalization software to handle Mn-sensitive T_1-weighted images dominated by non-brain tissue rather than brain dominated T_2/T_2^*-weighted images, and the generation of a signal change model for use in GLM. This enabled much more objective, reproducible and less laborious data analysis than with previous hand drawn ROIs. Attempts were made to use BOLD- and CBV-fMRI to study the effects of potent, appetite-modulating gut hormones on appetite, though these failed to produce a response.

Contents

Abstract . . . 2

Table of Contents . . . 3

List of Figures . . . 8

List of Tables . . . 11

List of Abbreviations . . . 12

Contributions of Others to this Thesis . . . 15

Acknowledgements . . . 18

1 Introduction **19**

1.1 Brief Overview of Appetite and Energy Balance Regulation . . . 19

1.2 Why Use Magnetic Resonance Imaging Rather Than Other Methods for Brain Activity Measurement in Nuclei Regulating Energy Balance, and Why Use Rodents? . . . 20

1.3 Principles of Magnetic Resonance Imaging . . . 23

1.3.1 Origin of the MR Signal . . . 23

1.3.1.1 Behaviour of Atomic Nuclei with an Intrinsic Angular Momentum and Magnetic Moment in an External Magnetic Field . . . 23

1.3.1.2 Resonance and Continuous Wave NMR . . . 24

1.3.1.3 Pulsed Wave NMR, T_2, $T_2^{'}$ and T_2^* . . . 27

1.3.1.4 Echo Formation . . . 27

1.3.2 Spatial Localization . . . 30

1.3.2.1 Magnetic Field Gradients Can Be Used to Spatially Localise the MR Signal 30

1.3.2.2 Frequency Encoding of Spatial Position 32

1.3.2.3 Phase Encoding of Spatial Frequency 32

1.3.2.4 k-space Representation 33

1.3.3 Other Imaging Considerations 33

1.3.3.1 Repeated Pulse Sequences and T_1 33

1.3.3.2 T_1, T_2 and T_2^* Contrast 35

1.4 Using MRI to Measure Brain Activity 36

1.4.1 Changes That Occur During Neuronal Activity 36

1.4.1.1 Haemodynamic 36

1.4.1.2 Ca^{2+} Channel Opening 36

1.4.2 Detection of Haemodynamic Changes in the Brain 37

1.4.2.1 Bolus Tracking/DSC-MRI 37

1.4.2.2 ASL 39

1.4.2.3 IRON 41

1.4.2.4 BOLD Effect 42

1.4.3 Manganese-Enhanced MRI (MEMRI) is Sensitive to Voltage-Gated Ca^{2+} Channel Opening, and Hence Brain Activity 43

1.4.3.1 Principles of MEMRI 43

1.4.3.2 Manganese Formulation and Toxicity 44

1.4.3.3 Variables in MEMRI Experiments 45

1.4.4 Analysis of Haemodynamic and MEMRI fMRI Data 48

1.5 Overview of fMRI Studies of Energy Balance in Rodents 48

1.6 Aims 49

2 Manganese-Enhanced MRI **50**

2.1 Introduction 50

2.2 Materials and Methods 56

2.2.1 Reagents 56

2.2.2 Non-MR Equipment 56
2.2.3 Animals 57
2.2.4 Metabolic Cage Measurements 57
2.2.5 Static MEMRI Injection Regimen 58
2.2.6 Animal Preparation for MRI 58
2.2.7 MEMRI Acquisitions 58
2.2.7.1 3D gradient-echo timecourses for dynamic MEMRI 59
2.2.7.2 2D fast spin echo timecourses for dynamic MEMRI 59
2.2.7.3 3D gradient-echo for static MEMRI 59
2.2.8 Measurement of Adiposity and Lean Body Mass Using MRS 59
2.2.9 Animal Numbers Used in Infusion MEMRI Experiments 60
2.2.9.1 Optimization of Image Acquisition Protocol 60
2.2.9.2 Effects of Changing Infusion Rate and Duration 60
2.2.9.3 Effects of Adjusting $MnCl_2$ Dose by Lean Mass in Animals of Varying Adiposity 60
2.2.10 MRI Data Analysis 60
2.2.11 Other Statistical Methods 61
2.3 Results 62
2.3.1 Optimization of Image Acquisition Protocol 62
2.3.1.1 3D gradient-echo 62
2.3.1.2 2D fast spin echo 66
2.3.2 Effects of Changing Infusion Rate and Duration 68
2.3.2.1 Continuing the 0.8μmol g^{-1} hr^{-1} $MnCl_2$ Infusion for the Entire Post-Baseline Period Leads to a High Mortality Rate 68
2.3.2.2 Stretching the $MnCl_2$ Dose Across the Entire Post-Baseline Period Leads to Poor Enhancement 69
2.3.3 Effects of Adjusting $MnCl_2$ Dose by Lean Mass in Animals of Varying Adiposity 69
2.3.4 i.p. MEMRI for Appetite Studies is Confounded by Weight Loss 75

2.4 Discussion 79

3 Automated Analysis of MEMRI Data 84

3.1 Introduction 84

3.2 Materials and Methods 87

3.2.1 Spatial Normalization 87

3.2.2 sems Fed/Fasted Data 88

3.2.3 Exploratory Data Analysis for Generation of MEMRI Signal Change Model 89

3.2.4 Other Statistical Analyses 89

3.3 Results 90

3.3.1 Generation of MEMRI Signal Change Model 90

3.3.2 Effect of Spatial Normalization on Analysis of MEMRI Data 93

3.4 Discussion 96

4 Haemodynamic fMRI 102

4.1 Introduction 102

4.2 Materials and Methods 104

4.2.1 Hormones 104

4.2.2 BOLD-Weighted Acquisitions 104

4.2.3 CBV-Weighted Acquisitions 105

4.2.4 Image Analysis 106

4.3 Results 107

4.3.1 BOLD Timecourses Exhibit Substantial Drift, are Noisy and Show No Response to Ghrelin or Exendin-4 Injections 107

4.3.2 N_2O Challenge Does Not Affect CBV-Weighted Signal 110

4.3.3 Ghrelin Injection Does Not Affect CBV-Weighted Signal 112

4.4 Discussion 113

4.4.1 Effects of Protocol Choices on Observing a BOLD Response 114

4.4.2 Factors Influencing Observation of a CBV Response 117

4.4.3 Concluding Remarks 119

5 Overall Discussion and Future Work **121**

5.1 Summary of Developments 121

5.2 Limitations of Methods and Techniques Used 122

5.3 Future Work and Prospects for Animal fMRI 123

References **152**

List of Figures

1.1 basic spin physics 25

1.2 resonance and relaxation 26

1.3 relationships between signal, time and T_2/T_2^* 28

1.4 formation of gradient and spin echoes 29

1.5 slice selection 30

1.6 frequency and phase encoding 31

1.7 k-space 34

1.8 relationships between signal, time and T_1 35

1.9 haemodynamics during basal and stimulated neuronal activity 37

1.10 signals produced by DSC-MRI, CBV-weighted MRI and BOLD 38

1.11 ASL 40

2.1 schematic of dynamic MEMRI protocol 51

2.2 schematic of generic static MEMRI protocol 52

2.3 example data on MEMRI temporal sensitivity 54

2.4 examples of unprocessed single timepoint dynamic MEMRI images acquired using the previous (sems) and two new MR sequences (ge3d, fsems) 63

2.5 t-test map showing differences in enhancement after a 3D gradient echo dynamic MEMRI experiment 65

2.6 uptake and t-test difference maps showing differences in enhancement after a fed-fasted fsems dynamic MEMRI experiment 67

2.7 timecourse of images from ge3d acquisitions with two different $MnCl_2$ infusion rates 70

2.8 effect of high fat diet on dynamic MEMRI experiments 71

2.9 statistical maps and t-tests of fsems dynamic MEMRI comparing Fed, Fasted and *ob/ob* mice 74

2.10 metabolic cage data showing the effect of different doses of $MnCl_2$ administered i.p. 77

2.11 schematic of static MEMRI protocol 77

2.12 body weight changes during the static MEMRI experiment 78

2.13 pre- and post- i.p. $MnCl_2$ images using the static MEMRI protocol 79

3.1 overview of automated data analysis framework 85

3.2 comparison of typical T_2^*-weighted rat BOLD-fMRI and a T_1-weighted MEMRI images 86

3.3 timecourses of signal change over baseline during a MEMRI experiment in various different ROIs 91

3.4 group tensor ICA analysis of dynamic MEMRI data from 29 mice 92

3.5 comparison of a single timepoint sems image to the mean of all the spatially normalised sems timecourses 93

3.6 timecourses of mean group signal change measured manually or automatically on spatially normalised images 94

3.7 statistical maps of a slice through the hypothalamus showing Mn uptake in fed and fasted groups of mice during sems MEMRI 96

4.1 example single timepoint BOLD image 108

4.2 BOLD signal changes in the Arc_LHS of the mouse brain in response to saline, ghrelin or exendin-4 i.p. 109

4.3 location of ROIs used during CBV studies, overlaid onto a pre-injection image. 111

4.4 timecourse of images at a slice through the hypothalamus during a CBV experiment 111

4.5 change in breathing rate during a CBV experiment with N_2O challenge 112

4.6 change in signal in the striatum during a CBV experiment with N_2O challenge . 112

4.7 change in signal in the Arc_LHS during a CBV experiment with either saline or ghrelin administered i.p 113

List of Tables

2.1 comparison of old (sems) and new (ge3d, fsems) acquisition protocols 64

3.1 p-values for various comparisons of data presented in Figure 3.6, calculated using linear mixed-effects modelling 94

List of Abbreviations

4V	4th Ventricle
AD	Alzheimer's Disease
AP	Anterior lobe of the Pituitary Gland
Arc_LHS	Arcuate nucleus of the hypothalamus, Left Hand Side
Arc_RHS	Arcuate nucleus of the hypothalamus, Right Hand Side
ASL	Arterial Spin Labelling
BBB	Blood Brain Barrier
BOLD	Blood Oxygenation Level Dependent
CBF	Cerebral Blood Flow
CCK	Cholecystokinin
CBV	Cerebral Blood Volume
CNR	Contrast to Noise Ratio
CT	Computed Tomography
CW	Continuous Wave
D3V	Dorsal 3rd Ventricle
DC	Direct Current
DSC	Dynamic Susceptibility Contrast
EDA	Exploratory Data Analysis
e.m.f.	Electromagnetic Force
EPI	Echo Planar Imaging
FE	Frequency Encode
FID	Free Induction Decay
fMRI	Functional MRI
FOV	Field of View
FSE	Fast Spin Echo
FWHM	Full Width Half Maximum
GE	Gradient-Echo
GLM	General Linear Model

i.a	intraarterial
IBBB	Inside the BBB
IC	Independent Component
ICA	Independent Component Analysis
i.p.	intraperitoneal
IRON	Increased Relaxation with iron Oxide Nanoparticles
i.v.	intravenous
IVC	Individually Ventilated Cage
LD	Light-Day
LDPE	Low Density Polyethene
ME	Median Eminence
MEMRI	Manganese Enhanced MRI
MRI	Magnetic Resonance Imaging
MRS	Magnetic Resonance Spectroscopy
NMR	Nuclear Magnetic Resonance
OBBB	Outside the BBB
PE	Phase Encode
Pe_LHS	Periventricular Nucleus of the hypothalamus, Left Hand Side
Pe_RHS	Periventricular Nucleus of the hypothalamus, Right Hand Side
PET	Positron Emission Tomography
phMRI	Pharmacological MRI
PICA	Probabilistic ICA
PVN_LHS	Paraventricular Nucleus of the hypothalamus, Left Hand Side
PVN_RHS	Paraventricular Nucleus of the hypothalamus, Right Hand Side
PYY	Peptide YY
rCBF	Relative CBF
rCBV	Relative CBV
RF	Radio Frequency
RMS	Root Mean Square

ROI	Region of Interest
s.c.	subcutaneous
SE	Spin-Echo
SEM	Standard Error of the Mean
SI	Signal Intensity
SNR	Signal to Noise Ratio
SPECT	Single Photon Emission Computed Tomography
SPIO	Small Paramagnetic Iron Oxide
TE	Time to Echo
TEeff	Effective Time to Echo
TR	Time to Repetition
USPIO	Ultra Small Paramagnetic Iron Oxide
VASO	Vascular Space Occupancy
VMH_LHS	Ventromedial nucleus of the Hypothalamus, Left Hand Side
VMH_RHS	Ventromedial nucleus of the Hypothalamus, Right Hand Side

Contributions of Others to this Thesis

All raw data acquisition, data analysis, interpretation, writing and figure design was that of the candidate, with the following few exceptions (note that in each case there is an acknowledgement of the contributions of others in the figure itself too):

Figure 1.9 on page 37 demonstrating how haemodynamic changes affect the MR signal was inspired by that of Peter Jezzard (http://www.fmrib.ox.ac.uk/education/fmri/brief-introduction-to-fmri-physiology).

The data in Figure 2.3 on page 54 comparing the temporal sensitivity of CBV (cerebral blood volume) measurements to those from MEMRI (Manganese-Enhanced MRI) experiments both with and without BBB (blood-brain barrier) compromise was derived from 3 studies published elsewhere (Kuo et al., 2007; Morita et al., 2002; Schwarz et al., 2003).

Some of the raw data (the 4 sems animals) in Figure 2.4 on page 63 used to demonstrate the image quality differences between the sems, ge3d and fsems acquisition protocols was kindly provided by Owais Chaudhri.

The raw data for Figure 2.8 on page 71 used to demonstrate the effect of high fat feeding on the MEMRI signal was kindly provided by Jelena Anastasovska (the 17 animals used here were part of a separate dietary study, separate to that in Figure 3.4 on page 92).

The raw data for Figure 2.9 on page 74 used to demonstrate the effect on the MEMRI signal of dosing $MnCl_2$ by lean mass in fed, fasted and *ob/ob* mice was partially collected by Mohammed Hankir (9/30 animals).

The raw data, analysis and graphs contributing to Figure 2.10 on page 77 (a study demonstrating the effect of different i.p. (intraperitoneal) $MnCl_2$ doses on mouse behaviour) was collected and performed by Jim Parkinson.

The raw data in Figure 3.4 on page 92, which uses 29 animals from a separate dietary study (a different one to that in Figure 2.8 on page 71) to generate MEMRI MELODIC components, was kindly provided by Jelena Anastasovska.

The raw data in Figure 3.3 on page 91 which shows MEMRI timecourses in a single mouse, background images in Figure 3.5 on page 93, timecourses and p-values in Figure 3.6 on page 94 and Table 3.1 on page 94 respectively showing the effect of spatial normalisation on ROI data, and the statistical maps in Figure 3.7 on page 96 were based on raw data kindly provided by Yu-Ting Kuo. As mentioned in the section where this data appears (page 93), this data is a reanalysis of previously reported data (Kuo et al., 2006).

In summary, with the exception of Figure 1.9 on page 37, Figure 2.3 on page 54 and Figure 2.10 on page 77, all data analysis, interpretation, writing and figure design (including the MR physics figures in the introduction) is the original work of the candidate.

With respect to raw data, a total of 187 animals contributed data to this thesis, with the candidate performing experiments on just over half.

The candidate performed experiments on 95 animals:

8/12 for comparing sems, ge3d and fsems acquisition protocols (Figure 2.4)
9 to the ge3d fed vs fasted experiment (Figure 2.5)
8 to $MnCl_2$ dose profile change testing (Section 2.3.2)
5 *ob/ob* mice dosed by whole body mass (Section 2.3.3
21/30 for the effects of dosing $MnCl_2$ by lean mass on fed, fasted and *ob/ob* mice (Figure 2.9)
13 for testing i.p. MEMRI in the context of a saline vs ghrelin experiment (Figures 2.13 and 2.12)
16 for BOLD measures of saline vs ghrelin vs exendin-4 (Figure 4.2)

3 for CBV measures with an N_2O challenge (Figures 4.5 and 4.6)
6 for CBV measures with saline and ghrelin challenges (Figure 4.7)
6 used for informally testing the anaesthetics medetomidine and saffan (Section 4.4.1)

24 animals were used by Jim Parkinson for testing different i.p. $MnCl_2$ doses on behaviour (Figure 2.10).

68 were primarily used by others as parts of other studies- 4 by Owais Chaudhri (partial contribution to Figure 2.4) and 9 each by Mohammed Hankir and Yu-Ting Kuo (partial contribution to Figure 2.9 and full contribution to Figures 3.3, 3.5 and 3.7 respectively) for fed vs fasted studies, plus 17 and 29 from separate dietary studies by Jelena Anastasovska (Figure 2.8 and Figure 2.8).

Acknowledgements

I have been given an unusually large amount of freedom during this PhD and for that I am deeply indebted to my supervisors Prof Jimmy Bell and Dr Amy Herlihy for having so much faith despite all the long stretches where very little, if anything, was happening.

Many people have given invaluable advice and assistance, in particular Anthony Price, Benito de Celis Alonso, Po-Wah So, Phil Muckett, Marzena Wylezinska Arridge, Willy Gsell and Tony Goldstone.

I also wish to thank everyone in the Metabolic and Molecular Imaging Group and the Biological Imaging Centre for providing such a great environment to work in. Especially anyone who had to share an office during the extensive bouts of stress, swearing, screaming and shouting.

Chapter 1

Introduction

1.1 Brief Overview of Appetite and Energy Balance Regulation

A sense of appetite is one of the basic functions possessed by all higher organisms. It is normally very accurate at matching energy intake to expenditure, operating in humans with an accuracy of >99.5% (Friedman, 2004). This stringency is required as just a small defect in our mechanisms of energy balance can cause a huge cumulative increase in body mass over time, leading to obesity and its related metabolic disorders. These are major public health problems, that at a conservative estimate consume 2-7% of total healthcare costs in developed countries (World Health Organisation, 2004). In England in 2004, 38.9% of adults were overweight and 23% obese (Department of Health, 2004), with the percentage of obese predicted to rise to 31% by 2010 (Zaninotto et al., 2006). This economic burden gives extra impetus to resolving questions surrounding the mechanisms of appetite and energy expenditure regulation, on top of their importance to basic biological function.

Observations and experiments dating back to the end of the 19th century, mainly the effect of pituitary tumours in humans and lesion experiments in rats, determined that energy balance was regulated in the hypothalamus of the brain (Elmquist et al., 1999). This initial discovery has since been developed into a modern view of multiple interconnected brain nuclei, mostly in the hypothalamus but also in other areas such as the brainstem, each with a characteristic pattern of receptor and neurotransmitter expression and innervation. The hypothalamus and brainstem receive many inputs from around the body, indicating energy status, and integrate these with information from higher centres of the brain. The flow of information continues to the reward centres, and so the feelings and behaviours of appetite are generated (Wynne et al., 2005).

The energy status inputs can be divided into those from the gut, and those from the energy depots (Morton et al., 2006). The gut signals are comprised of peptide hormones released from different parts of the gut as the food bolus moves through the different sections, e.g. ghrelin from the stomach (Kojima and Kangawa, 2005), CCK mainly from the duodenum and jejunum (Raybould, 2007), PYY mainly from the ileum, colon and rectum (Wynne and Bloom, 2006) and neuronal signals carried via the vagus nerve, many of which are triggered by the actions of gut peptides (Wynne et al., 2005). These provide information relating to the nutritional content and location of the bolus (Huda et al., 2006). Energy depot signals are primarily the hormones leptin and insulin, indicating to the brain the levels of adipose fat (Trayhurn and Bing, 2006). Blood-borne nutrients, most notably free fatty acids (Lam et al., 2005) and glucose (Burdakov et al., 2005) can also act directly on the hypothalamus.

1.2 Why Use Magnetic Resonance Imaging Rather Than Other Methods for Brain Activity Measurement in Nuclei Regulating Energy Balance, and Why Use Rodents?

A wide range of potentially cheaper, more direct and less invasive techniques are available for monitoring brain activity involved in energy balance, so some justification is needed for the use of only MRI in these studies.

The physical connections amongst the appetite centres, and their known role (based on lesion experiments) in appetite regulation imply that all are in some way involved in the response to appetite-related stimuli. However, very little is known about how the centres interact over time following a stimulus, such as elevated levels of a gut hormone. This problem is a consequence of the technologies currently used to study the neurobiology of appetite regulation. With a few exceptions, these are either immunohistochemistry of thin brains sections, or electrophysiology of either thick slice preparations or an intact brain.

Immunohistochemistry, though of high spatial resolution and coverage, provides only a single time point per animal, and its traditional reporter of neuronal activation, c-Fos protein, has a complex temporal profile that takes 90 minutes to peak (Hoffman et al., 1993a,b).

The most direct method of studying brain activity in live animals is using surgically implanted electrodes to record the electrical activity of neurons. Various elaborations on this technique can differentiate between the neurotransmitters being used, single and multiple cells, different depths along the electrode and multiple locations if using wire bundles (Kleinfeld and Griesbeck, 2005; Lin et al., 2006). Although electrode recording is the method that is best able to characterise brain activity, it does have a number of disadvantages for some kinds of study, including those of the nuclei regulating energy balance. These nuclei are mostly ventral and circumventricular, making electrode implantation in even just one area technically difficult. Additionally, they are distributed over several parts of the brain. A full understanding of their operation requires simultaneous observation of all, which would involve implanting more electrodes than is practically possible.

These limitations can only be overcome through the use of brain imaging technologies. Although several are available, many, such as magnetoencephalography (Lounasmaa et al., 1996) and optical tomography (Hielscher, 2005) are inappropriate since they have limited depth penetration, which precludes them from studying the highly ventral appetite centres. In addition most of the equipment currently available is limited to human-sized brains.

The only technologies with a depth penetration reaching the ventral side of the rodent brain, and which can detect changes in brain activity, are Magnetic Resonance Imaging (MRI), PET (Positron Emission Tomography) and SPECT (Single Photon Emission Computed Tomography) (van Bruggen and Roberts, 2002). All three detect neuronal activity indirectly. In brief, PET detects the emission of positrons from a radionucleotide. For neuronal activation studies, this is usually ^{18}F-fluorodeoxyglucose, whose uptake in different brain regions is proportional to the metabolic activity of those regions' neurons, itself proportional to neural activity. It is then inferred that areas accumulating more ^{18}F-FDG under an experimental stimulation are activated during that stimulation. SPECT also uses radionucleotides, but those that emit gamma rays. For functional brain studies this involves ^{99}Tc-hexamethylpropylene amine oxime (^{99}Tc-HMPAO). This substance is not taken up by neurons, but instead marks cerebral blood volume. This is also proportional to neuronal activity, though less directly than metabolic rate. Finally there is MRI, which uses a powerful external magnetic field and radiofrequency pulses to detect the presence of various chemical elements, usually hydrogen in water and fat. For studying neural activity, MRI experiments usually operate on a similar idea to SPECT, with haemodynamics taken as a proxy for neuronal activity (van Bruggen and Roberts, 2002). When using MRI there are alternatives to haemodynamics, such as detection of administered manganese (whose paramagnetism affects the MR signal), which is taken up by active neurons via voltage-gated Ca^{2+} channels (Silva et al., 2004).

The study of appetite places a number of constraints that determine which of these technologies can be used, and with what models. Hunger is a feeling that develops over a period of hours. This rules out using these technologies to study the timecourse of hunger development in humans, since all three require the subject to stay still in a claustrophobic environment. In addition the radiation exposure (when using PET and SPECT) from the large doses of tracer required for several hours of imaging is unacceptable. Also, the small size of the human hypothalamus and proximity to air cavities make its activity difficult to detect by MRI. Instead, it is more appropriate to use rodents, which are well characterised models in the study of mammalian energy balance (the caveat being that for imaging experiments the animals must be anaesthetised, blunting neuronal responses).

Through a mixture of positional cloning in obese mutants and knockouts of putative satiety genes, mice have provided extensive knowledge of the genes underlying appetite control (Butler and Cone, 2001). Rats are the source of much of our knowledge of appetite physiology, and were the platform for the discovery of many satiety hormones such as ghrelin (Kojima et al., 1999; Tschöp et al., 2000) and the orexins (Sakurai et al., 1998). Many of these proteins have since been shown to have analogous effects in humans (Wynne et al., 2005), e.g. leptin (Farooqi et al., 1999; Licinio et al., 2004; Montague et al., 1997; Strobel et al., 1998) and the melanocortin-4 receptor (Vaisse et al., 1998; Yeo et al., 1998). This does not mean imaging studies are not possible in humans- but they are more likely to involve stimuli of the primary senses, and reward tasks (Goldstone, 2006; Kringelbach, 2004). For studies of more autonomic processes such as the effect of gut hormones, rodents are more appropriate models since it is here that these processes were discovered and are best characterised.

In humans the hypothalamic and brainstem nuclei are much smaller than the cerebral regions typically studied by functional neuroimaging. This situation is less extreme in rodents, where the hypothalamus and brainstem are relatively larger, but is still important (Paxinos and Franklin, 2004). The spatial resolution of PET and SPECT are inherently limited to around 500μm, too small to resolve individual appetite centres in rodents. This rules them out in favour of MRI, whose spatial resolution has a practical limit of less than 100μm.

In conclusion, to study the neurobiology of appetite regulation and energy balance, there is a need to implement technologies that can observe whole brain neuronal activity at high temporal and spatial resolution, and the most appropriate available is MRI.

1.3 Principles of Magnetic Resonance Imaging

1.3.1 Origin of the MR Signal

1.3.1.1 Behaviour of Atomic Nuclei with an Intrinsic Angular Momentum and Magnetic Moment in an External Magnetic Field

MRI is a spatially resolved form of nuclear magnetic resonance spectroscopy. NMR exploits a finding of quantum mechanics that some elementary particles have an intrinsic angular momentum- they *spin*. As a consequence, all nuclei with odd numbers of either protons, neutrons, or both, also spin. ^{1}H is the most abundant of these nuclei occurring in the environment and in biological organisms, and so is also the most exploited nucleus in NMR-based methods (McRobbie et al., 2003, note that the majority of information in this section is derived from this reference and references therein).

Atomic nuclei are positively charged- they contain only positive charges (protons) and neutrons, with no negatively charged particles to make the nucleus electrically neutral.

Therefore spinning atomic nuclei (‘spins’) are moving charges, and as with all moving charges possess a magnetic moment. When placed in an external static magnetic field (B_0), these magnetic spins will respond by aligning their poles to match those of B_0, and precess about the B_0 field lines at a frequency (known as the larmor frequency) dependent on the strength of B_0 (Figure 1.1A+B). This is known as the parallel state. At temperatures $>0K$, the presence of thermal energy can excite/flip the spins to a higher energy state where they precess with poles aligned opposite to the field- the antiparallel state (Figure 1.1C). In the presence of a B_0 field and a number of other fixed conditions including $T>0K$, a group of spins (known as a spin packet) will reach an equilibrium where at any one time a majority of its members are parallel to B_0 (Figure 1.1D). The excess of parallel spins means the spin packet possesses its own net magnetic field (M_0) in the direction of B_0. The proportion of spins in the antiparallel state rises with temperature, tending to a ratio of 1:1 (Figure 1.1E). Note that when using the xyz co-ordinate system B_0 is by convention in the z-axis.

Spin energy does not vary with phase angle about B_0. At any one time it is highly unlikely any two spins will have the same phase about their axes. Therefore if the spin packet’s individual members’ magnetic vectors were all represented, they would fan out to appear as a larger (parallel) and smaller (anti-parallel) cone joined at their apices (Figure 1.1F).

1.3.1.2 Resonance and Continuous Wave NMR

In NMR spectroscopy, radiofrequency (RF) waves emitted by an RF coil are used to manipulate M_0. The response of M_0 (detected as an electromotive force, or e.m.f., on the RF coil) is dependent on- and therefore provides information about- its molecular environment. The simplest NMR method involves varying the frequency of a continuous wave (CW) of RF energy at a fixed B_0. The application of RF energy creates a second magnetic field, B_1, that rotates about the sample being analysed at the frequency of the CW. Normally the weakness and rotation of B_1 means it has little interaction with the sample. However, when the CW reaches the larmor frequency, the B_1 rotation matches the larmor frequency of the sample. This matching causes the spins to begin interacting with B_1- they precess about it (Figure 1.2A). This is the resonance condition referred to in the terms NMR and MRI. Since B_1 is relatively weak,

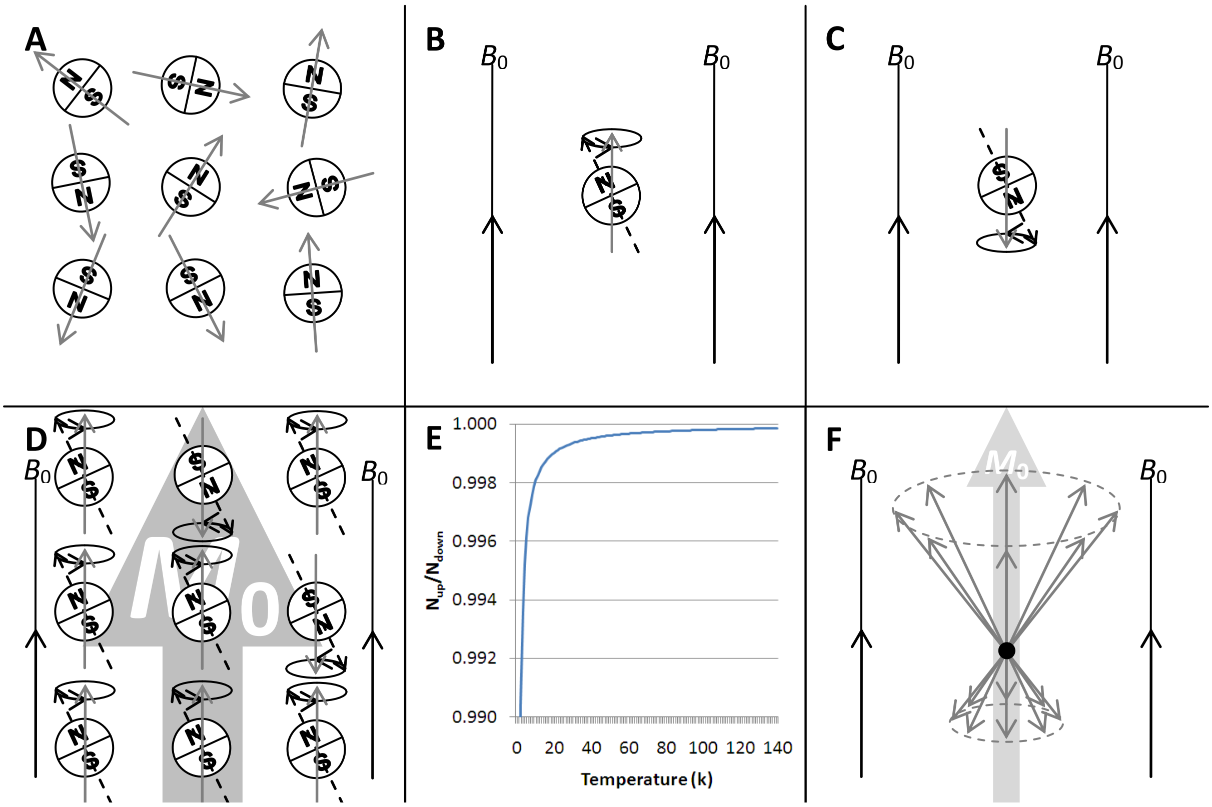

Figure 1.1: basic spin physics. In the absence of an external magnetic field, nuclear particles possessing a magnetic moment (spins) are randomly oriented, so there is no net magnetic field produced by them (A). When an external field is applied (B_0), any given particle will align with the field and precess about its field lines- overall the magnetic moment is aligned with B_0, but at any one moment in time the vector is rotating at an angle (B). In the presence of thermal energy, spins may also align against the field in a higher energy (anti-parallel) state (C). At a population level (a spin packet), there will always be more parallel than anti-parallel spins, resulting in a net magnetic moment (M_0) from the sample- the sample is magnetised (D). The proportion of parallel:anti-parallel spins is 1:0 at absolute zero, but rises rapidly towards 1:1 with increasing temperature. At room temperature, the excess of parallel spins is tiny, hence M_0 is very small (E). At any one moment in time the precession of spins' magnetic vectors in a spin packet appears as two cones joined at their apices, with the parallel cone possessing a bigger moment (F).

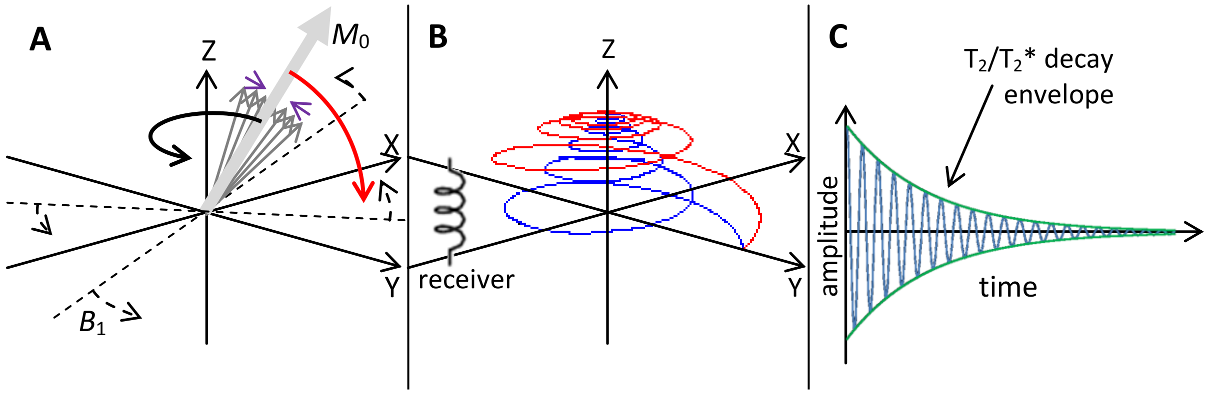

Figure 1.2: resonance and relaxation. In the presence of a weak second external magnetic field (B_1) rotating in the x-y plane, the spins making up M_0 begin to simultaneously cohere and precess (resonate) with B_1 (at a much lower frequency than B_0; A). If the tip of M_0 is traced, it appears as a spherical spiral down towards the x-y plane (B; red line). If B_1 was continued, this would continue down to the -z axis. If ceased after a 90° rotation, M_0 spirals back up (relaxes) with an exponential decay (B; blue line). This relaxation behaviour can be detected by an external receiver (C). The decay is a consequence of dephasing of the cohered spins due to spin-spin interactions (T_2 processes) and field inhomogeneity ($T_2^{'}$, usually combined with T_2 to form the composite process T_2^{*}).

this precession is much slower than that about B_0. These effects combine to make the spins cohere from a cone into a single vector 90° out of phase with the B_1 field, spiralling into the x-y plane and then the -z axis before spiralling back to +z again (Figure 1.2B). This movement of M_0 can be detected as an e.m.f. on the RF coil.

The electrons surrounding a nucleus partially shield against B_0. Different chemical groups provide different levels of shielding. This creates a chemical shift of the larmor frequency in the affected nuclei. By sweeping the CW frequency across a wide enough range, a signal spectrum of absorbance is acquired containing this chemical shift information, which can be used to deduce the molecular structure of sample contents. This type of experiment tends to only be done for one type of nucleus at a time, e.g. ^{1}H. The same principle can be used for other nuclei with net spin, e.g. ^{13}C. Simultaneous multinuclear experiments tend not to be performed since the bandwidth required to cope with the different larmor frequencies would be too large for a single set of hardware to handle.

1.3.1.3 Pulsed Wave NMR, T_2, $T_2^{'}$ and T_2^*

For imaging, CW NMR is too slow. It also provides a complex noisy signal with more information about the sample than is often required. It would be better to have some method that produced a large simple signal quickly.

A different form of NMR that achieves this uses a train of discrete RF pulses, or pulse sequence, to manipulate M_0. The simplest pulse sequence is the 90°-FID sequence. This single RF pulse is the same as a CW but calibrated to be applied only for the time required to bring M_0 into the x-y plane (hence 90° in the title). M_0 does not necessarily become zero in z at the same time the spins finish cohering and reach a 90° rotation about B_1; a situation is merely reached where the balance of magnetizations results in a net M_0 vector rotating about z in the x-y plane. The recovery from this situation involves the line tipping back towards the z-axis and spreading out into a cone. The spreading out of M_0 while it spirals back to alignment with B_0 appears to the RF coil as an oscillating exponential decay (Figure 1.2C). This signal is a free induction decay (FID), hence the term 90°-FID. Two factors known as T_2 and $T_2^{'}$ relaxation contribute to the decay process and hence the shape of the FID. T_2 processes influence the decay of x-y plane magnetization through spin-spin interactions that dephase M_0. T_2 is defined as the time required for the x-y component of M_0 to drop by a factor of e^{-1} (approximately 0.37) of its original magnitude after its initial excitation. $T_2^{'}$ refers to a mixture of many other factors including B_0 inhomogeneity that can further increase the dephasing. Instead of being described on its own, it is usually combined with T_2 to form the composite parameter T_2^*, whose time definition is of the same form as T_2. The relationship between signal, time and T_2/T_2^* is shown in Figure 1.3A.

1.3.1.4 Echo Formation

After the application of an RF pulse, the simplest method of data collection involves just recording the FID. However, substantial time is required after excitation to apply the magnetic field gradients used for spatial localization (discussed later). This means FID acquisition would occur after a significant amount of decay. To avoid this loss, we could rephase the spins and recover a larger signal to form what is known as an echo. There are two methods to form an

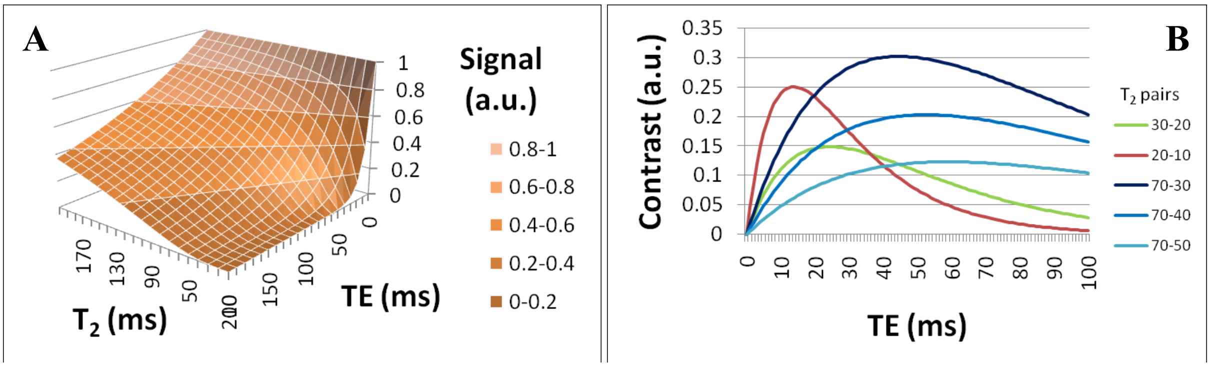

Figure 1.3: relationships between signal, time and T_2/T_2^*, as determined by the equation $signal \propto e^{-TE/T_2)}$. The absolute relationship is shown in graph A: lower TE and longer T_2/T_2^* results in a larger signal. Contrast behaviour between two materials with different T_2/T_2^* values is more complex, however (see B). In general, bigger differences between the T_2 values being contrasted gives greater signal contrast (compare 70-30 to 70-40 and 70-50), but for a given difference in T_2 lower T_2 values produce greater contrast, due to the larger signals being contrasted (compare 20-10 with 30-20, both differences in T_2 of 10ms).

echo: gradient-echo (GE), in which the spins are rephased using gradients, and spin-echo (SE) in which this is done using an RF pulse (Figure 1.4).

For GE a gradient is applied to deliberately dephase the spins, and then an opposite one to rephase and dephase them again. The initial deliberate dephasing may seem illogical, but it allows the encoding frequencies to efficiently occupy the full extent of the receiver's bandwidth. The point of maximum rephase is at the centre of the echo. There will never be total rephasing due to T_2^* effects (hence GE sequences are T_2^* sensitive). Data is collected in a window extending either side of the echo centre.

SE uses an RF pulse to rotate dephased spins by 180°, causing their directions to reverse, again resulting in an initial rephasing then dephasing. Like with GE, a dephasing gradient is often applied before the rephasing stage to aid spatial localization. Unlike with GE, the effects of decay due to field inhomogeneity are eliminated since the spins' directions are reversed back upon themselves, so SE is sensitive to T_2 effects rather than T_2^*.

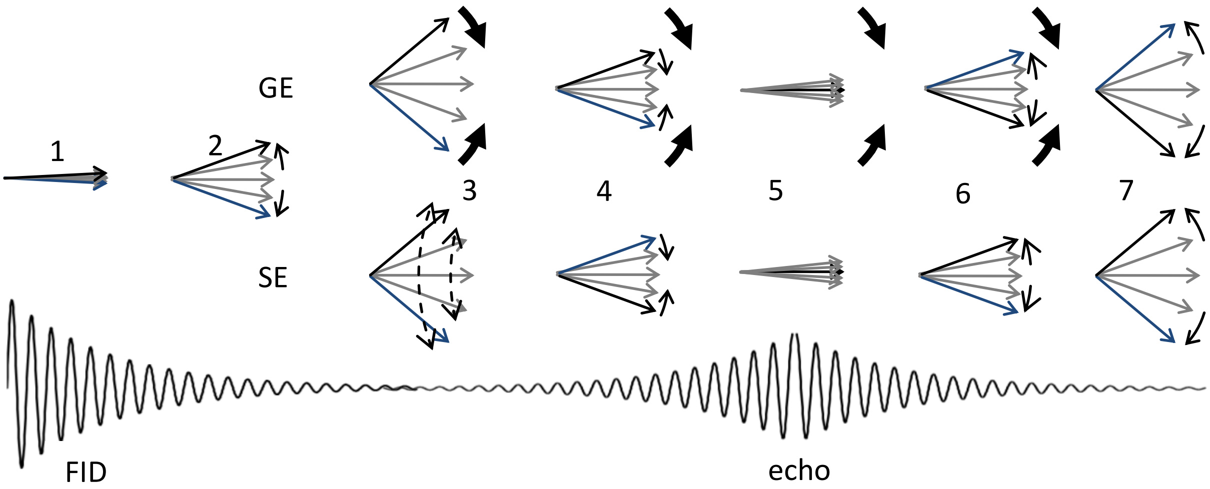

Figure 1.4: formation of gradient and spin echoes. Time proceeds from left to right. After excitation the spins (1) initially dephase (2), forming the FID which is not recorded (often during this time the phase encoding gradient described in Figure 1.6 is being applied, and this would dominate the received signal). Either using gradients (3-6, GE) or by applying a 180° pulse to invert/swap the order of the dephasing spins (fastest now last and slowest now first; 3, SE) the spins rephase (4; note how the leading and trailing arrow colours are swapped for SE compared to GE due to the inversion). The rephasing increases the strength of the magnetic moment of the spin packet, producing a measurable echo that eventually peaks (though more weakly than the FID; 5) before dephasing and decaying again (6-7). The inversion used in SE causes $T_2^{'}$ effects to cancel each other out, hence SE is influenced by T_2 decay only. GE is influenced by T_2^*.

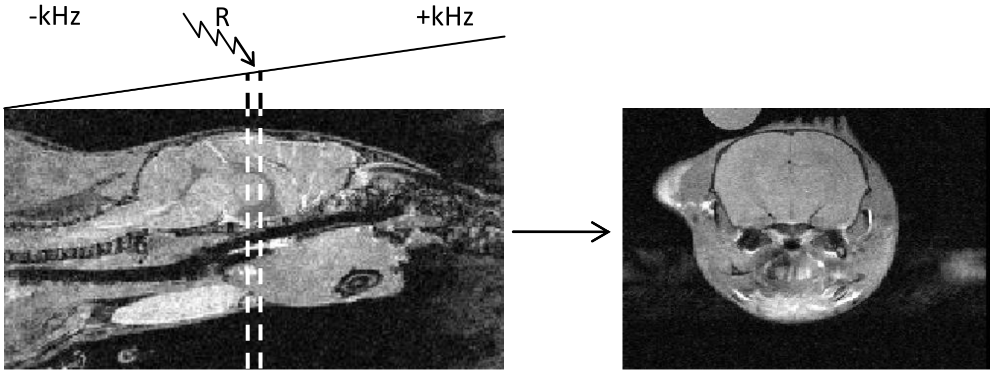

Figure 1.5: slice selection. Applying a magnetic field gradient during excitation means that only the spins in a thin slice of the object will be at the correct field strength and hence precessing at the correct frequency to match that of (and hence resonate with) the applied RF pulse. Hence only those spins will produce a signal, and in this way slice selection allows spatial resolution in one dimension.

1.3.2 Spatial Localization

1.3.2.1 Magnetic Field Gradients Can Be Used to Spatially Localise the MR Signal

Most imaging techniques (e.g. confocal microscopy, X-ray CT) acquire data points that originate in specific regions of the object. Knowledge of which signal came from which region can then be used to reconstruct the object as an image. This is difficult in MRI since the MR signal is dependent on an RF excitation that cannot be directed to a point in space. What we can do is sensitise discrete regions of space in the imaged object to the RF excitation, such that only those sensitised parts respond with an e.m.f.

Since the MR signal is dependent on the RF pulse matching the magnetic field strength, we can use a magnetic field gradient briefly applied on top of B_0 to achieve selective sensitization of a slice of the object, as shown in Figure 1.5. This technique of slice selection is used extensively in MRI to spatially localise or encode the MRI signal in one dimension. However, acquiring every point in a 3D object this way would be extremely slow, so other methods are needed.

After the application of a 90°-pulse, the spins underlying M_0 have two properties that could somehow be manipulated to aid spatially localising spin packets in each of the other two dimensions not spatially encoded by slice selection. These are the frequency and phase of precession. Magnetic field gradients, on top of their role in slice selection, can also manipulate frequency and phase, as shown in Figure 1.6A-C. Looking at the figure, it is difficult to conceive

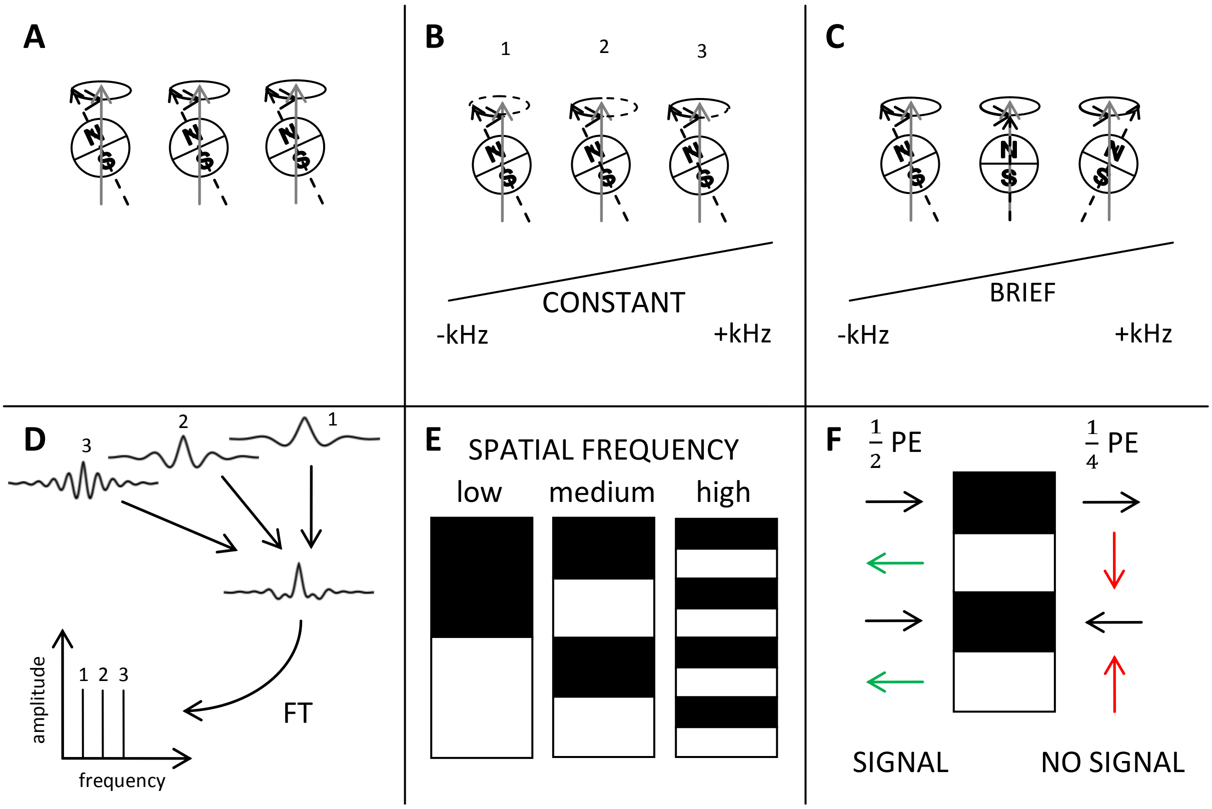

Figure 1.6: frequency and phase encoding (FE and PE). Spins (A) have two properties than can be manipulated to create spatial resolution: precession frequency (B) altered by the constant application of a magnetic field gradient (resulting in a gradient of B_0 and hence a gradient of larmor frequencies), and precession phase (C) altered by a brief application, further causing a brief gradient in larmor frequency, hence sending spins out of phase with each other depending upon their location. Spins at different frequencies (B1-3) produce echoes at different frequencies (D1-3), detected as a single spectrum. A fourier transform can separate these frequency components to uncover the original signals (D), whose frequencies correspond to their spatial location. PE is dependent on how spin phase interacts with the underlying spatial frequency of an object. Spatial frequency is described by the line pair objects in E- it is the frequency with which regular patterns repeat across space. In this example, white represents regions made up of matter with spins (e.g. water), black those made up of matter without any (e.g. air). Any object can be considered to be made up of a mixture of such patterns. The principle of PE is demonstrated in F using a medium frequency line-pair object If spins are given 1/2 PE, the two regions producing signal are in phase and the signal is additive. If spins are given 1/4, the two regions produce signal of opposite phase that are destructive. In this way, by applying many different levels of phase encoding, the spatial structure of an object can be determined.

exactly how frequency (FE) and phase encoding (PE) of the spin packets' locations could lead to an image- different parts of the object now have different spin states (and so are in a sense spatially encoded), but how do these affect the MR signal and can these effects be used to derive information about the object? With careful manipulation both FE and PE of MR signals can be used in combination with each other, on their own and (in both cases) even absent of slice selection to acquire 3D information about objects.

1.3.2.2 Frequency Encoding of Spatial Position

In FE, as can be seen in Figure 1.6C, a gradient of different larmor frequencies is created across the object. Since spin packets oscillate at the larmor frequency, the signals produced by them now exist in different frequency bands corresponding to their position along the gradient. Modern RF equipment is capable of recording the e.m.f. from all these bands simultaneously. The resulting spectrum is a mixture of several different frequency bands representing spin packet signals from different locations (Figure 1.6D). These bands can be resolved by the fourier transform, a mathematical operation that can separate the individual members of a mixture of sinusoidal waves, and in this way FE can be used to spatially localise the MR signal in one dimension.

1.3.2.3 Phase Encoding of Spatial Frequency

The operation of PE is less obvious. Signals from the different positions along the PE gradient will be phase-offset with each other, so phase could indicate location. However, these different phases cannot be readily isolated by the RF detection equipment.

Instead, the effect of spatial frequency on the PE signal is used. To understand how this works we need to consider what a spatial frequency is. The simplest example of an object with uniform spatial frequency is an x-ray line-pair object (Figure 1.6E). Line-pair objects have increased spatial frequency if there is an increase in the frequency of switching from dark to light bands as we move across the line-pair object, and vice-versa. Thus spatial frequency is a measure of how often a structure is repeated over space. A complex image can be considered to be made up of several simpler spatial frequency components (e.g. bands similar to those in a l.p.o). The mechanism by which PE detects spatial frequency is shown in Figure 1.6F. Light regions represent tissues that produce a signal of large amplitude, and dark regions the opposite. If the spatial frequency in the object matches the level of PE, the signal will be large; if not, it will be small. Thus the application of several levels of PE can be used to acquire information on the presence of several different spatial frequencies in an object. The same fourier transform used for FE data can then be used to reconstruct the 1D projection along the PE direction from this raw spatial frequency data.

This is an inherently slow process since rather than applying a gradient once (like with FE) and recording all the necessary data in one readout window, the PE has to be done multiple times, with a corresponding increase in scan duration.

1.3.2.4 k-space Representation

Both FE and PE signals are converted to spatial locations using the fourier transform. Hence, the FE gradient effectively also encodes spatial frequency, and so raw FE and PE data can be plotted on the same graph since they both represent the same type of data. This is k-space- a raw data spatial frequency image of an object (Figure 1.7). In the FE PE data acquisition scheme already described, one axis would be of FE, the other of PE. The signal intensity (SI) is determined by the magnitude of the echo produced for each FE PE combination. The order in which MR data is acquired is best visualised by seeing how k-space filled up. A typical MR image slice encodes one dimension with FE and the other with PE. In this scheme k-space is filled up FE line by FE line, since all the FE data values for one value of PE are acquired simultaneously. The PE gradient is stepped with every RF pulse from a negative gradient through zero to a positive gradient to allow all the necessary FE PE combinations to be acquired sequentially.

1.3.3 Other Imaging Considerations

1.3.3.1 Repeated Pulse Sequences and T_1

Using PE means the RF pulse has to be repeated in order to fill up the whole of k-space (i.e. acquire all the information necessary for image formation). Waiting until M_0 has fully

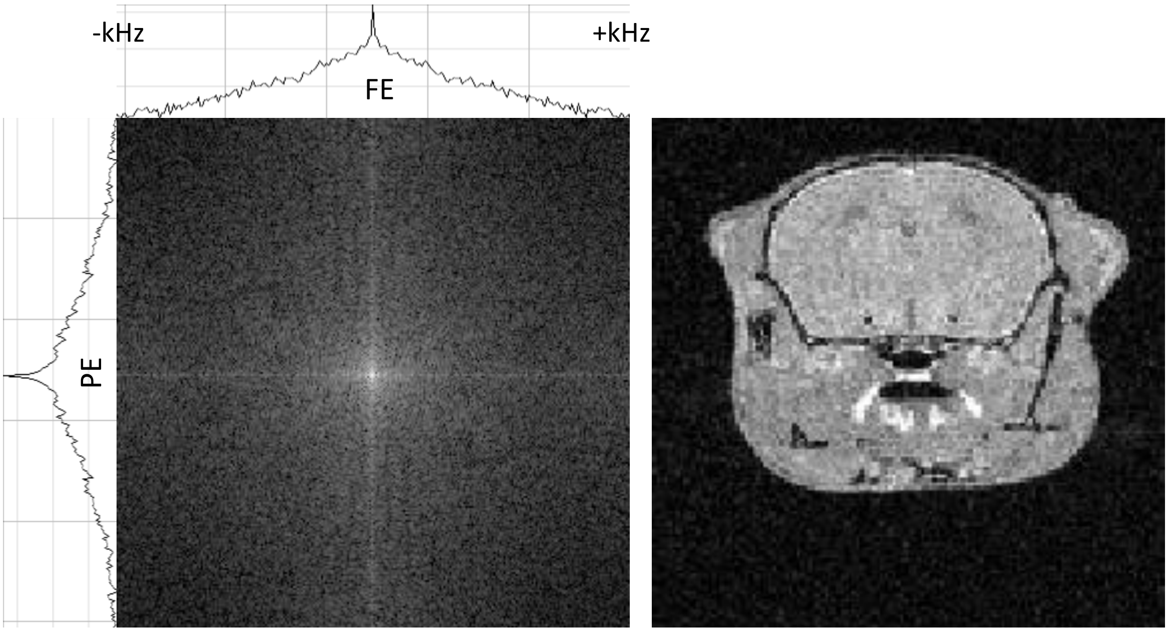

Figure 1.7: k-space. Signal intensities represent the amplitudes of signals produced for a given frequency and level of PE. The centre is bright since this represents the centre of the echo in the FE direction, and the lowest levels of PE in the PE direction (these tend to produce the largest signals since most objects possess more low spatial frequencies than high ones). After fourier transforming in both directions, the image on the right is produced. In standard imaging, one FE line is produced per excitation and echo.

recovered to repeat the RF pulse would use up a lot of time. Instead, we can repeat the pulse sequence prematurely. This reduces the available signal, but the reduction in acquisition time is often much greater. The level of signal reduction is dependent on what are known as T_1 processes. These influence the regrowth of longitudinal magnetization in the z-axis through the interaction of the spinning nuclei with unexcited nuclei and electric fields in the environment. T_1 is defined as the time required for the z-axis component of M_0 to be restored by a factor of $1 - e^{-1}$ (approximately 0.63) to its original magnitude. The relationship between signal, pulse sequence repetition time (*TR*), T_1 and the total available imaging time (which defines the number of averages that could be made for a given *TR*) is shown in Figure 1.8A. Thus the reduced signal can usually be more than made up for by repeating the pulse sequence further to acquire signal averages.

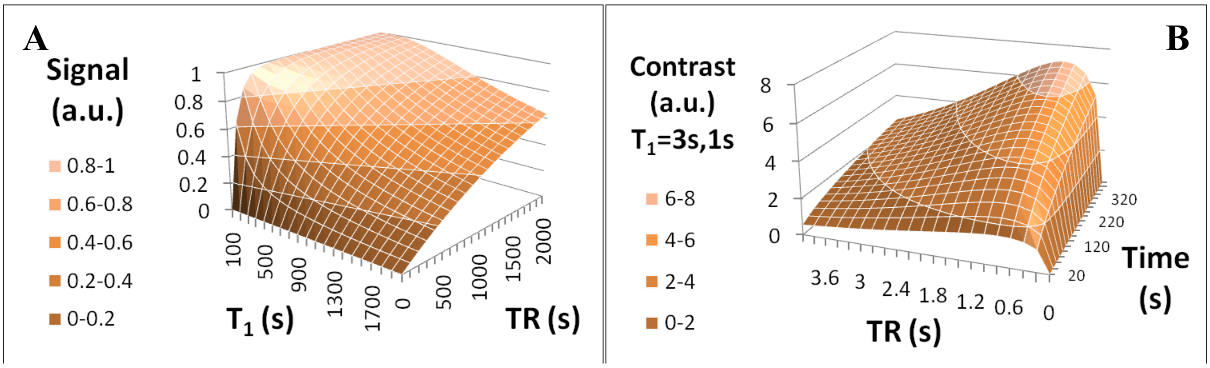

Figure 1.8: relationships between signal, time and T_1, as determined by the equation $signal \propto e^{-TR/T_1)}$. As *TR* lengthens and T_1 shortens, signal increases (A). However, the increase is not linear, and this makes contrast behaviour between two T_1 values for a range of acquisition time and *TR* values more complex. Signal increases $\propto \sqrt{2}$ of the number of averages (the number of averages being dependent on the available acquisition time), which depending upon the *TR* and T_1, may be a more or less efficient way of acquiring greater signal. The *TR*-time tradeoff for a given pair of T_1 values is shown in B, in this case 3s and 1s. Peak contrast for any given number of averages is achieved with a *TR* slightly less than the lower T_1. In general this result holds true for other T_1 pairs too.

1.3.3.2 T_1, T_2 and T_2^* Contrast

The usual aim of imaging is to differentiate biological states and tissue types. Acquiring maximum signal would do this based on spin density. However, this parameter does not vary substantially amongst tissue types or change much in normal or abnormal biological situations. Conversely the T_1, T_2 and T_2^* parameters do vary greatly. By altering the *TR* and echo collection time (TE) of the pulse sequence, we can alter its sensitivity to those parameters.

The growth of M_0 along the z-axis is described by the equation shown in Figure 1.8. Also plotted in Figure 1.8B are the changes with *TR* of signal difference (contrast) between two objects of different T_1 values, according to that equation. Hence to differentiate between two regions with different T_1 values, the *TR* should be set to a little below the lower T_1 value. In practice most objects to be imaged possess a wide variety of T_1 values, making the choice of *TR* a complex decision. It must also be noted that there are further complications if the pulse sequence uses partial excitation- that is not fully 90°. This is often done in gradient-echo based pulse sequences to increase acquisition speed, as although there will be less signal, M_0 recovery will be much faster. There is a nonlinear interaction between the tip angle and *TR*, making optimization of signal and signal contrast difficult (Busse, 2005; Haselhoff, 1997; Neelavalli and Haacke, 2007; Pelc, 1993).

The decay of M_0 in the x-y plane is described by the equation in Figure 1.3. The graph in Figure 1.3B is analogous to that in Figure 1.8B, but for T_2/T_2^*: for maximum contrast, the TE should be set about half-way between the T_2/T_2^* values of the objects to be differentiated. Similarly to the situation for T_1, most objects possess a wide variety of T_2/T_2^* values, making TE choice complex.

1.4 Using MRI to Measure Brain Activity

1.4.1 Changes That Occur During Neuronal Activity

Many events and processes occur during neural signalling, several of which alter tissue properties such as T_1 whose changes can be detected by MRI. The two that are most commonly exploited are outlined below.

1.4.1.1 Haemodynamic

Neurons expend energy to maintain a resting level of discharge (tone). This generates a resting level of energy expenditure. Neurons store very little energy, so when there is an increase in neuronal activity, and hence energy expenditure, there is an immediate requirement for an increased energy supply. This can be met by an increase in blood flow to supply the extra necessary oxygen (and glucose). In practice there is overcompensation in blood flow for the extra oxygen required, so in addition to a flow increase, the concentration of oxyhaemoglobin rises too. The elasticity of blood vessels means there is also an increase in blood volume (van Bruggen and Roberts, 2002). These changes are summarised in Figure 1.9.

1.4.1.2 Ca^{2+} Channel Opening

Entry of Ca^{2+} into cells and or cell compartments is a common stage in cell signalling processes. This includes neuronal signalling. When an action potential reaches the presynaptic terminal, it triggers the opening of voltage-gated Ca^{2+} channels. The influx of Ca^{2+} triggers

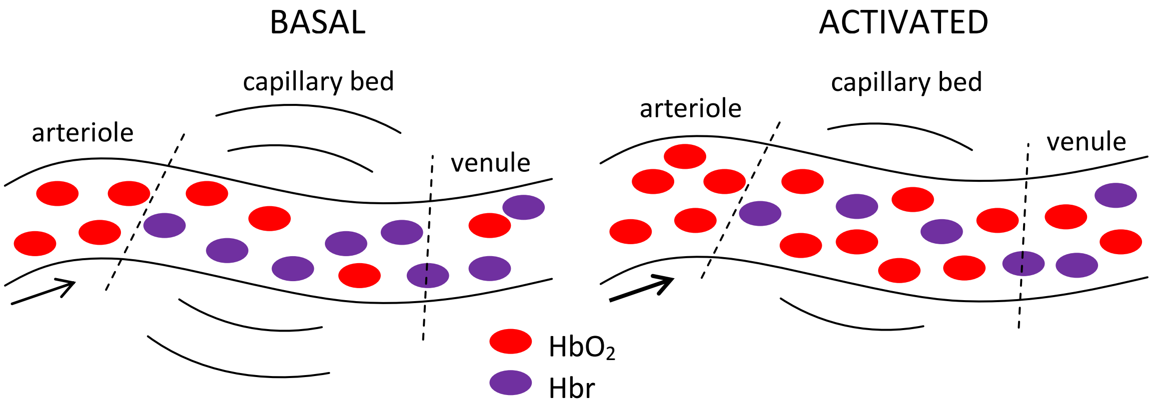

Figure 1.9: haemodynamics during basal and stimulated neuronal activity. Activation results in increased blood flow and volume, overcompensating for the increased oxygen usage. This causes an increase in the oxyhaemoglobin:deoxyhaemoglobin ratio, reducing the magnetic field inhomogeneity caused by deoxyhaemoglobin (lengthens T_2' and hence T_2^*). The combination of increased flow, volume and oxygenation increases signal. Figure inspired by that of Peter Jezzard (http://www.fmrib.ox.ac.uk/education/fmri/brief-introduction-to-fmri-physiology)

neurotransmitter release into the synaptic cleft, hence Ca^{2+} channel opening and influx is essential to neuronal activity, except in the case of electrical synapses where there are gap junctions between the pre- and postsynaptic terminals (Purves, 2001).

1.4.2 Detection of Haemodynamic Changes in the Brain

As explained above, there are three haemodynamic events during neuronal activation: a change in cerebral blood flow (CBF), volume (CBV) and oxygenation (BOLD- blood oxygenation level dependent). These factors between them affect T_1, T_2 and T_2^*, and so in principle can be detected by MR. There are many schemes to detect these changes. The most common are set out below.

1.4.2.1 Bolus Tracking/DSC-MRI

CBF and CBV changes can be detected and then quantified using dynamic susceptibility contrast (DSC-MRI), also known as bolus tracking MRI. Here, a bolus of blood pool contrast agent (does not diffuse out of the vascular space) which rapidly passes out of the body (e.g. Gd-DTPA) is injected intravenously (Figure 1.10A+B). A fast imaging sequence is then used to acquire a timecourse of images that are sensitive to the drop in T_2/T_2^* as the agent perfuses

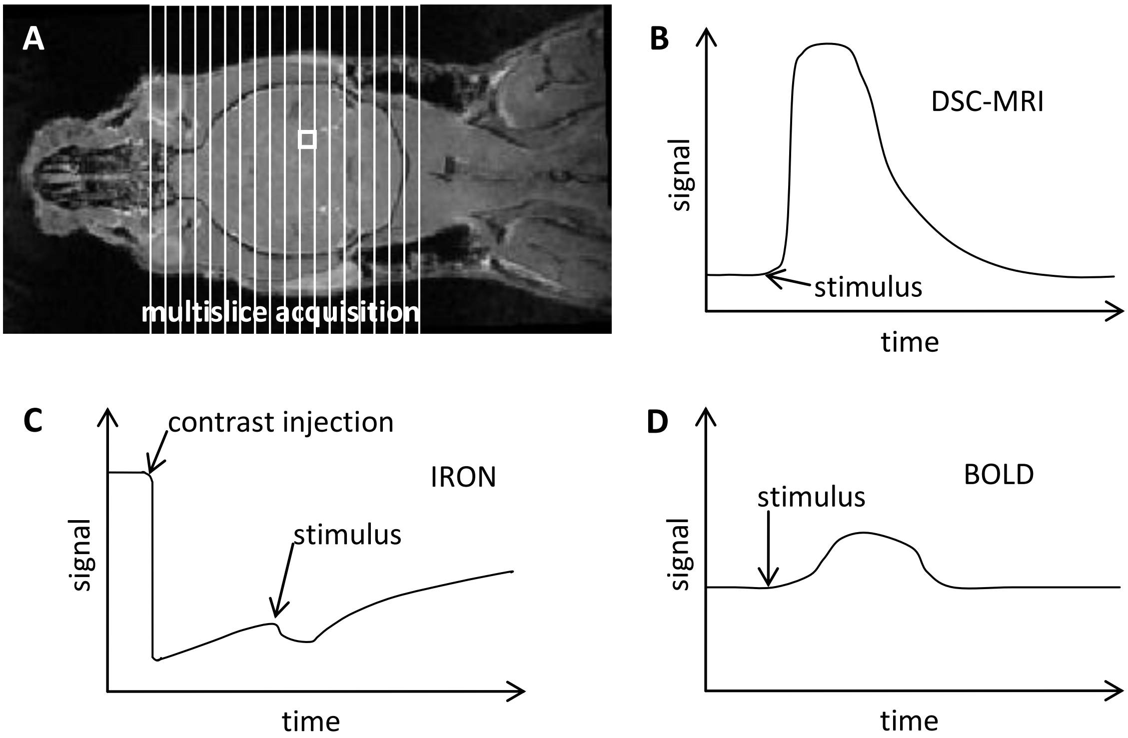

Figure 1.10: signals produced by DSC-MRI (B), CBV-weighted MRI (C) and BOLD (D). The signals are all examples of timecourses that could be produced from the voxel highlighted in A if this region were affected by the stimulus. In DSC-MRI the bolus injection of a rapidly excreted blood pool contrast agent (rapidly excreted agents normally generate positive contrast, hence the rise in signal) produces a complex curve that can be used to determine both blood volume and flow. In CBV the bolus is of a slowly excreted blood pool contrast agent (these are usually negative contrast agents, hence the signal drop). The signal is now largely weighted to blood volume, so injection of a stimulus will cause a signal drop due to an increase in blood volume. BOLD MRI is much simpler, with the stimulus causing an increase in signal via the full composite BOLD effect outlined in Figure 1.9.

through the brain. This was the first technique used in fMRI (Belliveau et al., 1991). By measuring some input parameters, and making certain assumptions, both CBF and CBV can be quantified from this data (Østergaard, 2005).

DSC-MRI has an inherently low temporal resolution since time has to be given for the injected agent to flow in and wash out completely. Without full washout, contrast agent accumulation would cause CBF estimation difficulties due to a changing baseline SI, and the circulating dose would begin to reach toxic levels. The low temporal resolution is not necessarily a problem since the haemodynamic changes in response to neuronal activity relating to energy balance stimuli have a low temporal frequency- they occur over long periods of time (minutes) relative to other classes of stimuli such as somatosensory (seconds). However, despite typical DSC-MRI contrast agents such as Gd-DTPA clearing much more rapidly in rodents than in humans, the time required is still far too long- upwards of 30 mins between injections (Rudin and Sauter, 1991). Another insurmountable problem with DSC-MRI is that it relies on equivalent circulation between the animals being studied. Many animal models used in the study of energy balance have varied body weight (mostly due to altered fat mass) and composition, and such changes can result in altered circulation in both humans (Bolinder et al., 2000; Jansson et al., 1992, 1998; Summers et al., 1996) and rats (West et al., 1987). This could be accounted for by altering the model relating DSC-MRI signal changes to CBV, but making the model flexible enough to accept wide variations in body composition is a very large undertaking, especially given how complex the model is already.

1.4.2.2 ASL

CBF can also be measured relatively non-invasively using arterial spin labelling (ASL). This technique acquires a pair of images, known as the control and label. The labelled image is different in only one way from the control- an RF pulse is applied that inverts the magnetization of the tissue that is the source of the blood flowing into the region of the brain to being studied (Figure 1.11). Inversion attenuates the blood's signal, such that it acts as an endogenous tracer in a similar manner to contrast agents in DSC-MRI, but with the T_1 dropping instead of T_2/T_2^*. Both control and label images are acquired with a maximally T_1-, minimally

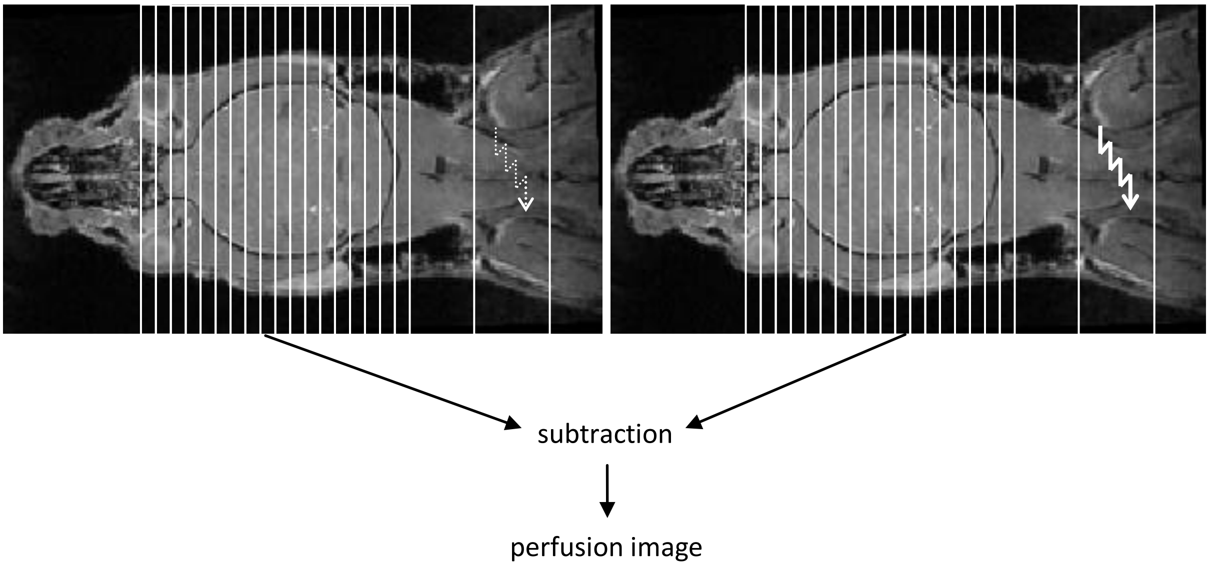

Figure 1.11: ASL. Images are acquired in pairs. First a control image, using a normal rapid T_1-weighted sequence, except for the pre-acquisition application of an off-resonance RF pulse in tissue where the blood flowing into the imaged region originates (usually the neck). The second image of the pair is the same except it is tagged by making the extra RF pulse on resonance. This attenuates the signal of blood flowing into the imaged region. Hence the subtraction of the two images will be different where the most blood is flowing- that is perfusion weighted. The timecourse will now be similar to that of BOLD images (see Figure 1.10D) except that the use of image pairs inherently corrects for any baseline signal drift, making the technique much more powerful for observing stimuli with long cycle times.

T_2/T_2^*-weighted sequence to maximise sensitivity to the inversion's effect on T_1 and reduce sensitivity to CBV and BOLD effects on T_2/T_2^*. Subtracting the labelled image from the control yields a perfusion-weighted image (Williams et al., 1992). As with DSC-MRI, making some assumptions and knowledge of certain input parameters can help quantify the change (Liu and Brown, 2007; Wong et al., 1997).

ASL is a promising alternative to DSC-MRI for CBF measurement. Since it relies on an endogenous contrast agent (labelled blood), there are no dosing problems and the temporal limiting factor of washout is gone. Circulation is still a potential confound, but this is unlikely to have much effect since magnetization inversion is typically done at the neck, so the blood does not have to pass though much tissue before reaching the brain. ASL is particularly suited to observing slow changes as it inherently corrects for a drifting baseline signal by acquiring a control image for every tagged one. This gives it great statistical power when the stimuli have low temporal frequency (Aguirre et al., 2002). Drifting baseline signal is a great problem for CBV and BOLD measures for differing reasons, and with different solutions that will be discussed later. Unfortunately ASL has numerous implementation problems, mainly relating to the RF inversion pulse and model of CBF quantification. These can be overcome, leaving the main issue of low SNR- signal changes are often only a few percent (Wong et al., 1997).

1.4.2.3 IRON

Relative changes in CBV can be monitored by injecting a large volume of a blood pool contrast agent that remains in the body for a substantial amount of time (e.g. Endorem, which reduces T_2/T_2^*). Changes in CBV will alter the concentration of contrast agent in tissue, altering signal levels (Figure 1.10A+C). As long as the contrast agent levels are high enough, any effect that simultaneous changes in CBF or BOLD have on signal intensity will be swamped by those from CBV. This has been dubbed the IRON technique (Chen et al., 2001; Jenkins et al., 1993), meaning increased relaxation with iron oxide nanoparticles. Methods for CBV measurement in the absence of an exogenous contrast agent exist (Gu et al., 2006; Lu et al., 2003), though these are quite recent developments and in the case of VASO doubts remain about its mechanism (Lu et al., 2003).

The large contrast agent concentrations used in IRON provide very large signal changes, and hence increased CNR (Jenkins et al., 1993; Mandeville et al., 1998, 2004) compared to the BOLD technique (discussed later). This is especially pronounced at low B_0. This effect diminishes at higher B_0, though experimental evidence indicates it lasts up to at least 9.4T, and should continue indefinitely (Mandeville et al., 2004). There are two main problems with IRON. First, a very large concentration of agent (much more than would be approved of in humans) is required to achieve blood volume weighting (Mandeville et al., 1998). As a consequence, there may be subtle effects on physiology (Sharma et al., 1999), and the animal MRI data becomes less comparable to human data where non-IRON methods have to be employed (Lu et al., 2007). Second, it is thought that CBV responds relatively slowly compared to other haemodynamic parameters (Buxton et al., 1998; Mandeville et al., 1999), though it has been proposed that this may be an effect of anaesthesia and species difference (Frahm et al., 2008; Martin et al., 2006). A relatively minor problem is that blood pool contrast agents gradually wash out of the body, resulting in baseline drift. However, this drift is predictable, and can be factored out with appropriate modelling (Schwarz et al., 2003).

1.4.2.4 BOLD Effect

The blood oxygenation level dependent (BOLD) effect refers to how the change in blood oxygenation during neuronal activity affects the MR signal, due to the longer T_2/T_2^* of oxygenated than deoxygenated blood (Barth and Moser, 1997; Lee et al., 1999; Meyer et al., 1995; Ogawa et al., 1993a; van Zijl et al., 1998). Unfortunately blood oxygenation cannot be measured directly and/or quantified by one MR method alone, as there is no known pulse sequence, MR parameter, contrast agent or combination of the above that is sensitive to only oxygenation. To observe a pure BOLD effect a BOLD-sensitive sequence (i.e. haemoglobin oxygenation sensitive- T_2/T_2^*-weighted) has to be interleaved with both CBF and CBV measures so that their effects can then later be subtracted out (Gu et al., 2005; Shen et al., 2008; Yang et al., 2004). This is usually not carried out for practical reasons. Instead, the composite BOLD measure, using a simple T_2/T_2^*-weighted sequence alone is employed (Figure 1.10A+D). It has a higher sensitivity than measuring CBF, CBV or pure BOLD alone, since all three measures theoretically change signal from a T_2/T_2^*-weighted imaging sequence in the same direction during changes in neuronal activity- blood flow, volume and oxygenation all increase during periods of heightened activity, increasing signal, and vice-versa. The BOLD effect's relative sensitivity and simplicity of implementation make it the most widely employed haemodynamic proxy for imaging neuronal activity.

The BOLD effect technique has many shortcomings. The most dramatic is a poor correlation between the centre of BOLD response and that of the neuronal activity that caused it. The cause is BOLD's relatively high sensitivity to changes in deoxyhaemoglobin levels in large blood vessels. This shifts the position of the response from the capillaries close to the active neurons towards draining veins. This effect is dramatic at typical clinical field strengths such as 1.5T (Duyn et al., 1994; Frahm et al., 1994; Hoogenraad et al., 2001; Lai et al., 1993; Oja et al., 1999; Song et al., 1996) and also 3T (Olman et al., 2007). At higher field strengths it starts to diminish since the BOLD effect in capillaries is theorised to vary quadratically with field strength, but only linearly in larger vessels (Ogawa et al., 1993b)- hence at higher fields the BOLD response will be weighted more towards capillaries, a prediction that has been confirmed experimentally (Duong et al., 2000a, 2003; Gati et al., 1997; Krüger et al., 2001; Lu and van Zijl, 2005). However, it still persists- for example even at 9.4T there will be bias towards surface vessels unless less sensitive T_2-weighted spin-echo pulse sequences are employed (Lee et al., 1999, 2002).

1.4.3 Manganese-Enhanced MRI (MEMRI) is Sensitive to Voltage-Gated Ca^{2+} Channel Opening, and Hence Brain Activity

1.4.3.1 Principles of MEMRI

Manganese (Mn) is an essential trace element in animals, primarily since it is the cofactor for many classes of enzyme (Aschner et al., 2007). Experiments in tissue culture (Drapeau and Nachshen, 1984; Hallam and Rink, 1985; Narita et al., 1990) and isolated neuromuscular junctions (Meiri and Rahamimoff, 1972) indicate that at supraphysiological concentrations Mn is able to enter cells through voltage-gated Ca^{2+} channels. Since the opening of these channels is essential for synaptic transmission (Purves, 2001), it is plausible that when administered at high doses Mn accumulation could mark neuronal activity. This is relevant to MRI since the +2 oxidation state of Mn forms the paramagnetic Mn^{2+} ion. Paramagnetism will alter the MRI signal, and in the case of Mn^{2+} this leads to a shortening of both T_1 and T_2 in solution and tissue (Kang and Gore, 1984; Mendonça-Dias et al., 1983). Thus Mn^{2+}, when administered at a large enough dose, could be used as an MRI-visible reporter of changes in or differential neuronal activity.

Early studies using vascular administration of Mn^{2+} (as $MnCl_2$) showed that glutamate (Aoki et al., 2002; Lin and Koretsky, 1997) and electrical forepaw stimulation (Aoki et al., 2002; Duong et al., 2000b; Lin and Koretsky, 1997) were able to influence Mn^{2+} uptake in the brain to a large enough extent to cause changes in the signal intensity of T_1-weighted MR images in the expected brain regions. Further studies of Mn^{2+} transport following focal injection into discrete brain regions showed signal intensity enhancement patterns that could only be explained by Mn^{2+} uptake at synapses and axonal transport to connected brain regions (Pautler et al., 1998). Hence at high concentration Mn^{2+} is taken up by neurons in live animals in proportion to those neurons' activity. Although it is currently unknown what proportion of the Mn^{2+} is being taken up by neurons due to action potentials as opposed to one of the many other possible mechanisms (Aschner et al., 2007), the combination of a viable mechanism and a visible robust response mean MEMRI is a valid and potentially useful method for visualising brain activity.

MEMRI can also be used for generating anatomical contrast (Burnett et al., 1984; Cory et al., 1987; Fornasiero et al., 1987; Geraldes et al., 1986) and, as alluded to above, tract tracing. Further discussion of these subjects can be found elsewhere (Pautler, 2004; Wadghiri et al., 2004; Watanabe et al., 2002).

1.4.3.2 Manganese Formulation and Toxicity

The simplest way of delivering Mn^{2+} is as a solution of the chloride salt $MnCl_2$. Although other formulations have been tried, $MnCl_2$ remains the most commonly used (Silva et al., 2004) since it is cheap, widely available and none of the other possible formulations (all of which are more expensive and less available) have shown any obvious advantage.

The primary concern when administering Mn, including as $MnCl_2$, is toxicity. Chronic overexposure to Mn in humans leads to a wide variety of psychiatric and motor disturbances (Aschner et al., 2007; Crossgrove and Zheng, 2004). These effects exclude most Mn formulations from use in humans. Exceptions would include chelated forms, such as mangafodipir trisodium (Federle et al., 2000), a contrast agent approved for use in human hepatic MRI studies. Chelation improves safety (Elizondo et al., 1991) but also reduces the efficacy of Mn as a contrast agent, hence it is not suitable for use in functional MEMRI studies. Acute administration in animals also has a number of dangers, primarily cardiovascular and breathing rate depression (Wolf and Baum, 1983). As a consequence it is important to make a very careful compromise regarding $MnCl_2$ dose. High doses will provide a large signal contrast level that will make observation of experimentally induced changes in Mn concentration more robust. Low doses will reduce the physiological confound of $MnCl_2$ toxicity. Many other factors interact here including administration route and rate, solution concentration, temperature and anaesthetic levels (Silva et al., 2004).

1.4.3.3 Variables in MEMRI Experiments

Most functional MEMRI experiments to date are variations on the intravenous (i.v.) administration scheme presented in Figure 2.1 on page 51. There are a very large number of variables here, and for most of these their effects have not been fully explored.

The experiment starts with a baseline acquisition from which changes in SI will be measured. Too few baseline acquisitions will result in an inaccurate baseline estimation and hence erroneous determination of SI change. Too many acquisitions will waste time.

The Mn administration itself is subject to many variables. The concentration and volume of the solution, its rate of infusion in terms of both volume and concentration, plus the total length of the infusion time and the related variable of total dose are all likely to affect the amount of Mn that can be administered before toxicity becomes a substantial confound. A demonstration of this is the large discordance between reported $MnCl_2$ LD50 values of 38 and 121mg kg^{-1} (Sigma-Aldrich Company Ltd., 2006; Silva et al., 2004), and the much higher doses of up to 175mg kg^{-1} i.v. (1hr infusion) that have been given to animals in recent MEMRI experiments (Lee et al., 2005). Something about the differences in administration method are likely to have caused this discrepancy, although it is possible that other factors such as the strain and general health of the animals could have been an influence too. The difference is important since providing higher doses spread out over longer periods of time increases the signal and time available for an experiment, increasing its power and potentially doing so without confounds from toxicity.

A crucial choice to be made is whether or not to degrade the blood-brain barrier (BBB). Mn is able to cross it, but at a low rate. This limits the availability of Mn to neurons and hence MEMRI's ability to detect neuronal activity. It also biases the sensitivity of MEMRI towards nuclei located close to circumventricular organs where the BBB is relatively weak and where Mn initially accumulates in the brain. Breaking open the BBB overcomes this problem, but also acts as a physiological confound. This is especially the case where the stimuli involve drugs acting on the brain- these would no longer have their access impaired by the BBB. This includes agents involved in energy homeostasis, many of which normally have to access the brain via saturable mechanisms, e.g. insulin (Banks, 2004) and leptin (Banks et al., 1996).

The stimulus timing and duration are also very flexible. The very first study of functional MEMRI demonstrated that this was the case by providing a glutamate stimulus both before and during a scan, and in both cases glutamate's excitatory effect was visible as increased Mn uptake (Lin and Koretsky, 1997). Since Mn takes approximately 24 hours to fully disperse throughout the brain (when the BBB is not disrupted), the possibility also exists to provide the stimulus after Mn administration.

Linked to this is the possibility of providing the stimulus and Mn to awake, freely moving animals, removing the anaesthesia confound (a factor which itself is subject to the variables of anaesthetic choice and depth). The scan would then be conducted after a delay determined by a compromise between the duration of the stimulus and how dispersed we wanted the Mn to be- i.e. how homogenous we would need its sensitivity to be across the whole brain. A number of recent MEMRI studies of the auditory system have taken this idea and married it with i.p. injection (Yu et al., 2005, 2007, 2008), which is technically easier than i.v. injection or infusion. This scheme is shown in Figure 2.2 on page 52. The one big disadvantage of this is that there is no longer any temporal resolution, since Mn flux 24 hours post-administration is very slow. Any images acquired are snapshots of overall activity over the previous 24 hours, as encoded by Mn uptake. This disadvantage can be turned into an advantage- the low Mn flux means a much longer time can be spent acquiring images since our marker of neuronal activity is being held static rather than rapidly changing as it would do during an i.v. infusion. Longer scan durations allow the acquisition of images with much higher spatial resolution and SNR.

One possibility not alluded to in Figure 2.1 or Figure 2.2 is performing MEMRI more than once on the same animal over time- a longitudinal study. Such studies are particularly valuable since they can reduce animal use and reduce inter-animal variance by taking advantage of the non-lethality of MRI. For these we need to consider an issue as important as administration and uptake- Mn^{2+} release, a much slower process. Indeed, it is so slow that until recently it had been thought that Mn^{2+} was permanently sequestered in the brain, since although the MEMRI signal completely decays after a few weeks (Aoki et al., 2004), biochemical assays indicated there is still a presence of Mn^{2+} with a half-life of upwards of 52-74 days (Gavin et al., 1990, 1992). However, a recent study using in parallel both MRI and inductively coupled plasma mass spectrometry (ICP-MS) showed that the near total loss of MEMRI signal in the brain during the 5-6 weeks post-administration does correlate with the actual Mn^{2+} concentration in tissue, giving a half-life closer to 14 days, hence Mn^{2+} is substantially cleared out of the brain within a month. This is still a slow pace, and means that MEMRI experiments are necessarily measuring cumulative uptake in the short-term, therefore knowledge of the precise rate of efflux is not essential for experimental planning. However, for longitudinal studies of the same animal the rate needs to be taken into consideration to avoid performing MEMRI on an animal that still has residual Mn^{2+} present and hence residual MEMRI signal. Such experiments have only been performed and published twice, and in both of these cases the aim was to map connections between regions rather than measure changes in activity (Soria et al., 2008; Van Meir et al., 2004).

1.4.4 Analysis of Haemodynamic and MEMRI fMRI Data

Despite both being 4D datasets (3D image timecourses) of the same object, where we are interested in analysing signal changes over time at each and every voxel, haemodynamic and MEMRI data have traditionally been processed differently. Haemodynamic image processing is highly automated, based on a framework developed from the early 1980s (Fox et al., 1988; Friston et al., 1991, 1995a,b; Turner et al., 1998). An overview of the general principle is shown in Figure 3.1 on page 85. Firstly, images are spatially normalised- that is brains are motion and position corrected to bring them into the same space. A GLM (general linear model) of the hypothesised signal change is then fitted to each voxel and statistical maps produced of the fit. Region of interest (ROI) data can also be automatically extracted based on standardised atlases of brain anatomy if a certain region is of particular interest. There are a number of software suites available that implement these methods with straightforward interfaces (Cox, 1996; Smith et al., 2004; The FIL Methods Group, 2005).

Surprisingly, MEMRI data tends to be analysed manually, using hand-drawn ROIs to extract signal time courses which are then analysed on a per-region basis (Aoki et al., 2002; Lin and Koretsky, 1997; Parkinson et al., 2009). This is more laborious, less objective, and also wasteful since for labour-saving purposes it is common for many brain regions with potentially interesting data to be left unextracted. Even where more automated methods have been applied to MEMRI data, they have tended to require some substantial degree of manual intervention, and made use of proprietary tools (Yu et al., 2008).

1.5 Overview of fMRI Studies of Energy Balance in Rodents

Given its importance, there have been surprisingly few fMRI studies of energy balance or appetite in rodents. There are just five studies published using haemodynamic methods. One involved acute stimulation with an amino acid after chronic deprivation of that amino acid (Yokawa et al., 1995). Two involved glucose stimulation- of these, one via the i.p. route (Mahankali et al., 2000), the other oral (Tabuchi et al., 2002). Another two studies involved the hypophagic and hypolocomotive serotonergic agonist mCPP (Stark et al., 2006, 2008)).

Amongst MEMRI studies, there are just five publications- all from the same laboratory, using stimuli of fasting (Kuo et al., 2006), gut hormones and other pharmacological stimuli (Chaudhri et al., 2006; Kuo et al., 2007; Parkinson et al., 2009) and diet (So et al., 2007).

1.6 Aims

The dearth of studies makes using fMRI for studying areas of the brain involved in energy balance a potentially fruitful area for discovery. There were three broad aims of this project, which correspond to the three Results chapters that follow.

- Make any possible MR acquisition and $MnCl_2$ administration protocol improvements to those used in previous appetite MEMRI studies (Chaudhri et al., 2006; Kuo et al., 2006, 2007; Parkinson et al., 2009; So et al., 2007) and use these to better characterise brain activity in response to gut hormones.
- Bring the statistical analysis of MEMRI data into the framework used in analysis of human fMRI in order to make analyses less laborious and more objective.
- Determine if it is possible to use haemodynamic MRI methods to observe responses to gut hormones.

Chapter 2

Manganese-Enhanced MRI

2.1 Introduction

MEMRI has the potential to make substantial contributions to the study of neuroscience. It is a relatively non-invasive method for observation of whole brain activity at reasonably high spatiotemporal resolution, and has been tested for efficacy with a variety of different stimuli including electrical forepaw stimulation (Aoki et al., 2002; Duong et al., 2000b; Lin and Koretsky, 1997), audition (Yu et al., 2005, 2007, 2008) and gut hormone injection (Chaudhri et al., 2006; Kuo et al., 2007; Parkinson et al., 2009). It does not directly measure the electrical activity of neurons, so it must be regarded as a proxy measure. Nevertheless, its observation mechanism- detecting the accumulation of Manganese in active neurons- is much more direct than haemodynamic measures, and more resistant to physiological perturbation (Van der Linden et al., 2007).

The concern of this thesis is using MRI to study appetite-related stimuli, and in this field MEMRI has demonstrated an ability to detect the effect of a wide variety, including fasting (Kuo et al., 2006), gut hormones (Chaudhri et al., 2006; Kuo et al., 2007; Parkinson et al., 2009) and diet (So et al., 2007). The same MEMRI protocol was used in these five studies. As with any MEMRI protocol, it can be split into two semi-independent parts- the Mn administration, and the imaging sequence. The Mn administration part used in these studies is outlined in Figure 2.1.

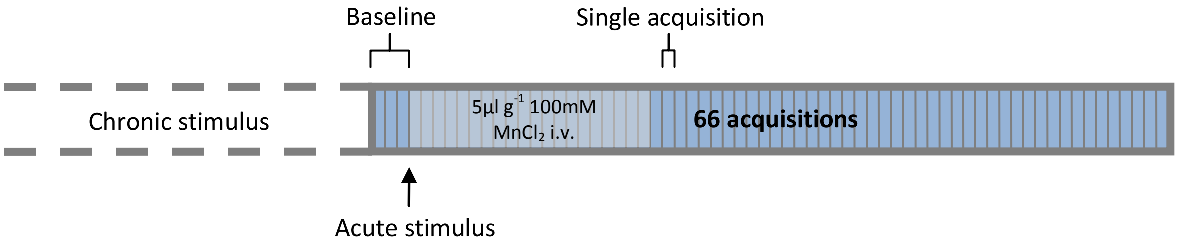

Figure 2.1: schematic of dynamic MEMRI protocol (Chaudhri et al., 2006; Kuo et al., 2006, 2007; Parkinson et al., 2009; So et al., 2007). Acute stimuli are usually hormones, but have included other agents such as hypertonic saline and the nauseant LiCl. Prior to a scan, chronic stimuli- such as altered diet and genetic modification- may have been applied. After three baseline acquisitions, $MnCl_2$ is infused at a dose proportional to body weight for a finite period lasting 19-20 acquisitions. In addition, an acute stimulus may be administered, usually at the start of the $MnCl_2$ infusion. The timecourse is continued until 66 images have been acquired. The infusion results in signal intensity changes in the images (see Kuo et al. (2006) for details) that are proportional to neural activity.

There are three potential difficulties with this method. The most important, especially with appetite-related studies, is the adjustment of $MnCl_2$ dose. Ideally this should be done such that the amount of Mn reaching any given part of the brain will be identical across animals. Assuming the brain vasculature is similar across animals, another way of describing this is that we want the concentration of Mn in the blood vessels supplying the brain- the internal carotid arteries- to be similar. The most direct way of achieving this is administering the Mn directly into those vessels. This is technically very difficult, and it is preferable to administer $MnCl_2$ through peripheral surface vessels. The lateral tail veins are the easiest vessels to access, but are also the most distant from the internal carotid arteries, so the Mn has to pass through much of the rest of body before reaching the brain. Different parts of the body have different Mn uptake properties (Ni et al., 1997; Spiller et al., 1988; Takeda et al., 1998). Fortunately, within any given group of genetically inbred rodents of similar ages and/or weights, there is not much substantial variance in body tissue composition (Nagy et al., 2002; Reed et al., 2007). Consequently, under these circumstances, it is reasonable to assume that adjusting Mn dose by total body weight will ensure the amount of Mn reaching the brain will be similar in all animals. However, in many appetite-related experiments this assumption does not hold. The most important example of this is with altered diets. These can cause many organs and body tissues to change size, most dramatically the levels of adipose tissue. This will change the amount of Mn removed from

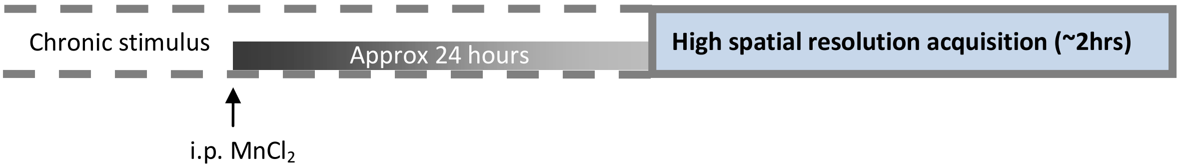

Figure 2.2: schematic of generic static MEMRI protocol (Yu et al., 2005, 2007, 2008). $MnCl_2$ is injected i.p., and 24 hours later an anatomical scan is acquired to measure Mn uptake. The chronic stimulus is best applied evenly across the entire Mn uptake period, usually the 24h prior to the scan.

circulation before it reaches the brain. For example, consider a fat, heavy animal- if dosed by body weight, it would be given a large amount of Mn compared to a lighter lean one. Since much of the extra weight is adipose tissue which does not take up much Mn (A. Koretsky, *pers comm*, Lee et al., *in prep*), the Mn would be highly concentrated in the circulation and its brain would receive an inappropriately high dose of Mn compared to the lean animal. The resulting increased Mn enhancement could lead to the potentially erroneous conclusion that the animal's adiposity was due to increased neuronal activity, to the detriment of other possibilities such as reduced energy expenditure- ironically something potentially caused by reduced neuronal activity.

The second difficulty with the method outlined in Figure 2.1 is the pulsed nature of the $MnCl_2$ administration. This leads to relatively complex signal intensity timecourses that form curves rather than straight lines (see Figure 2.3C on page 54 for an example). This makes it difficult to judge whether changes in Mn uptake at a particular timepoint are due to the stimulus or the pulsed administration. A rapid bolus of $MnCl_2$ provided at the start of the scan, or even better a steady infusion throughout the whole scan, would produce signal intensity timecourses that are much easier to interpret.

The third difficulty is that i.v. cannulation and scanning of a mouse during $MnCl_2$ administration must be done under anaesthesia to avoid large amounts of stress being placed upon the animal. Anaesthesia works by attenuating neuronal activity (Franks, 2008), which will include that of any systems under stimulation, reducing our ability to observe any responses. Unlike haemodynamic methods, there are MEMRI schemes which can circumvent the anaesthesia when studying neuronal activity. The principle is outlined in Figure 2.2. It involves administering the $MnCl_2$ outside the scanning environment, during a period of stimulus. Mn is allowed to distribute throughout the brain over a period of time, with differential accumulation marking the effect of the given stimulus. A scan is then acquired whose results represent cumulative neuronal activity over the period of time between the $MnCl_2$ administration and the image acquisition. Although first suggested as far back as 1997 (Lin and Koretsky, 1997), this scheme has only recently been exploited (Yu et al., 2005, 2007, 2008). It has two big advantages: 1) there is no anaesthesia confound since Mn accumulation and stimulus occur while the animal is conscious and freely-moving; 2) the image acquisition does not have to be rapid, so more emphasis can be put on acquiring high spatial resolution data with high Mn sensitivity. It does, however, have two big disadvantages: 1) there is no longer any temporal resolution, since the scan is conducted after the stimulus has finished and during a period of little or no Mn flux; 2) there is no equivalent of the baseline from which to judge Mn uptake. Instead, regions have to be found that are not affected by the stimulus in order to normalise images prior to comparison with each other. In addition, there is still the issue of how to administer an appropriate dose.

There are also a number of shortcomings with the simple 2D multislice spin-echo image acquisition protocol used in the five studies mentioned earlier (Chaudhri et al., 2006; Kuo et al., 2006, 2007; Parkinson et al., 2009; So et al., 2007). Despite the mouse brain being around 15mm long in the rostro-caudal axis (Paxinos and Franklin, 2004), images are only acquired along 10mm of it. In addition, these slices are 1mm thick, giving very low spatial resolution. In combination with the ROI-based image analysis these studies used, this gives it a spatial resolution no better than live animal electrophysiology. Additionally, the *TR* is set at 600ms, much lower than the T_1 of any part of the mouse brain, even after shortening following $MnCl_2$ administration (Kuo et al., 2005). This is not optimal for detecting Mn-induced changes in SI in the hypothalamus.

A final issue is that although a timecourse is acquired, the data are so noisy that temporal resolution is not possible. To demonstrate this, it is useful to look at graphs of signal change from a CBV experiment of an i.v. cocaine stimulus (Figure 2.3E), and also from a MEMRI experiment of an i.a. NaCl stimulus where the BBB had been compromised (Figure 2.3A), and one of an i.p. NaCl stimulus where it had not been (Figure 2.3C). The MEMRI graphs

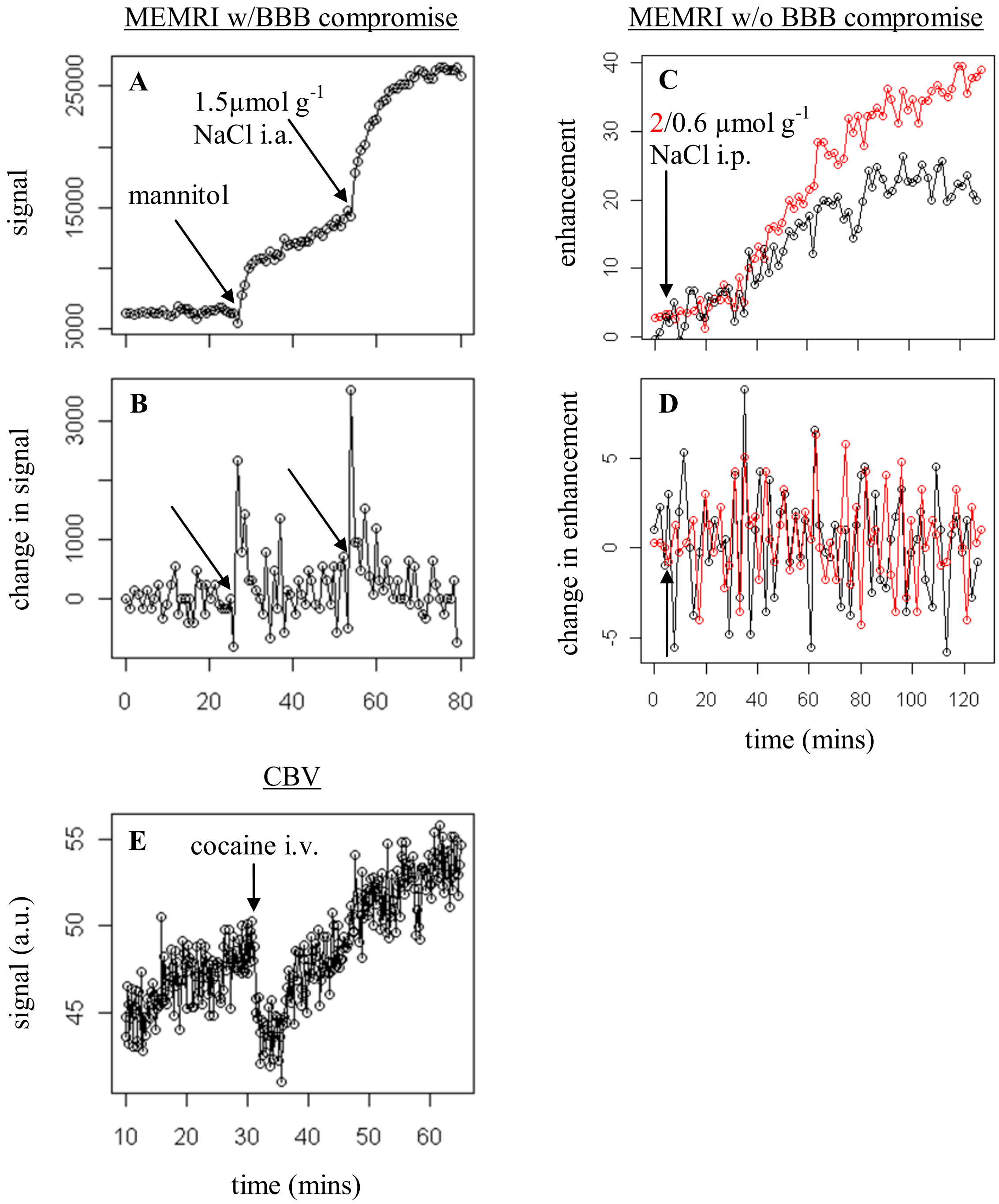

Figure 2.3: example data on MEMRI temporal sensitivity to an acute NaCl stimulus with (Morita et al., 2002) and without (Kuo et al., 2007) BBB compromise in rats and mice respectively, plus a comparison to a pharmacological CBV experiment in the rat (Schwarz et al., 2003). Ideally the same model would have been used but no suitable data were available. The MEMRI data represents cumulative Mn uptake whereas neuronal activity is proportional to rate, so these datasets have been converted to graphs of change in signal (B+D) to provide a fairer comparison to CBV (E). Mannitol (A+B) was used to degrade the BBB. In panels C and D the low dose control stimulus is also shown to make it clearer that most of the signal change is due to Mn infusion. Data from panels A-D is derived from the whole PVN, E from a single striatal voxel. It is quite clear that CBV has by far the highest temporal sensitivity, with MEMRI performing well when the BBB is broken but poorly when not.

have additionally been converted to show change of Mn uptake over time (Figure 2.3B+D). This is a fairer and more direct comparison to CBV, since neuronal activity is supposed to be proportional to the rate of Mn uptake, not the cumulative Mn uptake. As can be seen in the MEMRI experiments with a compromised BBB, even large responses fail to translate into graphs of signal change whose noise levels are low enough to be able to easily resolve at what timepoint a stimulus began and its effects ended. Without BBB compromise, the situation is even worse, with little visible difference when looking at a graph of change in signal intensity. The robust performance of CBV is even more remarkable given that the CBV data here was acquired from a single voxel of one animal, while the MEMRI data came from whole ROIs, of one animal in the case of the compromised BBB experiment, and averaging a group of four in the case of the intact BBB experiment. Ideally, identical stimuli would have been used in all three experiments, but no such data was available. The principles demonstrated here are, however, generally applicable, and in these experiments the different stimuli used are highly unlikely to have been the cause of such variable responses.

The aim of this series of experiments was to investigate methods that could deal with these shortcomings. With respect to $MnCl_2$ administration, specifically to try out administering the $MnCl_2$ dose according to lean mass, as determined by MRS. This should be much more closely correlated to circulation volume than whole body mass. This was tested in experiments on genetically obese *ob/ob* mice (Bray and York, 1979; Ingalls et al., 1950), where dosing by whole body weight leads to a high intra-scan mortality rate (5/5 animals tested). Also tested were two new infusion methods- one where the current dose is spread over the length of the entire scan (same dose given by the end, but more slowly), and one where the rate is continued across the entire scan (leading to a higher dose by the end). These should both provide simple linear signal change backgrounds, in addition to ensuring useful levels of Mn enhancement. Finally, the possibility of using i.p. administered Mn as a rapid anaesthesia-free method of assessing neuronal activity (Yu et al., 2005, 2007, 2008) in response to gut hormone injections was investigated.

With respect to changing the imaging sequence, two new methods were tried. The first, 3D gradient-echo, is slow and thus has poor temporal resolution, but due to increased SNR and much reduced partial volume effects, may produce a very high CNR to which models of Mn uptake may be fitted with high enough accuracy to infer when changes in Mn uptake took place. Also tried was fast spin echo, similar to the spin-echo method previously used (Chaudhri et al., 2006; Kuo et al., 2006, 2007; Parkinson et al., 2009; So et al., 2007) but acquiring multiple echoes per excitation. This allows multiple lines of k-space to be acquired per *TR*, rapidly increasing acquisition speed. There is a reduction in signal due to acquiring some of the data after more relaxation has taken place, but this should more than be made up for by increased signal from being able to employ a longer *TR*, which is more efficient both in terms of signal and contrast. With both sequences an aim was to acquire whole brain images at reasonably high isotropic resolution. This aids in using automated spatial normalization software that allow more objective and reproducible image analysis, and is discussed further in Chapter 3.

2.2 Materials and Methods

2.2.1 Reagents

Molecular biology grade 1M $MnCl_2$ (Sigma-Aldrich, cat# M1787) was dissolved in sterile ddH_2O to form more dilute solutions. Ghrelin (Bachem cat# H-4864) was dissolved in sterile ddH_2O before aliquotting into vials with 9nmol (30μg) each. These were freeze-dried and stored at -20°C before reconstitution in water at the moment of use.

2.2.2 Non-MR Equipment

Anaesthesia equipment and heating pads were supplied by Vet Tech Solutions Ltd. Syringe pumps were supplied by Harvard Apparatus (model# PHD 2000). Physiological monitoring and warm air heating equipment were supplied by SA Instruments. Low density polyethene (LDPE) tubing to allow administration of substances over distance to animals within the MRI system was supplied by Smiths Medical (cat# 800/100/120). Metabolic cage measurements were conducted using a Columbus Instruments Comprehensive Lab Animal Monitoring System (CLAMS).

2.2.3 Animals

All experiments complied with the United Kingdom Animals (Scientific Procedures) Act 1986. Apart from the animals derived from a dietary study (see below), mice were all C57BL/6 WT or *ob/ob* males aged 8-12 weeks (Harlan UK). Upon arrival, they were acclimatised for at least 7 days prior to any experimentation. Mice were kept grouped in individually ventilated cages (IVCs) at 22°C, 70% humidity, and a 12:12 (6.30am-6.30pm) light-day (LD) cycle. Unless otherwise stated, mice had free access to water and a standard mouse diet (RM3, Special Diets Services Ltd., Essex, UK). The afternoon before the start of any procedures, animals were transferred to a local holding room where they were housed singly near the MRI system to reduce the effect of transit stress on any subsequent experiment.

The animals used to show the effect of diet on MEMRI were derived from a dietary study (n=8 normal fat, n=9 high fat fed; raw data kindly provided by Jelena Anastasovska). Animals were similar to those described above, the main difference being that the mice were not supplied directly from Harlan; they were offspring of purchased breeding pairs, with MR performed at around 14 weeks. Instead of RM3, normal (3.6%) or high fat (12.4%) diets supplied by Harlan were provided from weaning.

2.2.4 Metabolic Cage Measurements

Mice (n=6 per group, total=24) were sorted into four groups of equal body mass, and housed singly in CLAMS cages. After overnight acclimatization, by group mice were each injected i.p. with 200μl of either 0.9% saline, or $MnCl_2$ at a dose of 40, 60 or 100mg kg^{-1} (0.318, 0.477 and 0.795μmol g^{-1} respectively). For six hours following injection, optical beams monitored ambulatory and rearing activity, while respiration rate was monitored by O_2 and CO_2 measurements. Telemetry was processed into 30min time bins. CLAMS conditions were otherwise the same as for IVCs. These experiments were kindly performed and analysed by Jim Parkinson.

2.2.5 Static MEMRI Injection Regimen

For two days prior to imaging, mice were injected i.p. twice daily (6am and 6pm) with either 7μl g^{-1} 0.9% saline (n=6) or 7μl g^{-1} 45μM ghrelin (n=7; 0.315nmol g^{-1}, from reconstitution of the 9nmol freeze-dried ghrelin in 200μl water). At 8am on the second day 6.36μl g^{-1} 50mM $MnCl_2$ (0.318 μmol g^{-1}, 40mg kg^{-1}) was injected i.p.

2.2.6 Animal Preparation for MRI

Unless otherwise specified, MRI was commenced between 7am and 10am to reduce circadian physiological variance. Anaesthesia was induced in a small transparent chamber with 3% isoflurane delivered in O_2 at 2L min^{-1}. During anaesthesia maintenance, breathing rate was monitored with a pressure transducer, and temperature monitored using a rectal probe. If i.v. substance administration was to be required at any point, anaesthesia was maintained at 2-2.5% isoflurane in 1L min^{-1} O_2 delivered via a custom-made snug snout mask, during which time the tail was cannulated with a 27G butterfly needle, and temperature maintained by clickable sodium ethanoate heating pads. For MR acquisitions mice were either laid prone on a bed and placed in a custom-made head restraint for head scanning or laid prone without restraint for whole body. Anaesthesia was then maintained at 1.5% isoflurane in 1L min^{-1} O_2, also delivered via a snug snout mask. Temperature was maintained by a computer controlled warm air heating system receiving feedback from the rectal probe.

2.2.7 MEMRI Acquisitions

All 3D gradient-echo images were acquired at 9.4T using a Varian Unity INOVA console running VnmrJ 1.1D software and a 40mm long 30mm i.d. quadrature birdcage transmit-receive RF coil. Whole head shimming was performed manually. Images were converted from VnmrJ FDF to NIfTI-1 format (Cox et al., 2004) using ImageJ (Rasband, 1997-2008). Fast spin echo image acquisitions were similar, but used a Varian DirectDrive console and VnmrJ 2.2B software, with image reconstruction and conversion to NIfTI-1 format (Cox et al., 2004) carried out using custom written code in MATLAB (The Mathworks, Natick, MA, USA).

2.2.7.1 3D gradient-echo timecourses for dynamic MEMRI

A ge3d sequence was used with the following parameters: *TR*=25ms, *TE*=2ms, flip angle=20°, matrix=256×128×128, FOV=38.4×19.2×19.2mm (voxel size=150μm isotropic) and 2 averages, volume acquisition time=13m 39.2s. Eight volumes were acquired, giving a total acquisition time of 1hr 49m 13.6s. From the beginning of the second acquisition, unless otherwise stated 100mM $MnCl_2$ was infused i.v. by a syringe pump at a rate of 8μl g^{-1} body weight hr^{-1} using an infusion pump, to a total volume of 5μl g^{-1} (i.e. 0.8μmol g^{-1} hr^{-1} for 37m 30s, total dose 0.5μmol g^{-1}).

2.2.7.2 2D fast spin echo timecourses for dynamic MEMRI

An fsemsp sequence was used with the following parameters: *TR*=1800ms, *TE*eff=5.6ms (echo spacing=5.6ms, 6 echoes, k-space centre=1), matrix=192×192, FOV=25×25mm, 46 axial slices of 0.4mm thickness (voxel size=130×130×400μm) and 2 averages, volume acquisition time=1m 55.2s. 66 volumes were acquired, giving a total acquisition time of 2hrs 6m 43.2s. Where dosed by whole body mass, $MnCl_2$ administration was the same as for 3D gradient-echo timecourses, but from the beginning of the fourth acquisition. Where dosed by lean body mass, infusion was at a rate of 8.70μl g^{-1} lean body mass hr^{-1}, to a total volume of 5.42μl g^{-1} (i.e. 0.736μmol g^{-1} hr^{-1} for 37m 30s, total dose 0.542μmol g^{-1}).

2.2.7.3 3D gradient-echo for static MEMRI

A ge3d sequence was used with the following parameters: *TR*=54ms, *TE*=2ms, flip angle=24°, matrix=256×128×128, FOV=36×18×18mm (voxel size 141μm isotropic) and 2 averages, volume acquisition time=29m 29s. Four volumes were acquired, giving a total acquisition time of 1hr 57m 56s.

2.2.8 Measurement of Adiposity and Lean Body Mass Using MRS

^1H spectra were acquired at 4.7T using a Varian DirectDrive console running VnmrJ 2.2B software and a 100mm long 40mm i.d. quadrature birdcage transmit-receive RF coil. Whole body shimming was performed manually. An spuls sequence (the standard supplied pulse sequence for acquiring ^{1}H spectra) was used with the following parameters: *TR*=10s, spectral width=20kHz, 4 averages. Raw data were then exported to MestRe-C software (Santiago de Compostela University, Spain). Here, it was fourier transformed, an exponential line broadening of 1.5Hz applied, then manual phase and baseline correction. The lipid peak was determined by integration in reference to the water peak. Lean mass and adiposity were determined using a standard formula (Mystkowski et al., 2000):

$$\%adiposity = \frac{100 \times integral_{lipid}}{integral_{lipid} + integral_{water} + (0.38 \times integral_{water})}$$

2.2.9 Animal Numbers Used in Infusion MEMRI Experiments

2.2.9.1 Optimization of Image Acquisition Protocol

sems vs ge3d vs fsems comparison: n=4 per group, sems data was kindly provided by Owais Chaudhri, total=8/12

ge3d fed vs. fasted experiment: n=4 fed and n=5 fasted, total=9

2.2.9.2 Effects of Changing Infusion Rate and Duration

n=3 per group for dose of 0.3μmol g^{-1} hr^{-1}, n=5 for 0.8μmol g^{-1} hr^{-1}, total=8

2.2.9.3 Effects of Adjusting $MnCl_2$ Dose by Lean Mass in Animals of Varying Adiposity

dosing regime	**fed**	**fasted**	***ob/ob***
whole body mass	4	5	3
lean body mass	4	5	9

Whole body mass raw data kindly provided by Mohammed Hankir, total=21/30

2.2.10 MRI Data Analysis

SNR was determined by dividing signal in a particular ROI by the average of 4 measures of standard deviation of noise, each of these taken from a corner of the image filled with air (i.e. no signal) and free from artefacts. CNR was determined similarly but using signal difference in the ROI between pre- and post-contrast. A full treatment of functional data analysis methods is given in Chapter 3. Briefly, timecourses (dynamic MEMRI images) were motion corrected using SPM5 and normalised using a combination of tools from FSL and AFNI to a standard mouse brain template (Dorr et al., 2008), or in the case of 3D gradient-echo images, to each other. Mn uptake was assessed in individual mice by a GLM analysis in the FSL tool FEAT, using a Gaussian smoothing kernel of 0.5mm and two models of Mn uptake (outside and inside the BBB) as independent explanatory variables. These models were derived from a brain-only 2-dimension constrained MELODIC analysis of separately acquired dynamic MEMRI data. Unless otherwise stated parameter estimate images were thresholded at $Z>2.3$ and the resulting clusters tested for significance at $p<0.05$ using random field theory, correcting for multiple comparisons. Group analysis of Mn uptake across mice was also performed within FEAT, with the same thresholding parameters. For AP normalization, timecourses were adjusted such that all had an AP signal enhancement of 40%.

Static MEMRI analysis was simpler. A mean of the four images acquired from each single scanning session was calculated and these means were normalised to an in-house brain template. The in-house brain template was a manually segmented Mn-enhanced ge3d brain-only image derived from a head image similar to the one shown in the middle column of Figure 2.4 on page 63. Images were then signal intensity (SI) normalised by making the SI of either the whole brain, pituitary gland or scalp muscle the same across all animals. Voxel-voxel statistical analysis was then performed within AFNI.

2.2.11 Other Statistical Methods

T-tests were performed in Microsoft Excel 2007. Group body weights are given as mean±SEM (standard error of the mean). Metabolic cage data was analysed using a 2-way ANOVA within GraphPad Prism (GraphPad Software, CA, USA) with time and injection group as factors.

2.3 Results

2.3.1 Optimization of Image Acquisition Protocol

2.3.1.1 3D gradient-echo

Previous MEMRI data was acquired using a simple 2D multislice spin-echo (sems) sequence with a very coarse spatial resolution. Since hypothalamic appetite centres are small and irregularly shaped, this creates a risk of substantial partial volume artefacts. In addition, the images only had a rostro-caudal FOV of 10mm (Chaudhri et al., 2006; Kuo et al., 2006, 2007; Parkinson et al., 2009; So et al., 2007).

The adult mouse brain is approximately 15mm long in the rostro-caudal axis, so depending upon positioning the olfactory bulbs, cerebellum or brainstem would be cut off. To maintain high spatial resolution in all three dimensions is difficult since slice selection becomes very inefficient at low slice thicknesses. So it is better to use an imaging method based purely on fourier encoding (frequency and phase) for all three dimensions (usually frequency encoding one direction and phase encoding two). Full excitation with spin-echoes, although more T_1-sensitive and less susceptible to distortion from field inhomogeneity, is far too slow for fully 3D imaging, so it is best to switch to partial excitation with gradient-echoes.

A change in the extent of partial volume artefacts and a lower temporal resolution can cause changes in the ability to observe T_1 changes in relevant anatomical areas. These changes cannot be predicted based on MR signal equations and existing data. Hence not only must we ensure that any new 3D gradient-echo imaging protocol is Mn-sensitive, but the fundamental experiment to determine if a protocol has any capability to observe the effects of appetite related stimuli- a fed-fasted experiment (Kuo et al., 2006)- also needs to be repeated.

A comparison of 3D gradient-echo images to the previous 2D multislice spin-echo acquisition protocol (n=4) both before and after $MnCl_2$ infusion is presented in Figure 2.4. Image acquisition parameters, SNR and CNR data from these images are presented in Table Table 2.1. The 3D gradient-echo images have much greater spatial coverage (whole brain rather than partial) and resolution (3.375 vs. 12.74 10^{-6} mm^3 voxel volume) plus better SNR (20.8±1.6 vs. 12.7±1.0) and CNR (5.8±0.6 vs. 4.4±0.3) compared to the 2D multislice

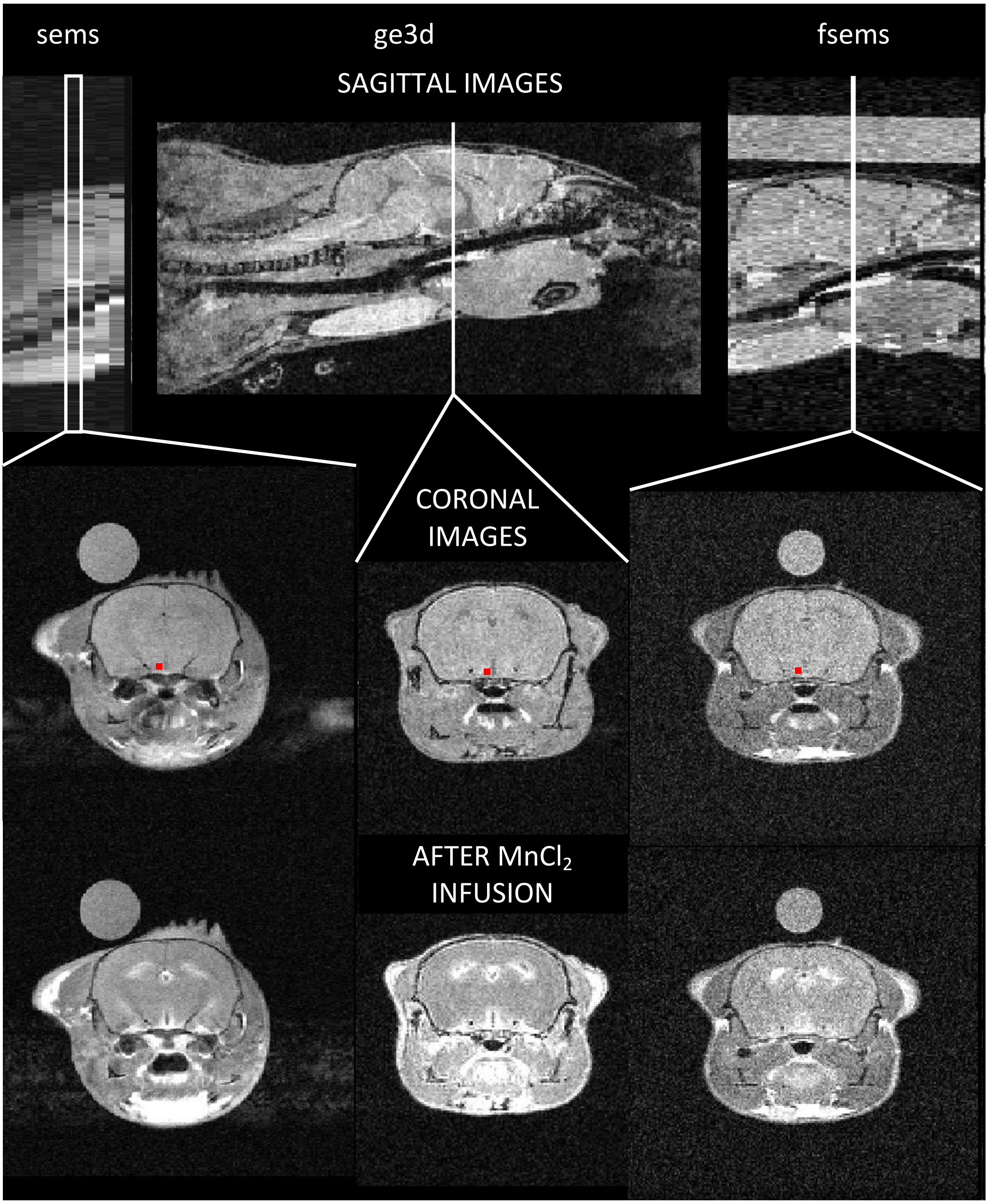

Figure 2.4: examples of unprocessed single timepoint dynamic MEMRI images acquired using the previous (sems, left column) and two new MR sequences (ge3d, middle column, fsems right column) in sagittal (top row) and coronal orientation before (middle, first timepoint) and after (bottom, final timepoint) $MnCl_2$ administration. sems and fsems images were taken with a saline phantom placed above the head- none was included in the ge3d acquisitions as at the time these images were acquired there were problems shimming the system that could only be solved by removing the phantom. The red square indicates the location of the region used for SNR and CNR measurements described in Table Table 2.1, and roughly corresponds to the location of the VMH. Raw data for the sems images kindly provided by Owais Chaudhri.

Parameter	**sems**	**ge3d**	**fsems**
Acquisition time	1m 55.2s	13m 39.2s	1m 55.2s
Timepoints in ≈2hr scan	66	8	66
Spatial coverage (mm)	25×25×10	19.2×19.2×38.4	25×25×18.4
Voxel dimensions (μm)	98×130×1000	150×150×150	130×130×400
Voxel volume ($\times 10^{-6}\mu m^3$)	12.74	3.375	6.76
SNR	12.7±1.0	20.8±1.6	11.3±0.5
CNR	4.4±0.3	5.8±0.6	5.1±0.5

Table 2.1: comparison of old (sems) and new (ge3d, fsems) acquisition protocols. SNR and CNR were determined using the ROI of fixed size described in Figure 2.4

spin-echo method. The pattern and extent of enhancement appears to be the same or better. The temporal resolution of this protocol was very low (13m 39.2s vs. 1m 55.2s acquisition time), but given the higher CNR and smaller voxel size, it was felt that as long as the Mn infusion profile across animals was stable then there would be enough images to accurately assess Mn uptake in brain nuclei, whether by an ROI-based analysis or a voxel-voxel one.

To test this improved acquisition protocol in an appetite environment, mice were either fed normally (n=4) or fasted (n=5) for 12-16hrs overnight prior to MEMRI using the 3D gradient-echo dynamic MEMRI protocol. The images were spatially normalised to each other and analysed using FEAT. A t-test map of differences in Mn uptake between fed and fasted groups is presented in Figure 2.5 (uncorrected for multiple comparisons). Even with these low sample sizes, differences in Mn uptake between fed and fasted mice can be seen in many areas such as the posterior hypothalamic and periaqueductal areas, hippocampal fimbrae, paraventricular hypo- and thalamic nuclei, prelimbic cortex, olfactory bulb glomerular layer and the medial and ventral orbital cortices. However, these areas are mainly associated with olfaction (Purves, 2001), emotion and stress (Herman et al., 2005; Morgane et al., 2005; Vertes, 2006) rather than control of appetite. Lowering of the statistical threshold, or even completely removing it failed to reveal any trend towards differences in Mn uptake in the appetite centres of the hypothalamus. Not seeing fed-fasted differences in the ventral hypothalamus was disappointing, and in disagreement with previous findings using a different MR sequence (Kuo et al., 2006).

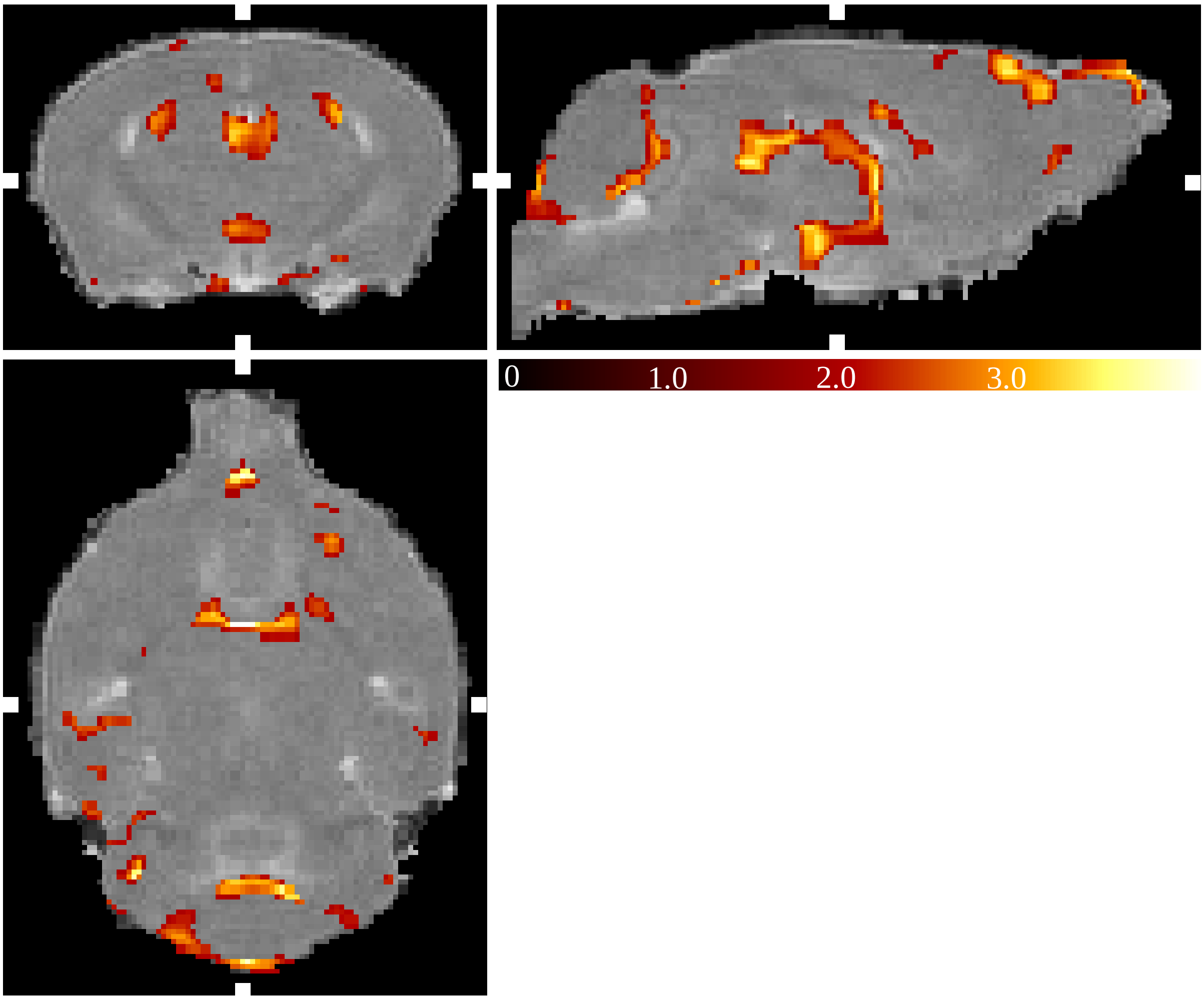

Figure 2.5: t-test map showing fasted>fed differences in enhancement (none were detected for fed>fasted) after a 3D gradient echo dynamic MEMRI experiment between overnight fasted (n=5) and fed (n=4) mice. Colours represent Z-scores according to the scale bar and are thresholded at $p<0.05$ without correction for multiple comparisons. Coronal, sagittal and transverse sections are shown, sliced at the positions indicated by the white notches.

2.3.1.2 2D fast spin echo

One application where the 3D gradient-echo protocol would have far too low a temporal resolution is imaging the response to peptide injections. These occur over short timescales, possibly within the acquisition period of just one volume. Therefore an alternative is required for more rapid imaging. The previous 2D multislice spin-echo protocol only acquired one echo per excitation. In principle, more echoes can be acquired during relaxation. Limiting factors to this idea include the gradient duty cycle which determines how rapidly the frequency- and phase-encoding gradients can be applied, and heating from RF pulses.

The sems sequence made very little use of the full capabilities of the available hardware, so there was tremendous scope for using these capabilities to improve the sequence in terms of spatial resolution and coverage, Mn-sensitivity and temporal resolution. It was decided to use a set of sequence parameters that would make no compromises in any of these terms, and hopefully make substantial improvements in all four.

The parameters of the new fast spin echo sequence (fsems), which aquires data more rapidly than sems by collecting multiple echoes per excitation, is described in section Section 2.2.7.2 of the Materials and Methods on page 59. A direct comparison of the two sets of parameters is shown in Table Table 2.1. The resulting images, before and after $MnCl_2$ administration, are shown in Figure 2.4. As with ge3d, the pattern and extent of enhancement appears the same or better than that for sems. Temporal resolution was kept the same (1m 55.2s acquisition time), while spatial coverage (whole brain rather than partial) and resolution in the rostro-caudal axis (0.4 vs. 1mm thick slices) was vastly improved. Mn sensitivity (CNR) also increased (5.1 ± 0.5 vs. 4.4 ± 0.3) due to the choice of a more appropriate TR (1800 rather than 600ms), placed between the pre- ($\approx$1900ms) and post- ($\approx$1700ms) Mn T_1 times of the hypothalamus (Kuo et al., 2005). Ideally it would have been lower than the pre-Mn time, but this was not possible given the time required by the pulse sequence to acquire data from all the slices and echoes.

Figure 2.6 shows the results of a t-test between fed (n=4) and 12-16hr overnight fasted (n=5) mice scanned by MEMRI using this fsems sequence, with the images normalised before analysis in FEAT. Despite a much greater Mn-induced signal change in the fasted group

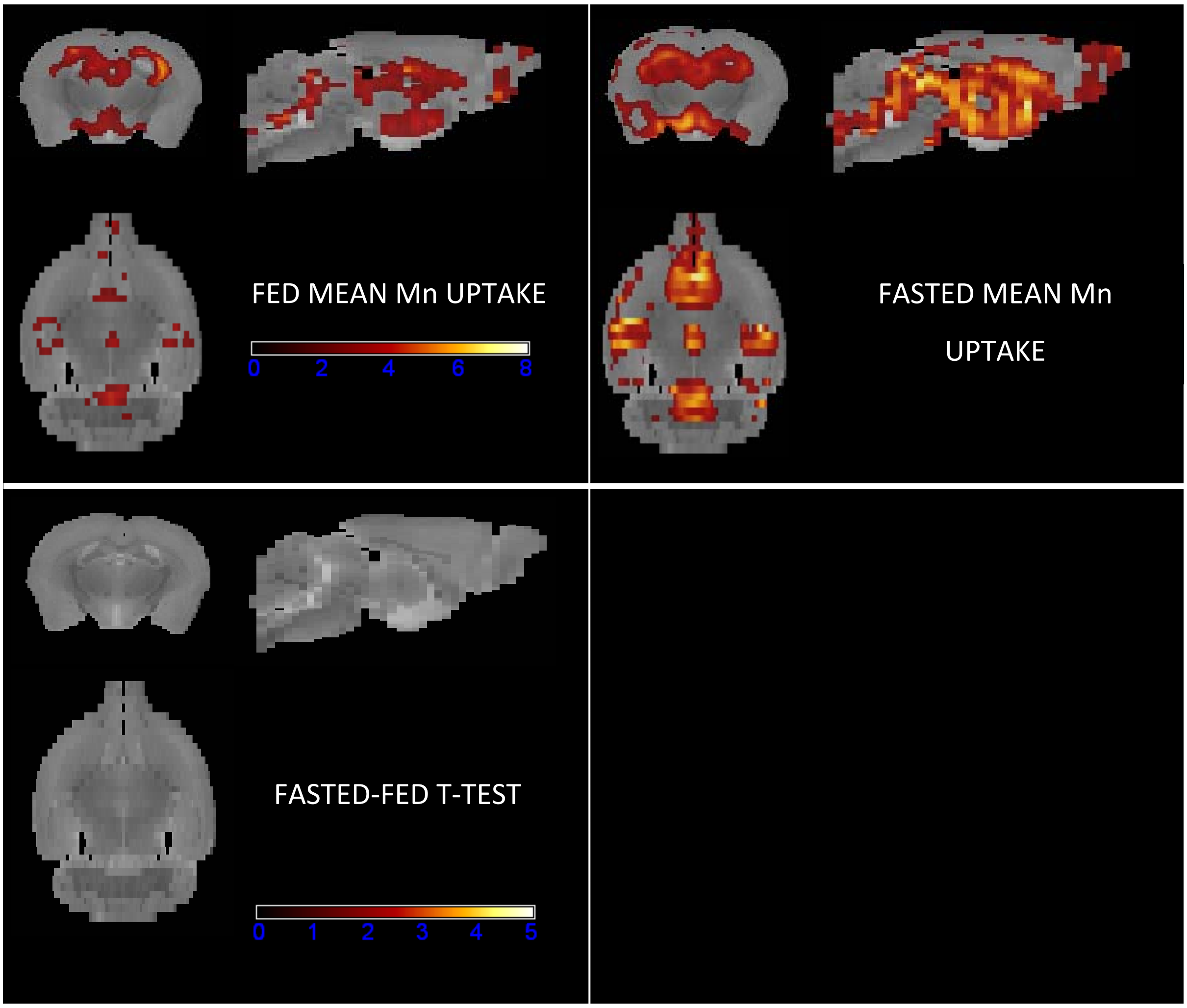

Figure 2.6: statistical maps showing the Mn-induced signal change in fed (n=4) and overnight fasted (n=5) mice scanned by fsems. Also shown is a t-test of fasted>fed differences in enhancement. Colours represent z-scores according to the scale bar, thresholded at $Z>2.3$ and the resulting clusters tested for significance at $p<0.05$ using random field theory, correcting for multiple comparisons.

compared to the fed, these differences were not judged to be significant. Manipulation of thresholds in the same manner as the previous section failed to ameliorate this situation.

2.3.2 Effects of Changing Infusion Rate and Duration

Based on previous ROI-based analyses (Chaudhri et al., 2006; Kuo et al., 2006, 2007; Parkinson et al., 2009; So et al., 2007), the current pulsed infusion protocol produces two quite distinct patterns of Mn intake in the rodent head. One is very responsive to the Mn intake, occurring outside of the brain and in the cerebrospinal fluid (see Figure 3.3 on page 91). The other is much less responsive, occurring within the brain. This can be confirmed across the whole brain with a MELODIC analysis (for details see Chapter 3, specifically Figure 3.4 on page 92). If a peptide were to be injected as part of a MEMRI experiment, these complex profiles would make it very difficult to assess what the Mn uptake response to the peptide was, independent of the background signal increase caused by the pulsed $MnCl_2$ infusion. It would be better to have a simple background of a straight line increase. These two experiments were designed to test two ways of achieving this.

2.3.2.1 Continuing the 0.8μmol g^{-1} hr^{-1} $MnCl_2$ Infusion for the Entire Post-Baseline Period Leads to a High Mortality Rate

The 3D gradient-echo dynamic MEMRI protocol was used on three mice with the following change to the $MnCl_2$ infusion: 8μl g^{-1} hr^{-1} (0.8μmol g^{-1} hr^{-1}) for the entire duration post-baseline (approximate total volume of 12.7μl g^{-1}, total dose 1.27μmol g^{-1}) rather than a pulse of 8μl g^{-1} hr^{-1} (0.8μmol g^{-1} hr^{-1}) for 37m 30s. Unfortunately the $MnCl_2$ infusion, despite being within that which should be tolerated by rodents (Lee et al., 2005), produced a very high mortality rate (5/5 animals died before the end of the scanning period). This is a very small number of animals for a formal toxicology study, but given that the primary purpose of this study was to determine what dose regimen produces good contrast, as opposed to what doses are tolerable without substantial mortality, it was felt that the number of deaths was enough to discontinue any further attempts at using this dose regimen.

2.3.2.2 Stretching the $MnCl_2$ Dose Across the Entire Post-Baseline Period Leads to Poor Enhancement

The 3D gradient-echo dynamic MEMRI protocol was used on three mice with the following change to the $MnCl_2$ infusion: $3\mu l\ g^{-1}\ hr^{-1}$ ($0.3\mu mol\ g^{-1}\ hr^{-1}$) for the entire duration post-baseline (approximate total volume of $4.78\mu l\ g^{-1}$, total dose $0.478\mu mol\ g^{-1}$) rather than a pulse of $8\mu l\ g^{-1}\ hr^{-1}$ ($0.8\mu mol\ g^{-1}\ hr^{-1}$). A typical timecourse of images is shown in Figure 2.7. Although this protocol had a perfect survival rate, the enhancement was very poor. Again, this is based on a very small sample size, but as before it was felt continuing any further would waste animals.

2.3.3 Effects of Adjusting $MnCl_2$ Dose by Lean Mass in Animals of Varying Adiposity

The primary confounding factor in MEMRI experiments of energy balance or appetite control is the possible difference in body weight caused by appetite-related stimuli. The main contributor to that weight difference is usually altered adiposity. Since this tissue is relatively inert with respect to Mn uptake (A. Koretsky, *pers comm*, Lee et al., *in prep*), if $MnCl_2$ was administered proportional to body weight, fatty animals would receive an inappropriately high dose of Mn, and leaner animals the opposite. The effects of this can be seen in Figure 2.8. Here, two groups of animals were fed different diets; the first group a normal fat diet (NF; body weight 22.5±0.7g; n=8), the second group a high fat diet (HF; 24.9±1g; n=9; t-test p=0.06). The mice were then scanned using the fsems dynamic MEMRI protocol and enhancement represented by statistical maps of signal change due to Mn uptake. Despite the consequent analysis complications, a pulsed $MnCl_2$ dose was used based on the results of experiments in section Section 2.3.2.

As can be seen the HF mice had greater enhancement than the NF group, a difference that reached statistical significance in numerous parts of the brain including parenchymal areas such as the paraventricular nucleus of the hypothalamus, olfactory bulb and cerebellum. This greater enhancement could have been due to higher neuronal activity. However, it is also seen in many non-parenchymal brain regions such as the lateral ventricles. Unless these non-parenchymal

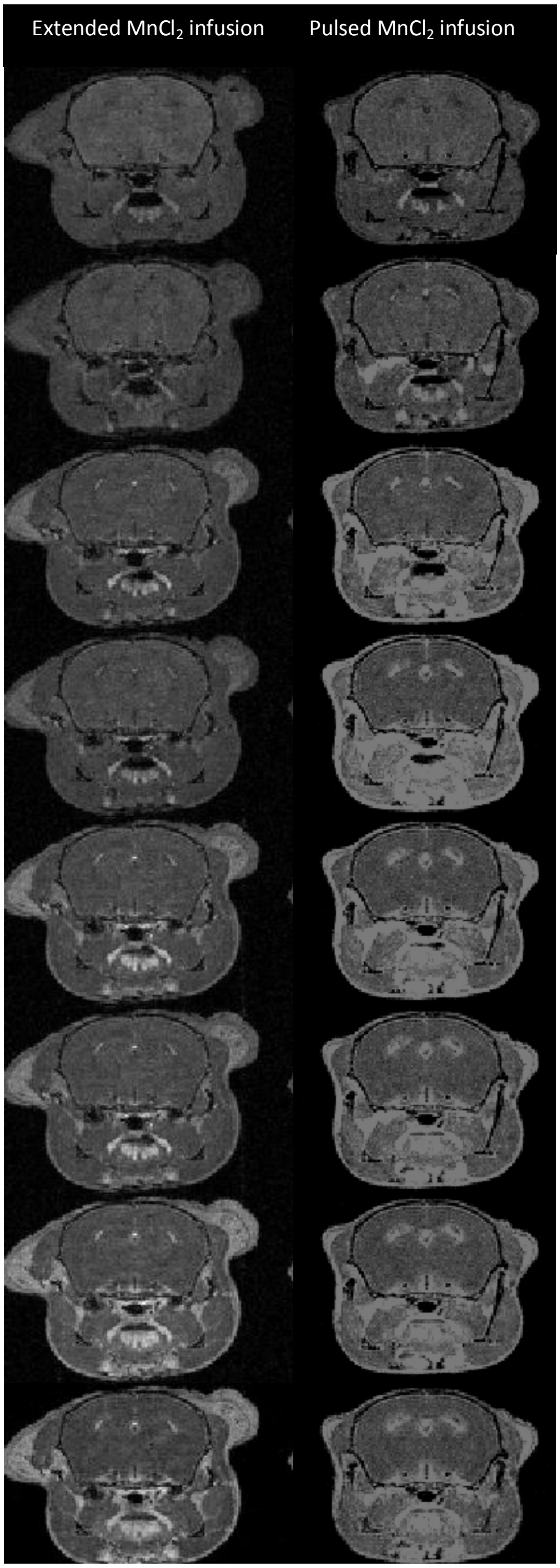

Figure 2.7: timecourse of images from ge3d acquisitions with a low extended $3\mu l\ g^{-1}\ hr^{-1}$ $MnCl_2$ infusion rate and a $8\mu l\ g^{-1}\ hr^{-1}$ pulse for 37m 30s (both provide a $4.78\mu l\ g^{-1}$ total dose). Images run from top to bottom. The first image is a baseline when no $MnCl_2$ was being infused. The infusion began at the start of the 2nd acquisition. Each timecourse covers a total of 1hr 49m 13.6s.

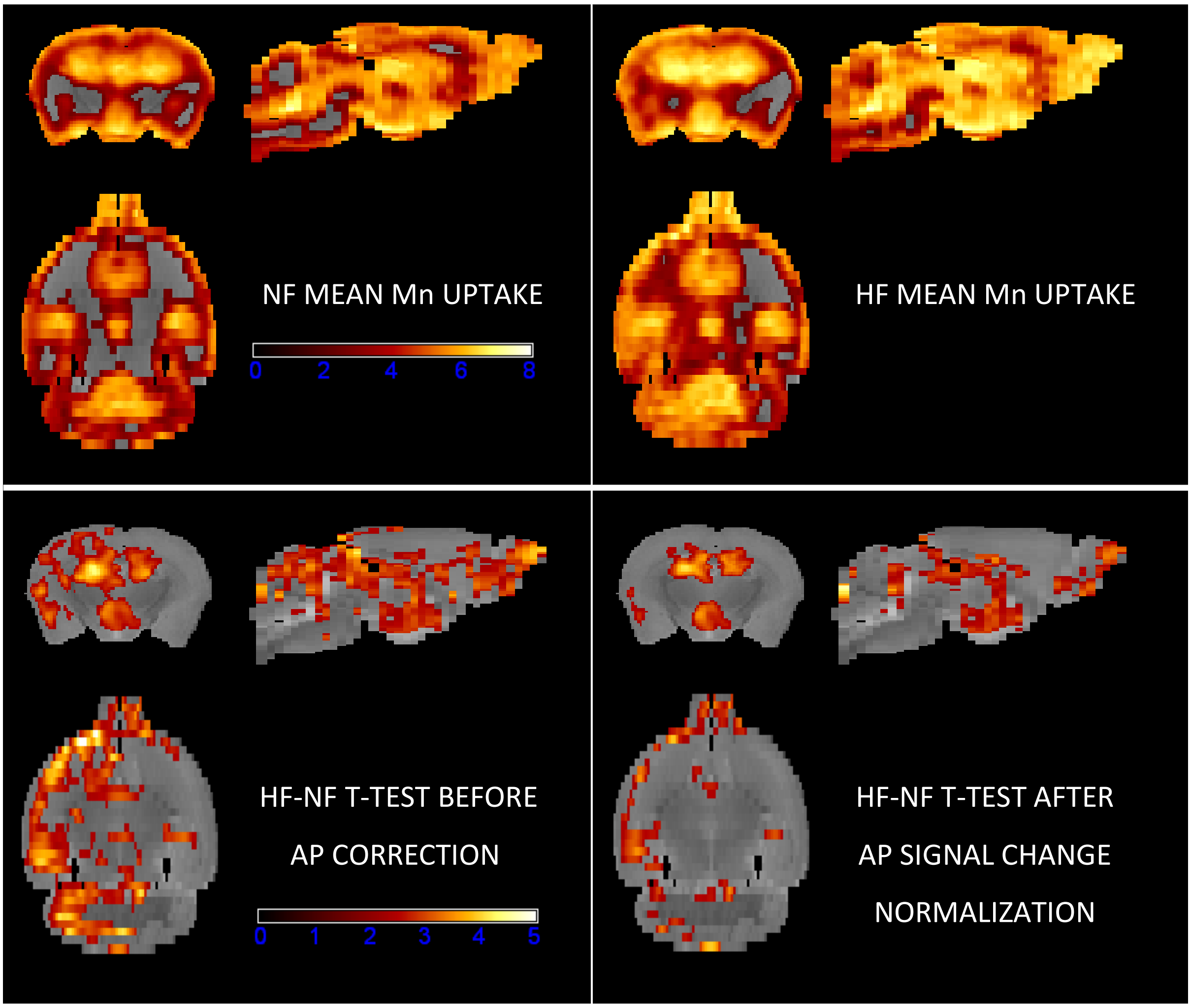

Figure 2.8: coronal, sagittal and transverse section statistical maps showing signal changes due to Mn uptake after an fsems dynamic MEMRI experiment in mice fed a normal diet (n=8, top left), high fat diet (n=9, top right), and t-test maps of differences in uptake between those two groups before and after $MnCl_2$ dose correction by normalization of the signal change in the AP (a surrogate of $MnCl_2$ dose). Colours represent Z-scores according to the respective scale bars, thresholded at $Z>2.3$ and the resulting clusters tested for significance at $p<0.05$ using random field theory, correcting for multiple comparisons. Raw data kindly provided by Jelena Anastasovska.

areas receive similar levels of enhancement between groups of animals, it must be concluded the results are confounded by $MnCl_2$ dose. The same mice had their adiposity measured by MRS, and this reveals a possible source of the dosing error: the NF group had a mean adiposity of 15.1±1.6%, the HF group an unsurprisingly higher level of 20.8±2.1% (t-test $p=0.04$). Thus the HF group may have received a higher dose into the brain as a consequence of having a greater proportion of adipose tissue. It should be noted that there is a marked degree of laterality in these images, with the source probably being the mean HF image. The larger enhancement on its left side than right would explain the laterality in the subsequent t-test images. Lateral MR artefacts in 1-2 mice can cause laterality in the detected mean MR enhancement maps of small groups of animals; however, manual inspection of the raw MR data did not reveal any obvious laterality in any of the mice, hence an explanation for the emergence of laterality at the group level cannot be given.

One possible way to remove this confound is to normalise the images to a region that we are confident is not influenced by the stimulus under test, and which can act as an accurate indicator of what the $MnCl_2$ dose was. Energy balance is of so much importance to the survival of an animal that appetite-related stimuli can potentially influence the activity of any brain region, so we must look to outside regions. One possible structure is the pituitary gland, which lies ventral to the hypothalamus and whose signal intensity is not modulated significantly by appetite-related stimuli (Kuo et al., 2006, 2007). It has the added advantage of being flush with the ventral side of the brain- thus during spatial normalization of the brain the pituitary gland becomes spatially normalised too, allowing automated and objective measurement of its signal intensity change. Presented in Figure 2.8 is a t-test conducted after images had been adjusted such that their signal increase in the pituitary gland anterior lobe had been fixed at 40%. Unfortunately, even with this correction, there is still a substantial amount of non-parenchymal difference in enhancement, primarily in the lateral ventricles.

Thus the problem must be tackled at source by infusing an appropriate dose of $MnCl_2$ in the first place. An easy metric which if measured could aid in preventing this problem is lean mass, which can be assessed by MRS. The aim of this experiment was to determine if dosing $MnCl_2$ in proportion to lean mass results in similar levels of enhancement in non-parenchymal areas regardless of adiposity. This was tested in two situations, 1) the standard fed-fasted experiment discussed earlier (to ensure anaesthesia for MRS does not act as a confound in appetite-related experiments), and 2) an extreme adiposity scenario- mice that became fat for genetic reasons (*ob/ob*), whose percentage adiposity is several-fold higher than wild type mice (Bray and York, 1979; Ingalls et al., 1950). In the case of *ob/ob* mice, dosing by lean mass is especially important since dosing by whole body mass for MEMRI in 5 animals of 8-10 weeks age weighing 40-42g resulted in 5/5 animals dying. This is admittedly a low sample size, but such high mortality is more likely to be due to inappropriate dosing than any other factor. Figure 2.9 shows statistical maps of Mn uptake in these three groups of mice after a 2D fast spin echo dynamic MEMRI experiment. Also presented are t-test maps of differences in Mn uptake between the three groups. The Mn uptake maps indicate that despite there being no systematic difference in lean mass between fed (19.3±0.6g; n=4) and 12-16hr overnight fasted (19.4±0.9g; n=5) groups (t-test p=0.95), and in fact no significant difference in pre-fast body weight, upon which a whole body weight $MnCl_2$ dose would have been based (20.5±0.6g vs. 20.5±0.7g, t-test p=1.00) fasted mice still had more enhancement in non-parenchymal ventricular regions than fed. The *ob/ob* group (n=9, whole body mass 43.7±0.9g, lean mass 22.4±0.7g) is more enigmatic, with a peak intensity of Mn uptake similar to the fasted group, but an extent of Mn uptake similar to the fed group. Despite this, the only significant differences found were between fed and fasted groups. These were all in parenchymal areas associated with modulation of olfaction (Purves, 2001), emotion and stress (Herman et al., 2005; Morgane et al., 2005; Vertes, 2006) rather than control of energy balance: periaqueductal area, hippocampal fimbrae, paraventricular thalamic nuclei, prelimbic cortex, olfactory bulb glomerular layer and the medial and ventral orbital cortices. This is a similar pattern to the previous 3D gradient-echo fed-fasted experiment (see Figure 2.5), but lacking hypothalamic regions.

The enhancement pattern in the fed and fasted mice of Figure 2.9 is much stronger than that in Figure 2.6, which is surprising given that it is a similar experiment, with the only substantial difference being the dosing regimen. This should not produce such great differences in enhancement since the two sets of mice were of the same age and strain, and both lean. T-tests between the two t-test maps, between the two fed enhancement maps (n=4 vs. n=4) and

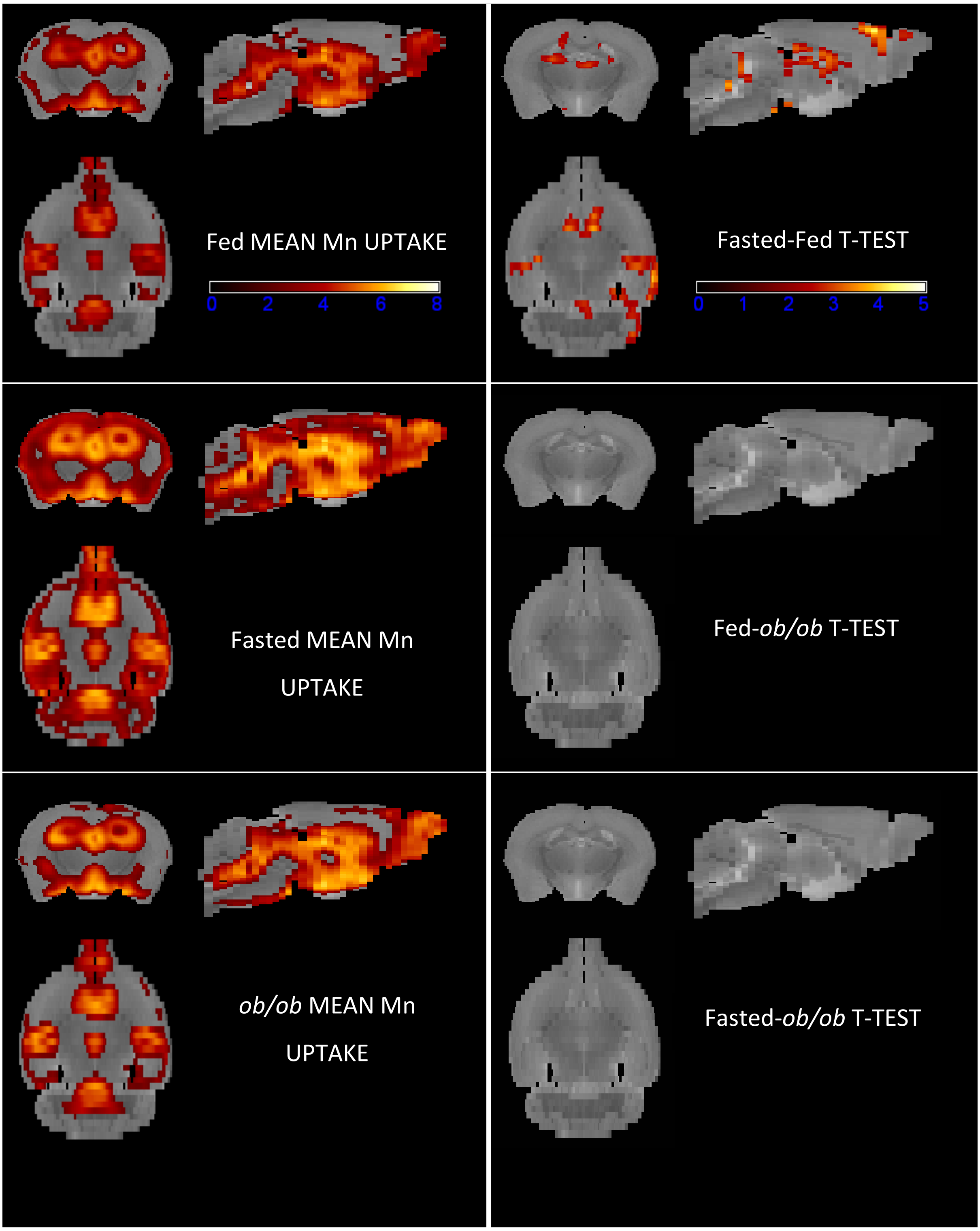

Figure 2.9: statistical maps of mean signal enhancement (left) and t-tests (right) in a fsems dynamic MEMRI experiment in groups of mice fed normally (n=4), fasted overnight (n=5) or which are leptin deficient (*ob/ob*; n=9), and dosed by lean mass. Colours represent Z-scores according to the scale bars, thresholded at $Z>2.3$ and the resulting clusters tested for significance at $p<0.05$ using random field theory, correcting for multiple comparisons.

between the two fasted maps (n=5 vs. n=5) did not produce any significant differences, though given the low sample size this is not surprising. The most likely explanation for these results is variance consequent of low sample size.

2.3.4 i.p. MEMRI for Appetite Studies is Confounded by Weight Loss

The studies presented so far all suffer from one major confound- the use of anaesthesia to prevent motion artefacts. The alternative is restraint or neuromuscular blockade of conscious animals (Peeters et al., 2001). This is very stressful, and so best avoided, especially when studying behaviours such as appetite that are sensitive to stress.

One of the disadvantages of MEMRI can be turned into an advantage that removes the anaesthesia confound. Unlike with haemodynamic markers and contrast agents, Mn has a very low flux through the brain. This limits its temporal resolution, both because of a slow response time, and the long duration required for Mn to flush out before an experiment is repeated in the same animal. However, it also means that effects on Mn uptake last throughout the whole of a chronic stimulus. Hence, in conjunction with $MnCl_2$ administration, a stimulus could be applied outside of the magnet while the animal is freely moving and conscious. The effect of the stimulus would be left as an increase in Mn accumulation, something which could be imaged later without risk that the Mn would disperse. Temporal resolution is lost, though a simple non-lethal method of measuring brain activity such as this one is still valuable, especially if it can be applied many times over an animal's lifetime to track longitudinal effects.

The principle of this static (as opposed to dynamic) MEMRI was demonstrated in the first paper of functional MEMRI (Lin and Koretsky, 1997), though it was not fully exploited until 2005. The more recent studies (Yu et al., 2005, 2007, 2008) exploited it to investigate the function of the auditory cortex in mice. This system was particularly suited for study by static MEMRI for three reasons: 1) auditory stimuli can be applied constantly and without restraint after $MnCl_2$ administration; 2) scanner noise, which would present substantial practical difficulties in a dynamic MEMRI experiment, should have no effect on a static MEMRI experiment due to little potential Mn flux at the time of acquisition; and 3) parts of the brain could be found that were not modulated by auditory stimuli, and hence could be used to normalise the signal intensity of images prior to any comparisons. Normalization substantially reduces inter-animal variability in signal intensity from sources such as differences in gain and SNR between scanning sessions. The authors were able to observe different patterns of Mn uptake in response to different sound tones in a manner that matched the known tonotopy of the auditory cortex as determined by electrophysiological studies.

As with dynamic MEMRI studies, dose could be an important confound. In the auditory study, this was adjusted to body weight. Since these mice were lean and had similar body weights both within and between groups, this was an adequate method of adjustment. However, as explained in the previous section, in an appetite experiment where body composition can differ between groups, this can lead to biased results. Thus if this technique was ever to be used on animals with systematic differences in body weight and composition, dosing would have to be given more careful consideration.

Here, it was decided to first try out static MEMRI on lean animals given a three-day short course of injections with the potent orexigenic hormone ghrelin, with a control group given injections of a similar volume of vehicle (saline). Ghrelin is an endogenous orexigenic hormone secreted by a number of organs and tissues, most importantly the stomach, whose secretions achieve peak concentration prior to a meal (Kojima and Kangawa, 2005; Kojima et al., 1999; Tschöp et al., 2000), hence ghrelin has a putative role in meal initiation. It acts via the arcuate nucleus Kojima and Kangawa (2005) and has previously been shown to affect the signal in MEMRI experiments (Kuo et al., 2007).

Unlike with the dynamic MEMRI, there was no prior information available on what effect the $MnCl_2$ dosing regime would have on the appetite-related behaviours of the mice (Kuo et al., 2007). This is important to determine since although high $MnCl_2$ doses produce the greatest T_1 change (and hence make available a larger signal for modulation by a stimulus), they can also have confounding neurotoxic effects. To achieve this mice (n=6 per group, total=24) were assigned to one of four $MnCl_2$ dose groups (saline, 40, 60 and 100mg kg^{-1}). After acclimatization to metabolic cages, they were injected i.p. and monitored over period of several hours for ambulatory movements and respiratory activity. The results are presented in Figure 2.10. It appears that there is no difference amongst the dose groups, including saline

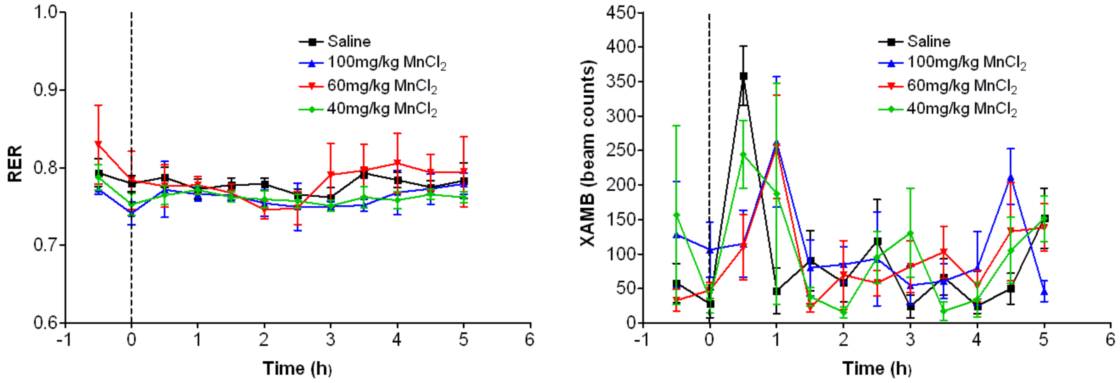

Figure 2.10: metabolic cage data showing the effect of different doses of $MnCl_2$ administered i.p. RER is the respiratory exchange ratio (CO_2/O_2 inspired, normally 0.8). Error bars are of SEM. XAMB is ambulatory activity in the surface of the cage. The dotted line represents the time of injection. Data collection, analysis and graphing courtesy of Jim Parkinson.

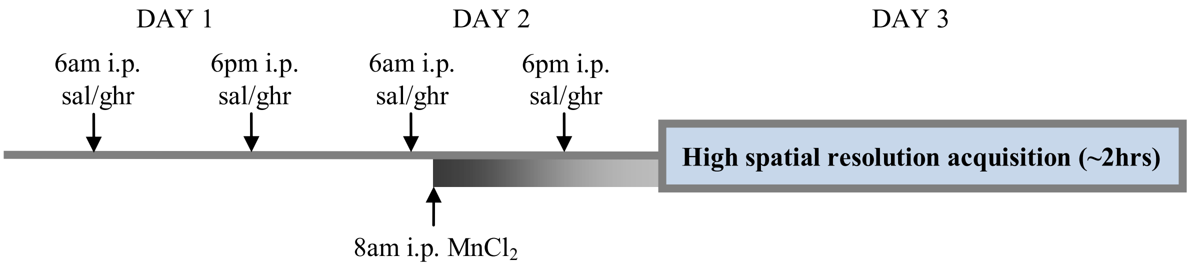

Figure 2.11: schematic of static MEMRI protocol used here (compare to Figure 2.2). $MnCl_2$ is injected i.p., and 24 hours later an anatomical scan is acquired to measure Mn uptake.

(injection group effect for RER data p=0.67, XAMB p=0.83). Although this would indicate that the highest dose should be chosen, it was decided to use a low 40mg kg^{-1} dose that had previously been used very successfully in the auditory study (Yu et al., 2005).

The setup of the experiment is described in Figure 2.11. The injection regime was chosen to minimise the total number of injections required, but still allow enough injections to acclimatise the mice to the stress of i.p. injection, thus removing the confound of injection stress during the period of Mn uptake.

The ghrelin-injected group should experience changes in neuronal activity in the hypothalamus relative to the saline, and an associated increased food intake over the period of injection. This should also result in a systematic body weight difference between the two groups. However, it is likely to be a very small difference, so it was decided to dose $MnCl_2$ by total body weight rather than lean mass. This may seem to contradict the principles behind the

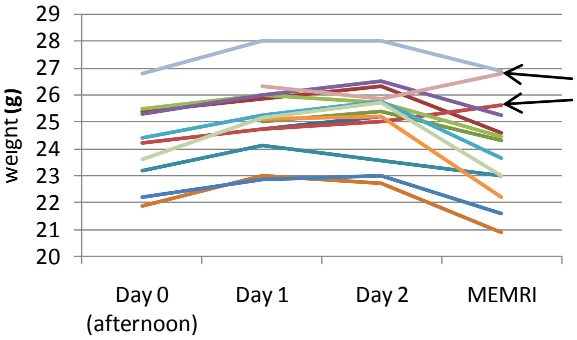

Figure 2.12: body weight changes during the static MEMRI experiment. Each coloured line represents an individual animal. Weights were measured around 8am, apart from on Day 0 when they were measured in the late afternoon (hence these are lower). Not all mice had their weights measured, and not all timepoints were measured for each mouse. MEMRI occurred in Day 3. Arrows highlight the two mice whose body weight did not drop on Day 3.

experiments of the previous section, but dosing by lean mass is not devoid of problems. The foremost is that animals have to be anaesthetised for MRS. This is a potentially confounding mild stressor, and if it can be avoided it should be. Since the systematic body weight differences found here were small (Day 2 saline 24.5±0.7g vs. ghrelin 26.1±0.4g, t-test p=0.07), it was decided that dosing by body weight was a more reasonable course to take than subjecting the animals to MRS in order to dose $MnCl_2$ by lean mass.

Figure 2.12 shows the changes in body weight of all the animals over the period of the injection regimen. As can be seen, the animals tolerated the injections on Day 1 well, but not those on Day 2, with a consistent drop in body weight of around 10% in most of the animals by Day 3 (25.4±0.5g vs. 23.7±0.6g, 1.7g drop, paired t-test $p=1.78\times10^{-5}$). Anecdotal observation implicated the $MnCl_2$ injection, which led to visible lethargy in most animals minutes after administration. Supporting this idea were the two mice whose weight did not drop- the MEMRI data collected the next day indicated that they had not taken up any $MnCl_2$

An example of pre- and post- enhancement images is shown in Figure 2.13. No difference in enhancement was found between saline and ghrelin-injected groups (now n=5 vs n=6 respectively rather than n=6 vs. n=7 since the two mice that did not take up Mn^{2+} were excluded) under any of the tested normalization schemes (to whole brain, pituitary gland or scalp muscle SI).

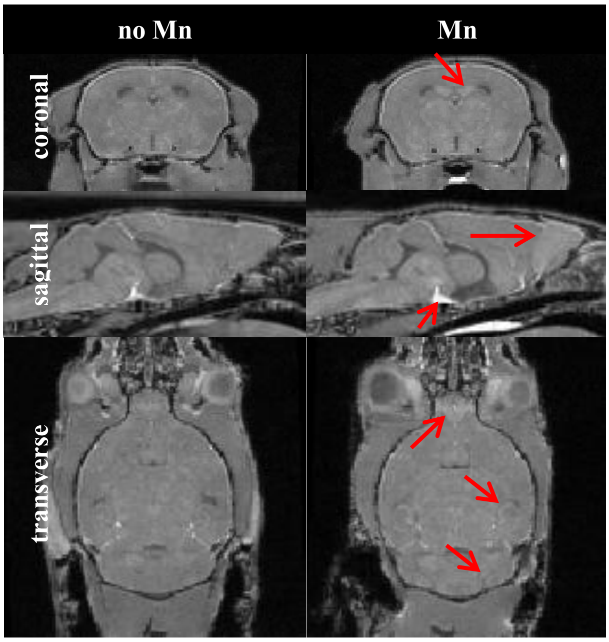

Figure 2.13: example pre- and post-i.p. $MnCl_2$ images from two mice, both scanned using the protocol described in Section 2.2.7.3 and Section 2.2.5 using saline as the stimulus, but with $MnCl_2$ only administered to the mouse on the right. Coronal, sagittal and transverse sections are presented. Red arrows indicate areas of substantial enhancement, often on just one side for clarity.

2.4 Discussion

The experiments described in this chapter aimed to correct a number of deficiencies in the protocols previously used for MEMRI studies. The first set of changes aimed to alter the image acquisition to collect data on the whole brain at higher spatial resolution. The first attempt, using 3D gradient-echo, achieved this with a great deal of compromise in temporal resolution. The protocol did enable differences to be observed between fed and fasted mice (a strong appetite-related stimulus), but not in the hypothalamic regions that should be most responsive. Instead, differences were found mainly in areas related to stress and emotion. Given the low sample size (n=4 fed, n=5 fasted), firm conclusions cannot be drawn from this. However, fasting is also a very strong reliable stimulus, and producing this curious result deserves some consideration. It is entirely plausible that stress and emotional centres are stimulated by fasting. What is puzzling is that hypothalamic and brain stem centres sensing appetite are not affected, which they should be given 1) they were shown be strongly stimulated before (Kuo et al., 2006), 2) are directly affected by the stimulus and 3) are circumventricular so receive more Mn which makes any Mn uptake difference more likely to be observed. The increased uptake in stress centres is an indicator that animal handling stress could have confounded the experiment, although this is unlikely as great effort was put into reducing this, and there is no reason to believe it should systematically have affected the fasted mice more. Another possibility is that in the previous study (Kuo et al., 2006) there were strong differences in the same non-hypothalamic areas identified here- however the ROI-based analysis used was inherently unable to find them. If these were stronger than the hypothalamic differences, one interpretation of the current results is that the experiment was too insensitive to detect hypothalamic differences, but could detect non-hypothalamic ones.

Another alternative, especially given so many differences were found in periventricular regions, is that this experiment is sensitive to brain volume changes during fasting as opposed to just activity. Even mild osmotic stressors are able to induce brain volume changes in both animals and humans (McManus et al., 1995), including in regions such as the cerebral cortex (Cserr et al., 1991) and ventricles (Puri et al., 1999). Fasting reduces water consumption and blood glucose levels (Apostolou et al., 1976), so it could plausibly alter brain volume too. An experiment to test for this would involve acquiring images in both fed and fasted animals but without the $MnCl_2$ infusion.

The statistical maps displayed in Figure 2.5 are uncorrected for multiple comparisons. Although this is an undesirable situation, both voxel and cluster-level correction eliminated any significant difference between fed and fasted groups. One strategy that could ameliorate this is the use of adaptive thresholding with anatomical pre-masks (for examples see Hammers et al. (2002, 2003)). The pre-mask excludes volumes where no change is expected (e.g. if one was interested in ventricular size change, it would be a mask only covering the ventricles and periventricular regions), reducing the size of the multiple-comparisons problem, and increasing the chances that small differences in signal can be detected. This is a valid strategy in infusion MEMRI, where large parts of the brain do not take up Mn and hence no difference in MEMRI signal can be observed in the first place- any pre-mask for MEMRI would exclude these regions.

In any case, it appears that the great reduction in temporal resolution is too much of a compromise. Hence, the alternative of using fast spin echo was explored. This acquisition made no compromises, had a higher spatial resolution and coverage than the previous protocol and higher Mn-sensitivity with the same temporal resolution. However, none of these changes increased the SNR and CNR substantially, so the temporal noise problem (described in the introduction to this chapter and Figure 2.3) that prevents functional temporal resolution was not resolved. One possible reason for not achieving better results with sequence changes is that a systematic analysis and computer simulation of available sequence parameters such as that carried out by Cleary et al. (2009) for phenotyping cardiac defects in *ex vivo* murine embryos was not performed here. Instead, parameters were chosen based around estimates of what should maximise contrast given the known T_1 and T_2 times of the pre- and post-Mn hypothalamus given constraints of acquisition time, FOV and required spatial resolution. Thus, optimal parameters may well have been missed, and as such the sequence comparison here is not an objective general comparison of sems vs ge3d vs fsems, but more a narrow comparison between the three unoptimised acquisition protocols chosen here. Since the ge3d acquisitions did not include a phantom, it was not possible to conduct an objective noise comparison across all three sequences. However, looking at the sems and fsems images, the fsems phantom and background do seem considerably noisier than that of the sems images, rather than approximately equal as the ROI data suggest. This is not contradictory, since while the ROI data is based on an ROI of equal size across all acquisitions, the fsems voxel volume is approximately half that of the sems, i.e. not equal size, reducing the available signal and thus appearing to increase the noise level. Thus this jump in visible noise is likely caused more by reduced slice thickness than a deficiency of fsems *per se*. Nonetheless, it is still a large increase, and even the SNR data indicate that the fsems sequence used here has a lower SNR than sems, albeit with a higher CNR. This deficiency could have negatively influenced the ability of subsequent experiments using fsems to observe changes in Mn uptake. Such problems are unlikely to have affected the ge3d sequence, whose background noise levels appear similar to those of fsems, in line with the results of the ROI SNR data.

The next set of changes was to the infusion profile. These stretched the dose across the whole timecourse, or continued the dose rate for the entire duration. Unfortunately, neither of these strategies was successful; the dose stretching resulted in poor enhancement apart from towards the latter stages, and the continued dose rate had high mortality rates, despite being within the range that should prevent this from happening (Lee et al., 2005). It appears the current pulsed infusion protocol (Chaudhri et al., 2006; Kuo et al., 2006, 2007; Parkinson et al., 2009; So et al., 2007) is a good compromise between providing the high concentration of Mn required to encourage rapid uptake of Mn across the BBB, and a low enough total dose to prevent toxicity. Hence it was decided to continue with this old dosing regimen.

The next study used MRS measurements of lean mass the day prior to the MEMRI scan to more appropriately adjust the $MnCl_2$ dose, rather than using whole body mass, a measure which can confound experiments where there are systematic differences in body composition (and hence Mn uptake per unit of non-brain body mass) between groups. Note that this assumes similar brain weight between these groups. The protocol was tested in the extreme situation of fed vs. *ob/ob*, plus the fed vs. fasted experiment. The only differences found were between fed and fasted groups, and these were mild and in non-hypothalamic areas, although this could be due to low sample size. Unfortunately similar Mn enhancement was not observed across groups in non-parenchymal regions such as lateral ventricles. Given that dosing by lean mass should prevent this happening, it may in fact be the case that the stimuli involved were so powerful that they did indeed cause genuine changes in Mn uptake in non-parenchymal areas. This is certainly a possibility with *ob/ob* mice. These are deficient in the hormone leptin, encoded by the *ob/ob* gene (Zhang et al., 1994). The *ob/ob* phenotype is largely reversible by leptin administration (Campfield et al., 1995; Halaas et al., 1995; Pelleymounter et al., 1995; Weigle et al., 1995), implying that leptin's primary role is to signal to the brain the levels of adipose tissue. Hence without leptin the energy balance mechanism behaves as if there was no adipose tissue, the response to which is hyperphagia, reduced energy expenditure and increased adiposity- the *ob/ob* phenotype. Leptin also holds roles outside of adipose tissue, including on brain development. A consequence of this is that the brains of *ob/ob* mice have reduced weight, altered composition and development compared to wild-type (Ahima et al., 1999; Bray and York, 1979). This is the equivalent of non-adipose body composition being altered, meaning that dosing $MnCl_2$ by lean mass is not enough to ensure a fair dose reaches the brain of *ob/ob* mice- the earlier stated assumption of similar brain weight between groups is violated. Any conclusions made about Mn uptake in *ob/ob* mice are confounded by this, and could explain any differences in uptake of Mn in non-parenchymal areas when compared to WT. How fasting could cause such differences is less certain, though a 12-hour fast induces such profound changes in physiology that it should not be surprising that this happens. Regardless of which of these hypotheses is true, dosing $MnCl_2$ based on MRS results of lean mass may not be fully robust since in addition to the inherent error of MRS (Mystkowski et al., 2000), there can also be differences in lean mass composition that alter Mn uptake (as with *ob/ob* mice). Thus it appears the most appropriate arena for this method would be where only diet varies between groups- and hence any difference in body composition will be dominated by adipose tissue. Unfortunately it was not possible here to test this method on mice that had been fed different diets.

The final study used the static MEMRI method which removes anaesthesia confounds at the cost of having no temporal resolution. Unfortunately the $MnCl_2$ injection on Day 2 proved to be an even bigger confound, producing a robust weight loss in most of the animals injected. This was puzzling given that the metabolic cage studies and previous reports (Yu et al., 2005, 2007) had provided no indication that this would happen. Animals being injected for MEMRI visibly looked lethargic and unhealthy for the post-$MnCl_2$ injection period, although systematic behavioural analysis was not conducted. The behavioural changes are unlikely to be due to injection stress since the two injections on Day 1 never caused such a loss of body weight. In addition, the third injection on Day 2 did not cause behavioural changes. It is possible that having two i.p. injections in such close temporal proximity caused the problem though unlikely since there were two mice that were injected with $MnCl_2$ but had no body weight loss and with no Mn uptake. This implies that it is Mn uptake in the brain that causes the lethargy. Great effort was put into reducing i.p. injection stress, such as rapid and gentle handling of the mice, minimal needle insertion, small injection volumes of 7μl g^{-1}, habituation to the same handler (the candidate) and prior to $MnCl_2$ injection, habituation to needle insertion (via the saline and ghrelin injections). Weight loss could also have been due to i.p. presence of the acidic $MnCl_2$ irritating the peritoneal cavity, though no post-mortem was carried out to confirm this.

An alternative to i.p. injection, despite the technical difficulty, would be to use i.v. injection, though the dose would have to be much lower if given as a bolus due to potential acute toxic effect. Another would be to anaesthetise the animal and infuse a large dose of $MnCl_2$ though this adds the anaesthesia confound back, albeit in a much milder form.

Chapter 3

Automated Analysis of MEMRI Data

3.1 Introduction

One of the primary advantages of using MRI for studying brain activity is that unlike many other methods, it is able to capture information across the whole brain. This creates a large amount of information, and ideally all of it should be used otherwise interesting phenomena may be overlooked.

A framework for semi-automated and relatively unbiased whole brain analysis of neuroimaging data was originally developed for PET images (Fox et al., 1988; Friston et al., 1991). The advent of haemodynamic fMRI coincided with both an increased availability of computational power and improved image manipulation and statistical methods. These were quickly adapted for fMRI since many of the principles are the same as for PET (Friston et al., 1995a,b; Turner et al., 1998). An overview of the framework is presented in Figure 3.1. It can be split into two independent processes- spatial normalization and statistical analysis, with the latter taking its input from the former.

Automated statistical analyses necessarily assume that any given image co-ordinate is comparable across images- i.e. it represents the same anatomy across those images. This means that images must be spatially normalised otherwise co-ordinates will represent different anatomies, making any comparison incorrect, or at least increasing variance due to spatial error. This is what spatial normalization of images is for, and it functions well for rodent haemodynamic fMRI studies. This is because the images are very similar to those from

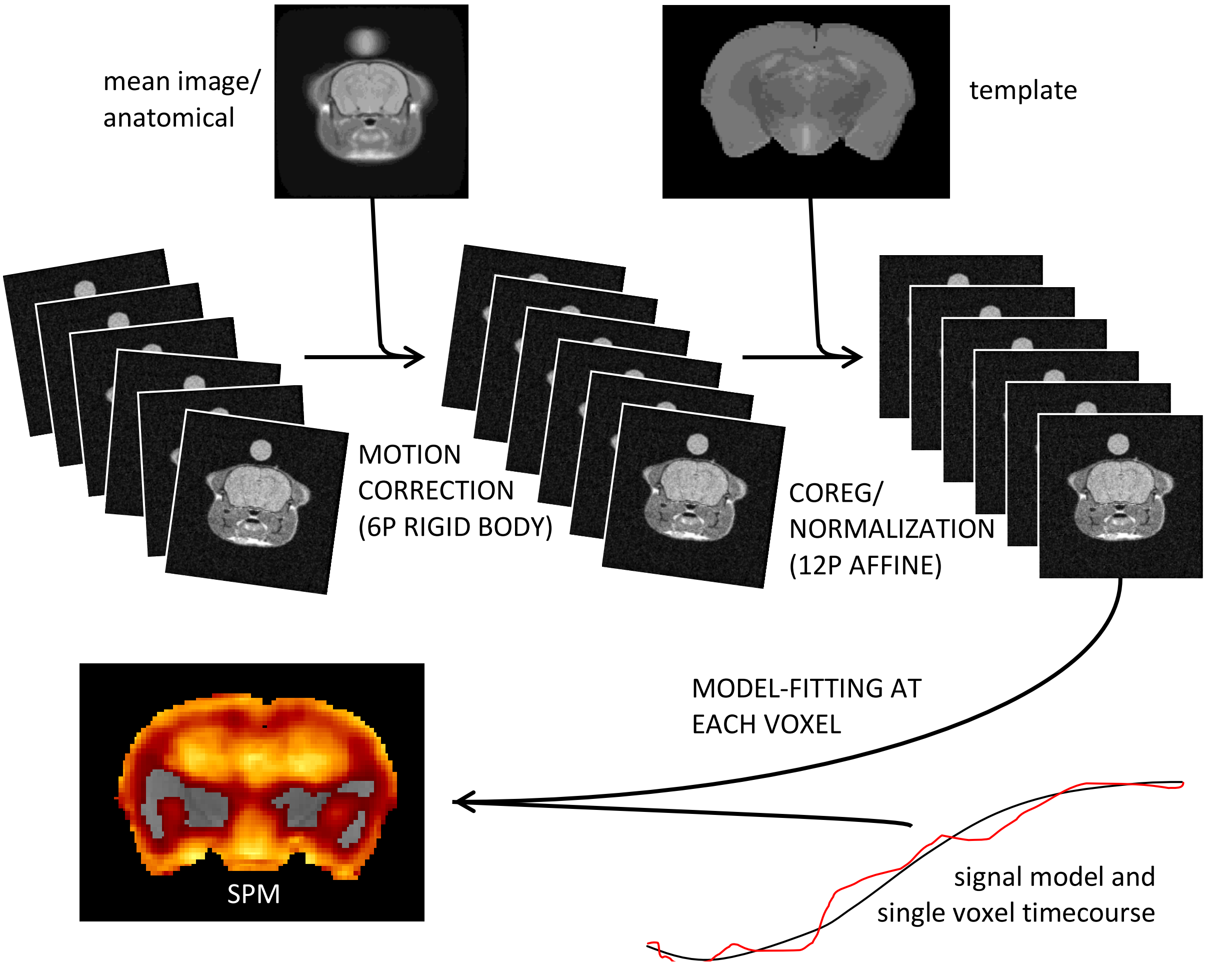

Figure 3.1: overview of automated data analysis framework. Image timeseries are first motion corrected using 6 transformation parameters (3 translations and 3 rotations) before 12 parameter spatial normalization (additional 3 scalings and 3 skews) to a standard space template. There are many different combinations of registration processes that can be used to achieve this; whichever way, the aim is the same- to produce timeseries that are all in the same space. This data is then fed into statistical analyses where models of signal change are fitted at each voxel to produce statistical parametric maps (SPMs).

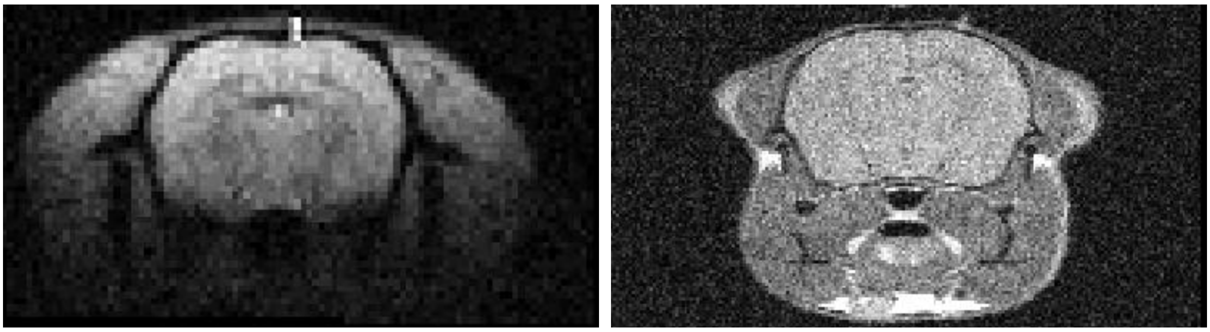

Figure 3.2: comparison of a typical T_2^*-weighted rat BOLD-fMRI image acquired using a surface coil (left) with a T_1-weighted image acquired for a MEMRI experiment in the mouse using a volume coil (right). Images are both of a slice through the hypothalamus. The rat image is 0.5mm thick, the mouse one 0.4mm. More problematic areas in the rostro-caudal extremities are not shown.

human haemodynamic fMRI, with the majority of signal originating from the brain, and a clear separation from the scalp (Figure 3.2, left). Also presented in Figure 3.2 on the right is a raw MEMRI image. The T_1-weighting means these properties are no longer true- the majority of signal originates from outside of the head, and there are a number of areas where it is not very clear where the boundary is between the brain and the scalp. Towards the rostro-caudal extremities of the brain, the situation can become much worse, with no separation between the olfactory bulbs, nasal cavities and trigeminal nerve, or between the cerebellum and the back of the skull. Much of the tissue outside of the brain is non-rigid. In principle this should not be problem for registration, since the standard registration algorithms do not always assume a body is rigid (i.e. can only be rotated or translated)- they can handle the other linear transforms of scalings and skews too. Except in the case of gross anatomical deformities, linear transformation is likely to be adequate for rodent brains, since there is little nonlinear deformity between brains of the same age and strain (Chen et al., 2006; Kovacevi et al., 2005). However, the rest of the head can experience nonlinear transforms, such as dilation of the oesophagus, and the movement of the jaw about its hinge. These changes violate the assumptions of the standard registration methods. Nonlinear registration could be used, but is computationally expensive and often requires a substantial investment in teaching software what a head 'looks like' so that it can automatically segment out different structures and ensure that both local and global registrations are correct. Alternatively all it has to do is identify and segment out the brain, but since there is little brain scalp separation, this may fail too.

In principle the statistical analysis should not suffer from so many problems. All that is required is a model of signal intensity change over time in a MEMRI experiment. Changes in Mn uptake due to a stimulus would cause changes in SI over time, altering the parameters required to fit the model. However, no such model currently exists, and needs to be developed.

Thus there were two main aims to this series of studies. Firstly, to adapt pre-existing spatial normalization software to deal with the complications of MEMRI images. Secondly, to devise a model of signal change during a MEMRI experiment that could be fitted to the data in order to assess the magnitude and extent of signal changes. The effect of these changes on inference would then be tested against manual ROI-based analyses that they are intended to replace.

3.2 Materials and Methods

3.2.1 Spatial Normalization

Most neuroimaging software analyses, such as those used in functional imaging analysis competition, FIAC (Poline et al., 2006) rely on a single integrated suite of tools. Spatial normalization of rodent head images, which are mostly of non-brain tissue (see Figure 3.2) requires weighting of motion correction and template registration to the brain. The large amount of high signal non-brain tissue means that this cannot be done by simple thresholding. Instead the brain extraction has to be done by edge detection based segmentation. In addition, because the individual images are so noisy, it is better to create a mask for weighted motion correction rather than to inaccurately brain extract each individual noisy image.

There is no available fMRI analysis suite that can sequentially perform weighted rigid body motion correction, brain extraction and affine registration to a template. Hence a mixture individual tools from a number of suites were used.

Baseline images in each timecourse were averaged (in the case of all the MEMRI timecourses presented in this chapter, this means the first three images), and the brain extracted using the FSL tool bet2 (Smith, 2002; Smith et al., 2004) with centre co-ordinates defined by manually locating the centre of the central medial thalamic nucleus. In addition, since bet2 expands a sphere, to improve the performance of the program the mean baseline image was made more spherical (and thus human-shaped) by stretching the image 2-fold in the dorsal-ventral axis and 2/3 (i.e. compression) in the rostral-caudal direction. After running bet2 the extracted brain had these deformations reversed before further use. A mask was created from the extracted brain and used for weighted motion correction of the data in SPM5 (The FIL Methods Group, 2005). The brain extracted mean baseline image was 9-parameter normalised (translation, rotation, stretch/compress) to a standard (Dorr et al., 2008) or in-house mouse brain template using the AFNI tool 3dWarpDrive (Cox, 1996). The in-house brain template was a manually segmented Mn-enhanced ge3d brain-only image derived from a head image similar to the one shown in the middle column of Figure 2.4 on page 63, which provided much better registration performance for the thick-sliced sems images than the template from Dorr et al. (2008). The calculated normalisation parameters were then applied to the motion corrected data to create the spatially normalised timecourse.

3.2.2 sems Fed/Fasted Data

This data came from a previous study, and its collection has been described elsewhere (Kuo et al., 2006). Briefly, reagents, equipment, animal handling and preparation were similar to those described in Sections 2.2.1 to 2.2.3 and 2.2.6 on pages 56 to 58. The differences were in animal age (16-24wks rather than 8-12), time of day for image acquisition (around 9am-12pm rather than 7am-10am), maintenance temperature (35.5°C rather than 37°C), anaesthesia induction (1.5% at 1.5-2L min^{-1} rather than 3% at 2L min^{-1}) and maintenance (1% rather than 1.5%). Note that this previous MEMRI anaesthesia regimen (Kuo et al., 2006) was, in the opinion of and in the hands of the candidate, not reliable enough at producing balanced anaesthesia- hypnosis, analgesia and muscle relaxation (Flecknell, 1996), hence a stronger one was used for other collecting other MEMRI data presented in this thesis. For the fasted group food was removed 12-16h prior to MEMRI. On the morning of the experiment fed mice weighed 27.6g±0.7 (n=4), fasted 29.3g±1.6 (n=5). Dynamic MEMRI acquisitions were performed at 9.4T using a Varian Unity INOVA console running VnmrJ 1.1D software. Whole head shimming was performed manually. A sems sequence was used with a 45mm long 25mm i.d. quadrature birdcage transmit-receive RF coil and the following parameters: *TR*=600ms, *TE*=10ms, matrix=256×192, FOV=25×25mm, 10 axial slices of 1mm thickness (voxel size=98×130×1000μm) and single averages. From the beginning of the fourth acquisition, 62.3mM $MnCl_2$ was infused i.v. by a syringe pump at a rate of 200μl hr^{-1} using an infusion pump, to a total volume of 5μl g^{-1} (around 37mins). Images were spatially normalised (see section Section 3.2.1) to an in-house mouse brain template.

3.2.3 Exploratory Data Analysis for Generation of MEMRI Signal Change Model

The animals used here (n=29) were from a dietary study (raw data kindly provided by Jelena Anastasovska). Briefly, reagents, equipment, animal handling and preparation were similar to those described in Sections 2.2.1 to 2.2.3 and 2.2.6 on pages 56 to 58 with two main differences. Firstly, the mice were not supplied directly from Harlan; they are offspring of purchased breeding pairs. Second, and most importantly, the mice were subjected to varying dietary conditions during gestation, lactation and weaning (diets supplied by Harlan). Some of their mothers received a low protein diet during gestation. Shortly after birth mice were cross-fostered for lactation to mothers receiving a different diet to the one the mice experienced (via their mother) during gestation. For weaning, some mice received a high fat diet. This resulted in mice with a mixture of different body weights and compositions. MEMRI was performed at around 14 weeks with the same fsems image acquisition protocol as in section Section 2.2.7.2 on page 59 but with a Varian INOVA console running VnmrJ1.1D software, and the infusion protocol described for sems MEMRI in the previous section (Section 3.2.2).

After spatial normalization (see section Section 3.2.1) using a standard mouse brain template (Dorr et al., 2008) data were subjected to EDA using the FSL tool MELODIC (Beckmann and Smith, 2004; Smith et al., 2004). After masking out non-brain tissue using the template mask, group ICs thresholded at $p>0.95$ were created using tensor ICA (Beckmann and Smith, 2005).

3.2.4 Other Statistical Analyses

ROI timecourses were extracted using AFNI and exported to the statistical programming environment R, where all subsequent analysis and plotting took place. Statistical images were generated using the FSL tool FEAT with a Gaussian smoothing kernel of FWHM 0.5mm (i.e. approximately 2 voxels, as recommended by Turner et al. (1998) as the minimum for SNR enhancement, reducing inter-individual differences in anatomy and ensuring the datasets constitute a Gaussian random field) and a pre-threshold brain mask applied (derived from the template). Statistical images were thresholded at $Z>2.3$ and the resulting clusters tested for significance at $p<0.05$ using random field theory, correcting for multiple comparisons (Benjamini and Hochberg, 1995; Friston, 1997; Genovese et al., 2002; Worsley et al., 1996).

3.3 Results

3.3.1 Generation of MEMRI Signal Change Model

To run GLM analysis of signal change in an image timeseries usually requires a time-varying covariate model of what the signal change should be. This can be an equation, though in the case of fMRI data it is usually entered as a vector of numbers (or matrix if there are many models to be fitted). When this is fitted to the data, and assuming that noise levels are similar across voxels and timeseries, the strength of fit will be a representation of the magnitude of response according to the model.

The pulsed Mn infusion is likely to lead to a complex signal change profile. To investigate this, ROI timeseries were measured in 8 different head regions of a single fed mouse subjected to sems MEMRI. The results are presented in Figure 3.3. The timecourses appear to fall into two classes. The first class, made up of the 4V, AP, D3V and ME, has a signal that rises rapidly during the $MnCl_2$ infusion then levels off and slowly declines shortly after it ends. The second class, made up of the Arc_RHS, Pe_RHS, PVN_RHS and VMH_RHS has a signal that slowly rises after the infusion starts. The regions in the first class all have an incomplete or no BBB at all, so a signal that rises rapidly with the infusion and starts to decline can be considered to indicate a region outside the BBB. Conversely, the regions in the second class are all inside the BBB.

To see if this relationship extended across the whole brain, 29 image timeseries of fsems MEMRI data from a dietary study in mice (raw data courtesy of Jelena Anastasovska) were

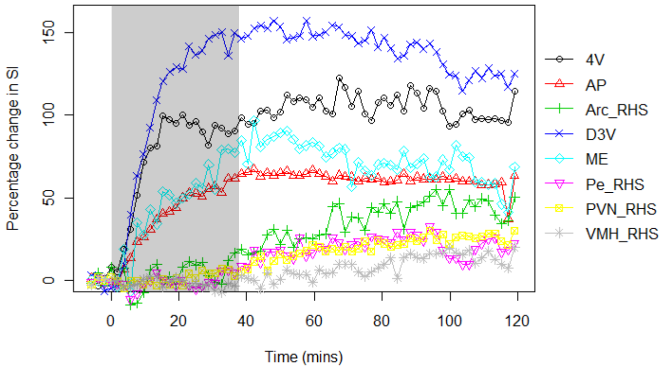

Figure 3.3: timecourses of signal change over baseline during a MEMRI experiment in various different ROIs (see Figure 3.5 for their definition and location). The grey area indicates the period of the $MnCl_2$ infusion. The timecourses appear to fall into two classes; those that rise rapidly upon the start of $MnCl_2$ infusion with a slow decline after it stops (4V, AP, D3V, ME) and those that simply rise slowly, reaching a moderate level of signal enhancement at the end (Arc_RHS, Pe_RHS, PVN_RHS and VMH_RHS). Raw data from which timecourses were derived kindly provided by Yu-Ting Kuo.

subjected to exploratory data analysis using tensor ICA (Beckmann and Smith, 2005). This method pattern searches data for non-Gaussian spatio-temporal signal sources (components). The results of this analysis are presented in Figure 3.4. The software used, the FSL tool MELODIC (Beckmann and Smith, 2004) includes a dimensionality estimation algorithm that estimated the data could be best explained by six independent components. These are presented in the top section of the figure. In total they explain 71% of the total variability in the data. Examination of these also produces two classes. Components 1 and 3 are very similar to each other, both being of the OBBB sort. Components 2 and 4-6 are similar to the IBBB regions in terms of timecourse and spatial location. Thus it was decided to rerun the analysis, but this time constrained to two dimensions. The results of this are presented in the lower section of Figure 3.4. These two components are very similar to the IBBB (upper component explaining 46% variability) and OBBB (lower explaining 20%) sorts respectively, with a total explained variability of 65%. Their associated timecourses are probably good models of signal change in a pulsed infusion dynamic MEMRI experiment. The most important is the IBBB model, since this relates to parenchymal tissue.

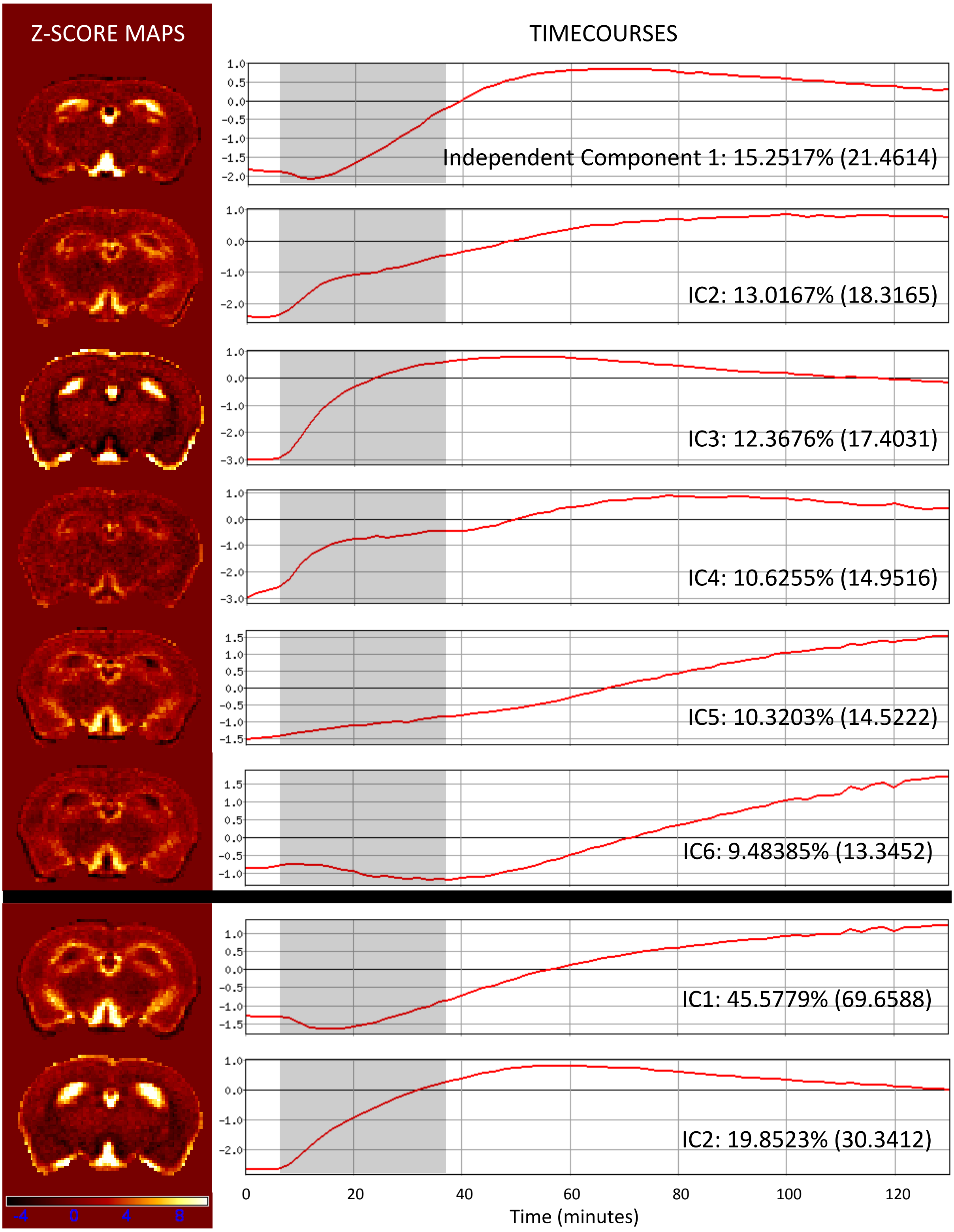

Figure 3.4: group tensor ICA analysis of dynamic MEMRI data from 29 mice. Images are of a slice through the hypothalamus. Each image-timecourse pair represents an IC. The timecourse vertical axis is of normalised response. The grey areas in each timecourse indicate the period of the $MnCl_2$ infusion. Inset in each is that component's percent contribution to the total and (explained) variance. The top six components are from an unconstrained analysis, the bottom two from one constrained to two dimensions. Raw data kindly provided by Jelena Anastasovska .

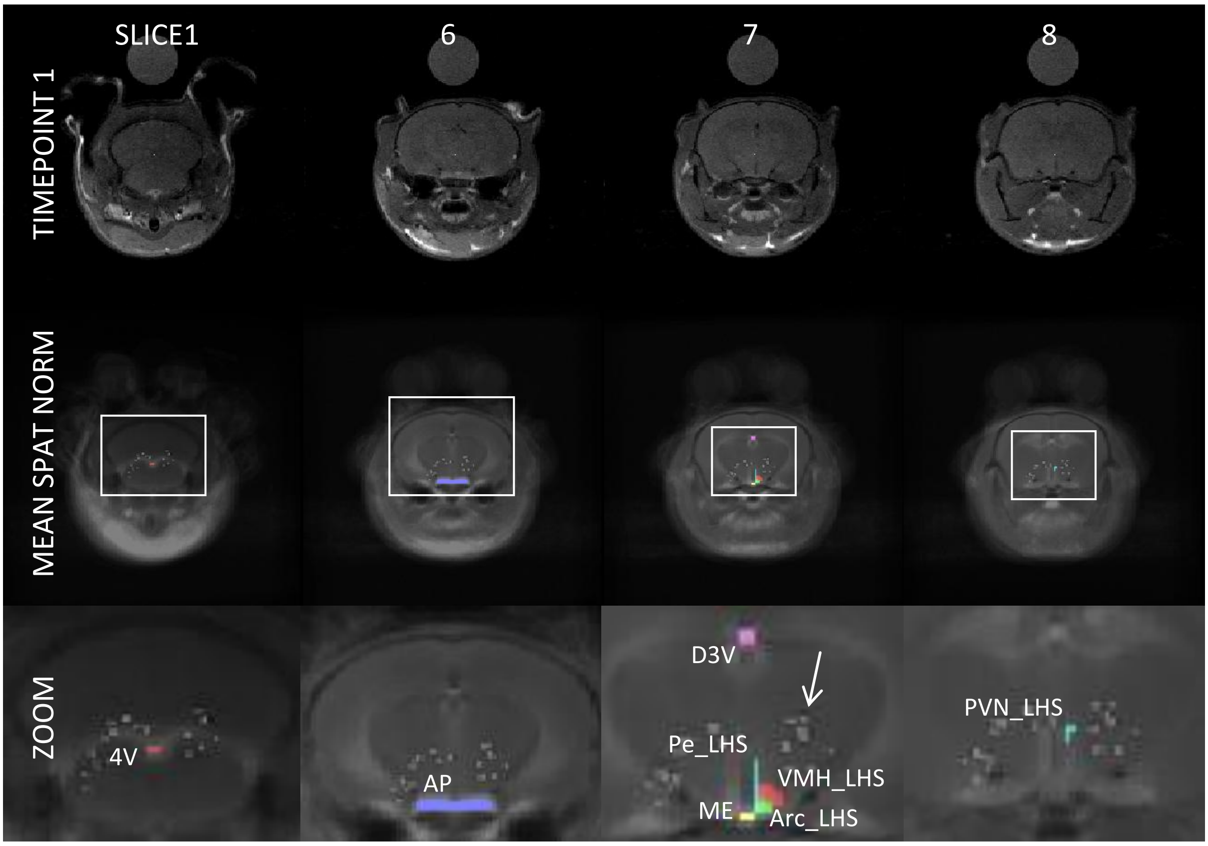

Figure 3.5: comparison of a single timepoint sems image to the mean of all the spatially normalised sems timecourses, plus locations of ROIs used to generate data in Figure 3.4 and Figure 3.6. Zoom images are of the corresponding highlighted region in the mean image. The arrow indicates an example DC offset artefact. Slice1 is the most caudal. See Figure 2.4 for a sagittal image showing the rostro-caudal location of the slices. Raw data kindly provided by Yu-Ting Kuo.

3.3.2 Effect of Spatial Normalization on Analysis of MEMRI Data

This section is a reanalysis of previously reported data (Kuo et al., 2006). The aim was to analyse whole brain data automatically rather than using manually drawn ROIs. The sems fed and fasted data sets were spatially normalised to an in-house mouse brain template. Judging the quality of the spatial normalization is difficult, since registration metrics are normally based on the root mean square (r.m.s.) difference between images or on the sharpness of joint histograms. Since most of the image voxels are in unregistered (non-brain) tissues, and also given how little contrast is present within the rodent brain, these measures will not work. Instead it is best to judge by looking at image overlays, and also seeing the effect of the normalization on the ability to extract similar mean timecourses to before.

A mean of the normalised images images is presented in the second row of Figure 3.5. Much

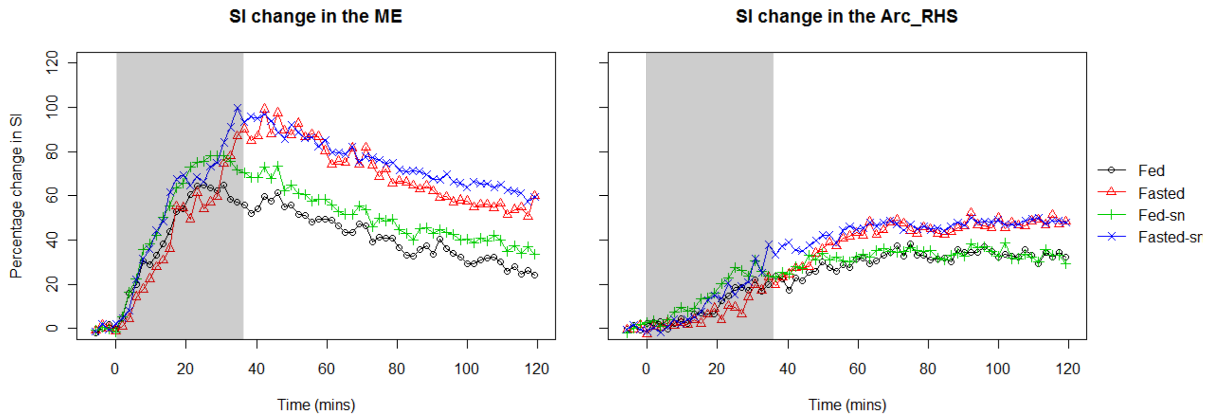

Figure 3.6: timecourses of mean group signal change measured manually (Fed, Fasted) or automatically on spatially normalised images (Fed-sn, Fasted-sn) in the ME and Arc_RHS in fed (n=4) and fasted (n=5) groups of mice subjected to sems MEMRI. The grey areas indicate the period of the $MnCl_2$ infusion. Raw data from which timecourses were derived kindly provided by Yu-Ting Kuo.

	ME (inc OBBB covariate)	Arc_RHS (inc IBBB covariate)
fed vs. fed-sn	0.3557	0.3637
fasted vs. fasted-sn	0.8036	0.3642
fed vs. fasted	0.0683	0.2605
fed-sn vs. fasted-sn	0.0404	0.2942

Table 3.1: p-values for various comparisons of data presented in Figure 3.6, calculated using linear mixed-effects modelling, with the covariates generated by the tensor ICA analysis in Figure 3.4, and the mouse experimented on as a random effect.

of the image is fuzzy since it is not registered. However, the brain outline and internal structure are very sharp, hence it appears the spatial normalization was able to accurately overlay brain images.

As examples of the effect of spatial normalization on timecourse extraction focus has been placed on the ME and Arc_RHS, which represent OBBB and IBBB regions respectively. Mean timecourses from a sems dynamic MEMRI experiment on groups of fed and fasted mice are presented in Figure 3.6. Visually it appears that the data from ROIs in spatially normalised images is very similar to that from manually drawn ROIs. This similarity is confirmed by the results of statistical tests presented in Table Table 3.1. The fasted vs. fasted-sn and fed vs. fed-sn comparisons test manual signal measurement against automated, and in both cases they are very similar, with neither comparison revealing significant differences ($p<0.05$). Similar analyses were undertaken at other ROIs, and all produced similar results, with the measurements from spatially normalised data being very similar to that from manually placed ROIs. This indicates that the spatial normalization procedure functions well- otherwise with such small sample sizes as we have here the results would be very different between manual and automated data, adding to the evidence in Figure 3.5 that the registrations are of good quality.

Looking at the fed-fasted results, the spatial normalization has produced a significant difference in signal change in the ME which did not occur when the ROIs were placed manually. The ME ROI here is spatially the equivalent of the ROI named Ärcüsed in Kuo et al. (2006) from where this data is derived. This region is renamed in this thesis to M̈Eäs anatomically it is the median eminence, not the arcuate nucleus (Paxinos and Franklin, 2004). In Kuo et al. (2006), the combination of those authors' manual ROI placements and the different statistical modelling method of generalised estimating equations (GEE) also found no significant difference in signal change between fed and fasted groups in the ME (p=0.22), agreeing with the non-significance found here using manual ROI placement. This implies that the spatial normalisation procedure has uncovered a significant difference in signal change between fed and fasted groups that would not otherwise have been observed. However, given that the fed-sn vs. fasted-sn result p-value of 0.0404 is only just under the arbitrary significance level of p=0.05, and that the experiment was based on small sample sizes of n=4 vs. n=5, this is too strong a conclusion to make.

A major aim of spatial normalization is to enable the generation of voxel-level activity maps rather than to merely aid ROI-based analyses by making them more automated and objective. The combination of a good Mn uptake model generated in the previous section, and a working spatial normalization used here allows this to be done. The results of such an analysis are presented on the sems fed/fasted data in Figure 3.7. Three models of signal change are presented. The first is simply a pre vs. post model of signal change. Here, most of the timepoints are discarded. The Mn uptake is assessed by what amounts to a voxel-voxel t-test between the baseline and last 15 images. The choice of baseline period is fixed by the point at which the Mn infusion starts. The period to compare it against is more arbitrary, and is a compromise between the greater accuracy of using more images, and reduced sensitivity due to the lower average Mn intake the further back it extends. The period of 15 images was chosen previously as it was thought this represented some kind of 'steady-state' period (Kuo et al.,

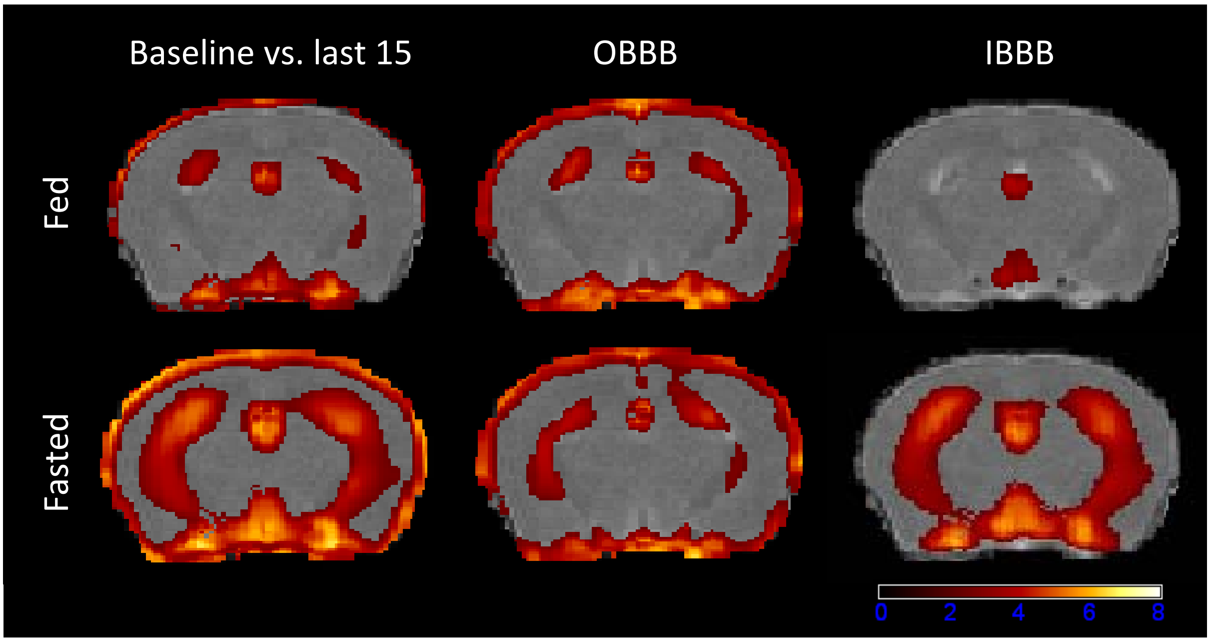

Figure 3.7: statistical maps of a slice through the hypothalamus showing Mn uptake in fed (n=4) and fasted (n=5) groups of mice during sems MEMRI. The colours are z-scores of Mn infusion-induced signal change (thresholded at Z>2.3) corresponding to the scalebar. Uptake was determined using either a simple baseline vs. last 15 model of signal change, or using the OBBB and IBBB models generated in Figure 3.4. Raw data kindly provided by Yu-Ting Kuo.

2006). The other two models are the OBBB and IBBB profiles derived in the previous section and shown in Figure 3.4.

The uptake maps for both fed and fasted groups of mice are presented. For the baseline vs. last 15 model, differences in uptake can be seen at the brain edge, in the lateral ventricles, circle of Willis and in the hypothalamus surrounding the 3rd ventricle. For the OBBB model, very little difference can be seen. The IBBB model produced similar results to the baseline vs. last 15, but without any uptake at the brain edge. Also the increased uptake proximal to the dorsal 3rd ventricle in the fasted group is more prominent. Voxel-voxel t-tests were carried out between the fed/fasted uptake maps generated using each model, but in all three cases these failed to identify clusters of significant differences.

3.4 Discussion

The work presented in this chapter was aimed at bringing analysis of infusion MEMRI data into the framework of data analysis used in human fMRI since the early 1990s (Fox et al., 1988; Friston et al., 1991, 1995a,b) and presented in Figure 3.1- that is, spatial normalization of all images followed by mass univariate (voxel-voxel) GLM statistics. This has the advantage of removing the subjectivity and laboriousness of manual ROI placement, while also allowing a whole brain analysis. In addition, the use of standard space templates allows anatomical locations to be compared across studies from different laboratories.

T_1-weighted MEMRI images have low within-brain contrast, brain/scalp separation and high contribution of non-rigid non-brain tissue. This makes it very difficult to objectively judge or describe with a summary metric the quality of the brain-weighted registrations used for spatial normalization. There are however two other admittedly poorer but still useful methods. The first is creating a mean image of all the spatially normalised data from a study (i.e. mean of all timepoints from all timecourses). Such images are presented for sems MEMRI data in Figure 3.5. As expected, much of the tissue outside of the brain is fuzzy, since this tissue was not included in the motion correction weights or the registration. However, the brain itself is sharp, especially the brain/scalp boundary. The Mn enhancement shows a symmetrical pattern and the ventricles are clearly visible. This indicates the spatial normalization is accurate. An additional source of evidence is that the timecourses measured using manual ROI analysis are similar to those measured automatically using template-derived ROIs on spatially normalised images (Figure 3.6). This demonstrates that the registration software is able to colocate accurately even tiny regions from different timepoints and different mice. That this occurs with only a 9-parameter registration is due to the great homogeneity of inbred rodent strains. Linear transformation is certainly not adequate for human brains (Ashburner et al., 1999; Heckemann et al., 2006; Klein et al., 2009; Steinmetz et al., 1990). Rodent brains are much more homogenous; however, even within strains for the same age group there are significant non-linear deformations up to hundreds of microns, including in the hypothalamus (Chen et al., 2006; Kovacevi et al., 2005). Thus although the spatial normalization procedure appears accurate, subtle registration errors caused by non-linear deformation could substantially degrade normalization quality, reducing the chances of observing signal changes in group data.

It should be noted that an alternative or complimentary strategy to software spatial normalization would be to use a stereotaxic frame with both tooth and ear bars to firmly fix the mouse head in position. This would both minimise motion to the extent that motion correction software would not be so crucial, and potentially also allow accurate image piloting to minimise even the amount of position correction required. However, such equipment was not available to software correction methods had to be used on the acquired images.

The ability to spatially normalise images is a substantial achievement, regardless of which sort of statistical analysis is used afterwards to analyse the signals. A first minor advantage is related to dealing with partial voxel movements. Especially during motion correction, structures can move fractions of a voxel in distance. Image registration software deals with this by interpolating the signal intensity between the voxels concerned. Most software for ROI measurement cannot do the equivalent for an ROI- i.e. move it fractions of a voxel and then only have that fraction's signal contribute to the overall ROI signal measurement. Hence the ROI has to be shifted only when it is judged that the structure has moved more than half a voxel. This can lead to inaccurate measurements, especially with small structures close to large signal boundaries, such as those involved in appetite sensing in the hypothalamus.

The main purpose of spatial normalization of images is that it enables independence from manually drawn ROIs- entities that effectively restrict one's ability to extract useful information from whole brain datasets. They also bias potential discoveries to whichever ROIs are chosen. An alternative would be to draw every possible ROI on every mouse, but this assumes it is known what ROIs are worth drawing and is also extremely laborious. ROIs still have an important role- many scientific hypotheses about changes in brain activity refer to specific regions and nuclei, and it is useful to be able to extract ROI data to view in detail the effect that specific stimuli have on those regions. In this way ROI analysis is complementary to that of voxel-voxel. In this case spatial normalization helps too- rather than having to custom draw an ROI for each fMRI session, the ROI only has to be drawn once for the whole experiment. An even better alternative is to take advantage of the fact that many brain templates such as the one used here (Dorr et al., 2008) come with carefully segmented brain atlases. In this situation, the ROI has already been drawn, saving the investigator time, and allowing standardisation of ROI definitions across different laboratories. One context in which manually-drawn ROIs would still be necessary is in the case of gross anatomical distortion. In this case automated spatial normalization, both in the direction of warping brains to a standard or warping atlases to the individual, would become unreliable.

This alludes to one of the biggest advantages of all- time saving. The sems fed/fasted data reanalysed here came from a broader study of hormone action involving 23 mice. There are potentially around 13 ROIs that one would want to measure in an appetite study. To carefully draw these manually on each of 23 mice takes a very long time, upwards of 1-2 hours per mouse. Shifting them to account for motion can extend this requirement even further. Thus placing ROIs manually for a 23 mouse study can take several days. This should ideally be repeated at least once by the same investigator a month later to freshly check for mistakes made the first time ROIs were drawn. To ensure the greatest objectivity, a separate investigator has to carry out the same procedure, so to complete manual ROI drawing on a single mouse takes a total of one day's worth of work. Thus a 23 mouse study can occupy a month of time simply drawing ROIs. The spatial normalization described here takes only a minute to set up per mouse- specifying data location and the brain centre co-ordinates. Once this has been done, the processing itself takes about 10-20 mins per mouse. This is of course computer time, so in practice spatially normalising 23 mice takes only 30mins to set up and can be left for the computer to process overnight, or while doing something else. This is a great time saving, and compels the use of spatial normalization wherever possible. Additionally, it frees data from the potential mistakes or biases of the investigators who draw the ROIs.

Once spatially normalised, for mass univariate GLM signal analysis we need a model of signal change. Based on previous data there were likely to have been two models needed- one for Mn uptake outside, and another for inside the BBB. Ironically, the best way to find such a model is EDA, a multivariate methodology. The one used here, tensor ICA as implemented in the FSL tool MELODIC (Beckmann and Smith, 2005), was readily able to find them. A note of caution is required however. The underlying cause of the signal changes in an infusion MEMRI experiment, and to some extent the images themselves, demonstrate that it is a great simplification to use a single simple model for assessing Mn uptake. Mn does not spread into the brain evenly- it is initially biased to regions near the ventricles, from where it spreads to gradually occupy the whole brain (Aoki et al., 2004). The relative importance of the various different circumventricular organs to the transport of Mn across the brain-CSF barrier (on top of any entry across the BBB) is unknown. Depending upon their location relative to the ventricles, each brain region will experience different rates of Mn influx and efflux, the absolute magnitudes and ratios of which will be shifting over time depending upon the timing and duration of the Mn infusion. This would explain why the unconstrained tensor ICA analysis produced six components rather than just the two predicted- there probably genuinely are more than two Mn uptake profiles. In fact, there should be one for every bilateral pair of voxels. Accounting for this situation would require the building of a complex model of Mn influx and efflux at each voxel in the brain and how these interact with the nature of the Mn infusion. This model could then be used to assess and create more accurate statistical maps of Mn uptake in each mouse (which are later fed into a group analysis) that currently are instead created here using FEAT.

The model derived from tensor ICA also has the disadvantage in the context of acute stimuli that its shape remains invariant. Hence it is assumed that the acute stimulus evenly affects Mn uptake across the entire post-baseline period. Such a situation is unlikely to be true.

A final issue is how these two tools, spatial normalization and a Mn uptake model, alter inference in a basic appetite experiment. The most basic, and that which was used here, is the stimulus of fasting. The data in Figure 3.6 and Table Table 3.1 at least indicate that they do not destroy observations which were made previously about the effect of fasting on Mn uptake in the ME. However, the fed/fasted results are puzzling. Yet again, as with experiments presented in Chapter 2, fasting has stimulated Mn uptake changes in unexpected areas, and not the ventral hypothalamus. The primary site seems to be the lateral ventricles, and ventricular and circumventricular regions in general. Although t-tests could not uncover statistically significant differences between the two groups regardless of which Mn uptake model was used, this is likely to be more down to the high variability of Mn uptake and the stringent sample size requirements of a mass univariate experiment rather than because differences between the two groups do not exist.

The uncovering of these puzzling differences is a good showcase for the principle of using mass univariate statistics on spatially normalised data, as opposed to using manual

ROI placement: interesting phenomena have been observed that would otherwise have gone unnoticed. The more contentious issue is whether the Mn uptake models derived from tensor ICA are useful. It is difficult to tell here, but it is very likely to be the case since they can use information from every single timepoint to be fitted- in the sems MEMRI case 66 points rather than the 18 used for the baseline vs. last 15 analysis. Using more data should allow a more accurate fitting. This is of course only as long as the Mn uptake profiles are similar across mice- any shape changes would compromise the goodness of fit.

Chapter 4

Haemodynamic fMRI

4.1 Introduction

The majority of work presented in this thesis relates to using MEMRI to assess brain function. This method uses the exogenous contrast agent Manganese (usually as $MnCl_2$)- a paramagnetic agent that increases the MR signal and which is also taken up preferentially by active neurons (Silva et al., 2004)- as a marker of neuronal activity. Although this method is considered by some to be more direct, easier to use and less physiologically perturbed than haemodynamic methods (Van der Linden et al., 2007), it suffers from toxicity problems that both compromise physiological relevance and prevent translation into humans. In addition, the tendency of Mn to accumulate in tissue and disperse slowly makes it relatively difficult to observe rapid temporal changes as opposed to cumulative changes over time. Hence despite their numerous flaws it is worth considering using haemodynamic methods. These are well established at observing brain function in rodents. Some of the earliest experiments using MRI to study blood flow in the brain were conducted in rats, and have a much longer history than MEMRI (Ogawa et al., 1993a,b; Rudin and Sauter, 1991). Since then, haemodynamic responses have been recorded in response to an extensive range of stimuli including somatosensory and pharmacological interventions (Van der Linden et al., 2007).

One exception to this is appetite related responses. Almost no literature exists on haemodynamic responses of any sort to any kind of appetite related intervention, whether fasting, diet, genetic modification or hormone injection. The first three are pre-scan chronic interventions. These are particularly difficult to study using haemodynamic methods since they induce gross changes in circulation, usually by changing body composition and physiology in such a way as to undermine the assumptions of the models that translate MR images from CBV/CBF experiments into measures of blood flow and volume (Østergaard, 2005). The one technique that could circumvent this is ASL, which is in principle immune to the problem of contrast agent dosing for CBV/CBF measurement, as well as the temporal drift which affects any sequence primarily weighted towards detection of the BOLD effect (Aguirre et al., 2002). Unfortunately ASL is not very sensitive, and is also difficult to set up, especially so for whole brain acquisitions, so it was not used here.

The most fruitful route in haemodynamic studies is to apply within-scan acute intervention on animals with similar starting physiologies and body compositions. Giving the intervention within the scan enables normalization to conditions on the day, whatever these might be. Chronic treatments can also now be studied albeit indirectly via their modulatory effect on the acute intervention. The aim of this series of experiments was to see if such methods were viable in the context of appetite studies.

Since ASL could not be used to measure CBF, these studies concentrated on using simpler sequences to measure BOLD and CBV instead. Both have been used extensively to assess the effect of acute pharmacological stimuli (Martin and Sibson, 2008; Shah and Marsden, 2004; Steward et al., 2005). For reasons explained earlier, they cannot be used to look directly at the effects of fasting, diet or genetics, though they could be used indirectly by observing the effects of those three stimuli on responses to an acute stimulus.

The hormonal stimuli chosen were ghrelin and exendin-4. Ghrelin is an endogenous orexigenic hormone secreted peripherally mainly by the stomach (Kojima et al., 1999; Tschöp et al., 2000). It acts via the arcuate nucleus (Kojima and Kangawa, 2005) and has previously been shown to affect the signal in MEMRI experiments (Kuo et al., 2007). Exendin-4 is a mimetic of the endogenous anorexigenic hormone GLP-1, but is far more potent (Young et al., 1999) due to its resistance to proteolytic degradation (Parkes et al., 2001). It also acts via the arcuate nucleus (Ma et al., 2007). Hence these two hormones are both relatively strong and reliable pharmacological appetite-related stimuli, that should both alter the haemodynamic MR signal in the arcuate nucleus.

4.2 Materials and Methods

4.2.1 Hormones

Ghrelin (Bachem cat# H-4864) was dissolved in sterile ddH_2O before aliquotting into vials with 9nmol (30μg) each. These were freeze-dried and stored at -20°C before reconstitution in 200μl water at the moment of use. Exendin-4 (Phoenix Peptide cat# 070-94) was dissolved in sterile ddH_2O and aliquotted into 250μl volumes of 0.215nmol (0.9μg) each. These were stored at -80°C and thawed to room temperature at the moment of use.

4.2.2 BOLD-Weighted Acquisitions

Equipment, animal handling and preparation were similar to those described in Sections 2.2.1 to 2.2.3 and 2.2.6 on pages 56 to 58 respectively. The main modification was maintenance of isoflurane anaesthesia in a 7:3 N_2O:O_2 mix (0.7:0.3L min^{-1} respectively) rather than pure O_2, with the concentration varied throughout between 1-1.5% to maintain a breathing rate of approximately 130bpm. In addition an i.p. cannula was implanted during animal preparation. The reason for the anaesthesia change was that although supplemental oxygen is beneficial to animals undergoing anaesthesia (Flecknell, 1996), pure O_2 can raise the partial pressure of oxygen (pO_2) in blood to 400mmHg, much higher than the normal physiological range of 100-200mmHg. At 400mmHg there is little deoxyhaemoglobin left, and hence no BOLD effect. A much smaller supplementation level of 30-40% O_2 with either air, nitrogen or (least ideally, since it is an anaesthetic and vasodilator) N_2O making up the remainder of the gas supply avoids saturating the blood with oxygen. N_2O was used here for the remainder as at the time it was the only one for which delivery equipment was available, was recommended as being an adequate substitute (W. Gsell, *pers comm*) and it has been used successfully elsewhere (Duong et al., 2000a).

Images were acquired at 9.4T using a Varian Unity INOVA console running VnmrJ 1.1D software and a 40mm long 30mm i.d. quadrature birdcage transmit-receive RF coil. Whole head shimming was performed manually. An fsems sequence was used with the following parameters: *TR*=4834ms, inter-echo spacing=5.6ms, echo train length=8, k-space centre=7, matrix=192$\times$96, FOV=38.4$\times$19.2mm, 2 averages, 42 coronal interleaved overlapped Gaussian profile slices of 0.4mm thickness, gap -0.2mm (negative due to overlap; voxel size 200μm isotropic) acquired in 1m 56s, 124 volumes acquired giving a total session time of four hours. The use of overlapped Gaussian profile slices halves the effective *TR* and leads to a degree of through plane blurring, though it provides a slice width of 200μm that would otherwise not be possible (Noll et al., 1997). Image reconstruction and conversion to NIfTI-1 format (Cox et al., 2004) was carried out using custom written code in MATLAB (The Mathworks, Natick, MA, USA).

Injections (saline n=6, ghrelin n=6, exendin-4 n=4) were made i.p. 20mins after the start of the scan during the 11th acquisition, at a dose of 7μl g^{-1} (0.3nmol or 1μg g^{-1} and 6pmol or 25ng g^{-1} for ghrelin and exendin-4 respectively). This ghrelin dose is able to induce adiposity and weight gain when injected daily (Tschöp et al., 2000), as well as hypothalamic MEMRI signal increases (Kuo et al., 2007). Exendin-4 has not been used in fMRI experiments before, but the dose used here was enough to induce substantial weight losses and reduction in food intake in mice and rats (Mack et al., 2006).

4.2.3 CBV-Weighted Acquisitions

Equipment, animal handling and preparation were similar to those described in Sections 2.2.1 to 2.2.3 and 2.2.6 on pages 56 to 58 respectively, the main modification being that isoflurane anaesthesia was maintained using 5:1 medical air:O_2 (33% O_2 in air; 1:0.2 L min^{-1} respectively). This anaesthesia regime was used as it exactly (Mandeville et al., 2004) or closely (Liu et al., 2007; Mandeville et al., 2007; Marota et al., 2000) matches that used in other successful CBV/IRON experiments. Images were acquired at 9.4T using a Varian DirectDrive console running VnmrJ 2.2C software and a 40mm long 30mm i.d. quadrature birdcage transmit-receive RF coil. Shimming was performed using FASTMAP (Gruetter, 1993; Gruetter and Tkac, 2000) on a 4×4×4 mm voxel placed at the centre of the brain (special thanks to Vladimir Mlynarnik for providing code and installation advice, and Marzena Wylezinska-Arridge for installation and setup). Linewidth was measured using PRESS and ranged from 25-50Hz. A gems sequence was used with the following parameters: TR=390ms, TE=5ms, matrix=128×128, FOV=19.2×19.2mm, 2 averages, 50 interleaved transverse slices of 0.2mm thickness (voxel size 150×150×200m) acquired in 1m 40s, 72 volumes acquired giving a total session time of 2 hours. Images were converted from VnmrJ FDF to NIfTI-1 format (Cox et al., 2004) using ImageJ (Rasband, 1997-2008).

Endorem (Guerbet) supplied at 11.2mg ml^{-1} was diluted 2-fold in sterile ddH$_2$O to 5.6μg l^{-1}. After 10 pre-contrast baseline acquisitions, at the beginning of the 11th acquisition the diluted endorem was injected i.v. at a dose of 4.1μl g^{-1} (23μg g^{-1}). The endorem was allowed to equilibrate for 5 acquisitions, after which 15 post-contrast baseline images were acquired. After these 30 acquisitions, any intervention was given at the beginning of the 31st acquisition.

For the N_2O challenge experiment (n=3), anaesthesia was changed to 2:1 N_2O:O_2 (0.8:0.4L min^{-1}) at the beginning of the 31st acquisition for the rest of the scan. For ghrelin experiment, during animal preparation an i.p. cannula was implanted. Saline (n=3) or ghrelin (n=3) injections were made i.p. at the beginning of the 31st acquisition, at a dose of 7μl g^{-1} (0.3nmol or 1μg g^{-1} ghrelin dose).

4.2.4 Image Analysis

NIfTI-1 format images (Cox et al., 2004) were spatially normalised according to the scheme described in section Section 3.2.1 on page 87. Briefly, images were motion corrected using SPM5 and normalised using a combination of tools from FSL and AFNI to a standard mouse brain template (Dorr et al., 2008). ROI analyses and timecourse extractions were carried out using MRIcron (Rorden et al., 2007). The striatal ROI was extracted from the atlas supplied with the mouse brain template (the atlas is composed of 62 structures drawn manually on the template, which itself is a composite of 40 normalised C57BL/6 mouse brain images). The Arc_LHS was drawn based upon comparisons with a standard mouse brain atlas (Paxinos and Franklin, 2004). Timecourses were plotted using Microsoft Excel 2007.

4.3 Results

4.3.1 BOLD Timecourses Exhibit Substantial Drift, are Noisy and Show No Response to Ghrelin or Exendin-4 Injections

The BOLD effect offers a promising method for visualising (albeit indirectly) the effect of various stimuli on neuronal activity in the brain. It is widely used in humans, so results can readily be compared to those from human fMRI. In addition, it does not require the administration of any exogenous agent. To test its efficacy in responding to hormones controlling energy balance, it was decided to acquire BOLD timecourses and observe their response to the administration of two potent hormones involved in energy balance- ghrelin, and exendin-4. Both act on the arcuate nucleus, but with opposite effects- ghrelin increases food intake (Tschöp et al., 2000) while exendin-4 reduces it (Mack et al., 2006). In addition, ghrelin has a half-life of minutes (Kojima and Kangawa, 2005) compared to hours for exendin-4 (Parkes et al., 2001). Both were injected i.p. at concentrations known to induce a response- 0.3nmol g^{-1} for ghrelin (Kuo et al., 2007) and 6pmol g^{-1} for exendin-4 (Mack et al., 2006). Figure 4.1 shows a typical single timepoint BOLD image acquired using the protocol here.

Since there was no precedent for what the signal change should be in response to hormones related to energy balance, the initial analysis was ROI-based, rather than the voxel-voxel GLM approach advocated in Chapter 3. The targetted ROI was the left arcuate nucleus (Arc_LHS), whose activity is modulated by both hormones. Its location is indicated in Figure 4.1.

Arc_LHS BOLD timecourses for saline (n=6), ghrelin (n=6) and exendin-4 (n=4) injected groups of mice are shown in Figure 4.2. All three timecourses exhibited a substantial amount of downward signal drift. The saline group signal declined by around 4% shortly after 2 hours of imaging, rising back up to a decline of around 2% by the 4 hour end point. The ghrelin group had similar behaviour up until just after 2 hours, when it diverged, levelling off before a further decline, finishing around 5% lower than at the start. The exendin-4 group diverged from the saline and ghrelin groups at around 45mins after the commencement of the scan, with signal spiking back up to baseline levels and remaining steady up until 1h 48m. At this point signal

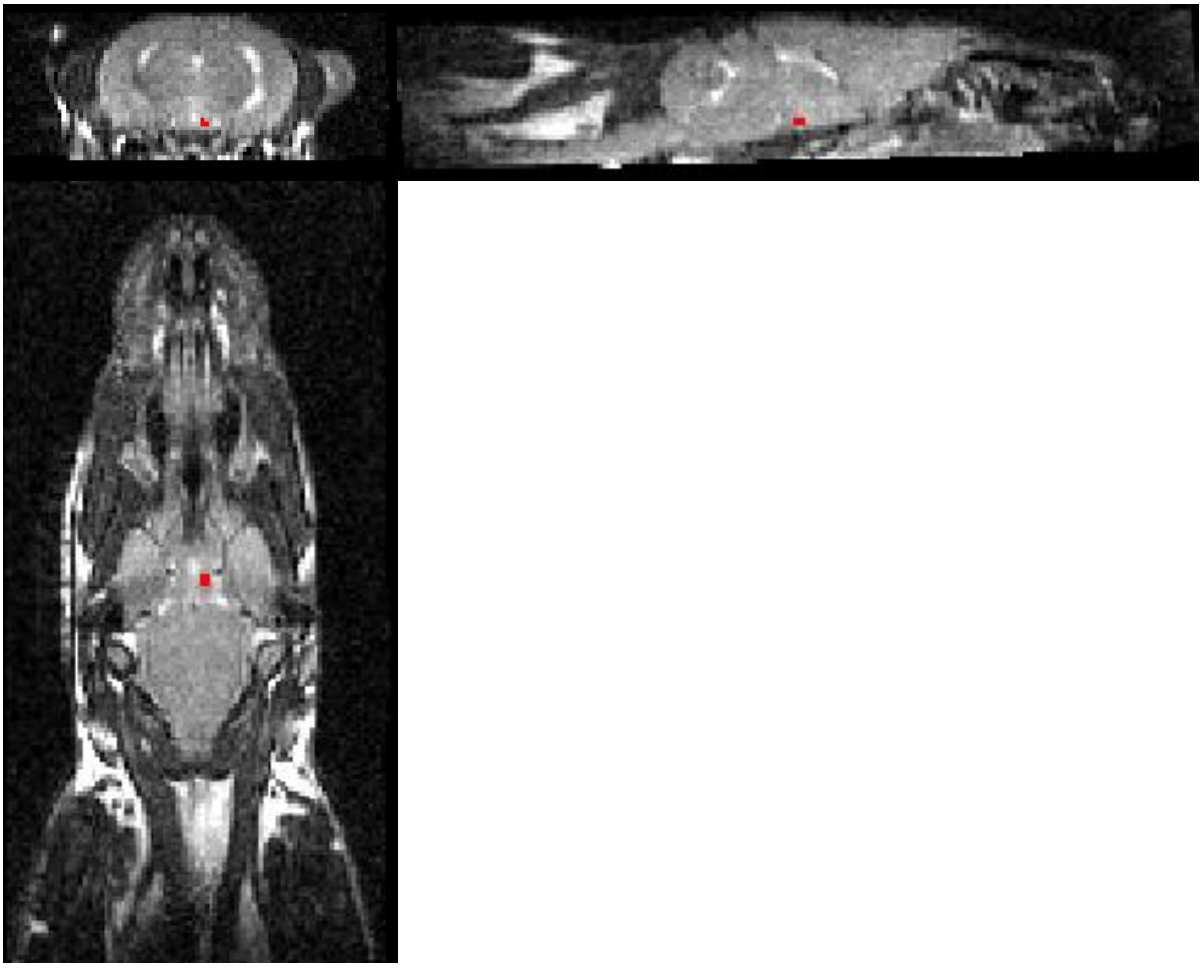

Figure 4.1: example single timepoint BOLD image with location of Arc_LHS ROI shown in red. Clockwise from left, transverse, coronal/axial and sagittal planes are shown. This image has been motion corrected and normalised, hence some areas towards the extremities may be filled with black due to reslicing of regions that were outside of the acquired FOV.

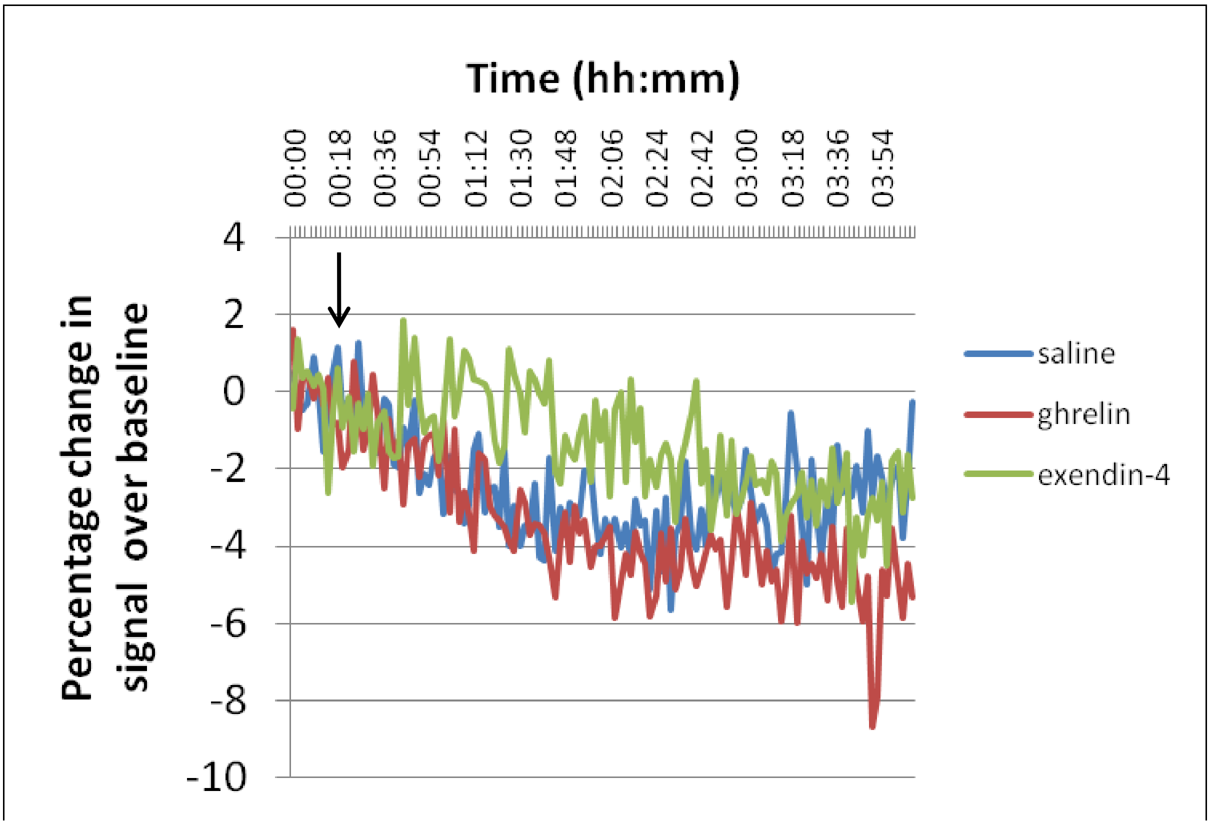

Figure 4.2: BOLD signal changes in the Arc_LHS of the mouse brain in response to saline (n=6), ghrelin (n=6) or exendin-4 (n=4) i.p. injections. The arrow indicates the timepoint of injection (20 mins into the timecourse during the 11th acquisition). The baseline is defined as the mean of the first 10 (pre-injection) acquisitions.

plummets to slightly less than 2% below baseline, before continuing a slow steady decline down to slightly more than 2% below baseline.

4.3.2 N_2O Challenge Does Not Affect CBV-Weighted Signal

The poor performance of the BOLD method was not entirely unexpected since BOLD is known not to have much statistical power beyond a stimulus cycle time of 1min (Aguirre et al., 2002). However, the substantial amounts of signal drift and noise were a surprise.

To deal with this, an alternative haemodynamic method was tried. This was cerebral blood volume weighted (CBV) MRI. Here, a blood pool contrast agent, usually iron oxide based, such as SPIOs and USPIOs (Weissleder et al., 1990) is used to weight the MR signal to blood volume. Although involving the administration of an exogenous agent, it has proven to be much more sensitive than BOLD, and because it involves much larger signal changes, less prone to background drift. This method has also been dubbed IRON, for increased relation with iron oxide nanoparticles (Chen et al., 2001; Jenkins et al., 1993).

An initial test of whether a CBV protocol is working well enough to detect a pharmacological stimulus is to see the effect of nitrous oxide on the CBV signal (Mandeville et al., 2007). N_2O is a potent vasodilator that readily crosses the BBB, producing large increases in both CBF and CBV (Lorenz et al., 2002). Hence in a CBV-weighted experiment there should be a large drop in signal upon N_2O administration (Lorenz et al., 2002; Mandeville et al., 2007).

Three mice were subjected to CBV, with nitrous oxide administered approximately half-way though the scan. The effect of CBV was measured in the striatum, where a previous study had shown its effects should be quite potent. The location of the striatal ROI is shown in Figure 4.3. A timecourse of CBV images acquired with the protocol used here is shown in Figure 4.4. Upon endorem administration in timepoint 11, there is an expected large global drop in signal. The drop is not even, with the greatest drops unsurprisingly occurring at the location of large vessels, such as the circle of Willis. The agent gradually washes out, leading to increasing signal as the experiment continues.

N_2O is an example of an agent where the relationship between haemodynamics and neuronal activity is decoupled- N_2O is an anaesthetic, producing reductions in neuronal activity. This is

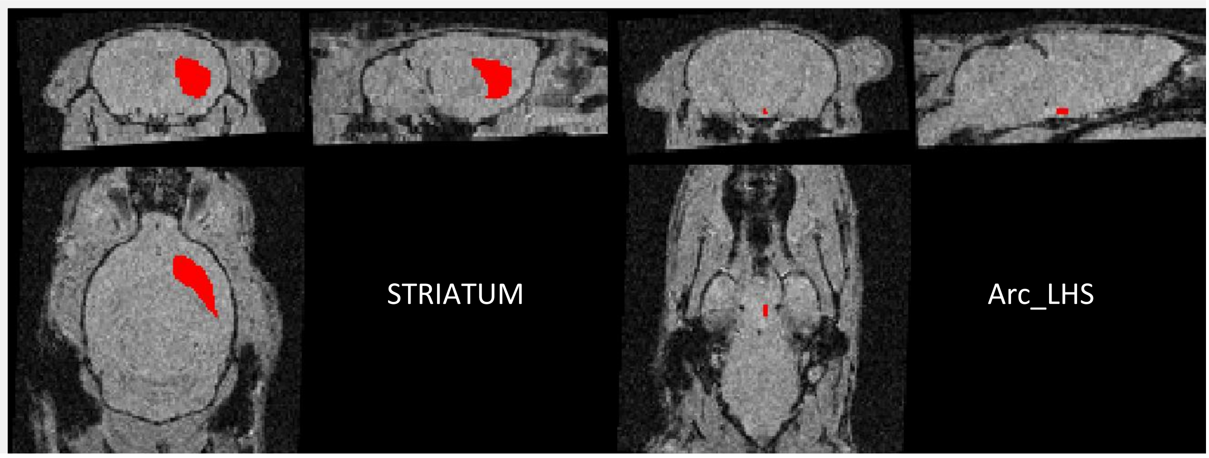

Figure 4.3: location of ROIs (marked in red) used during CBV studies, overlaid onto a pre-injection image.

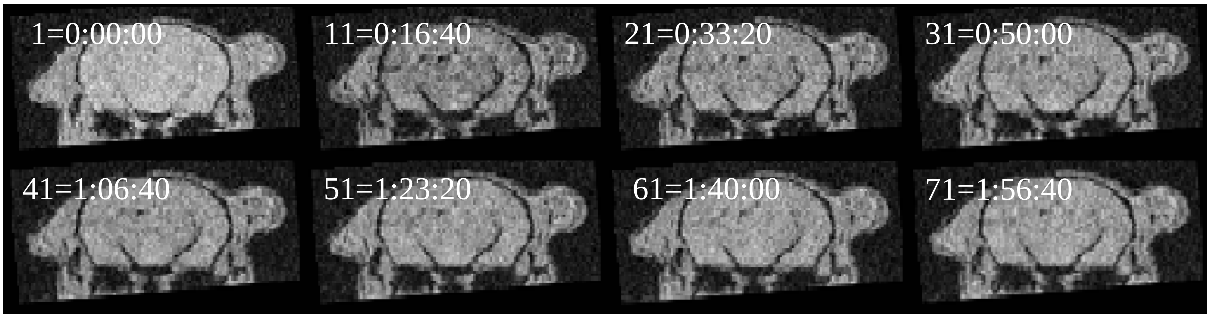

Figure 4.4: timecourse of images at a slice through the hypothalamus during a CBV experiment. Numbers indicate timepoint and time in h:mm:ss. Contrast agent injection is made at the beginning of timepoint 11. The images have been motion corrected and normalised, hence some areas towards the extremities may be filled with black due to reslicing of regions that were outside of the acquired FOV.

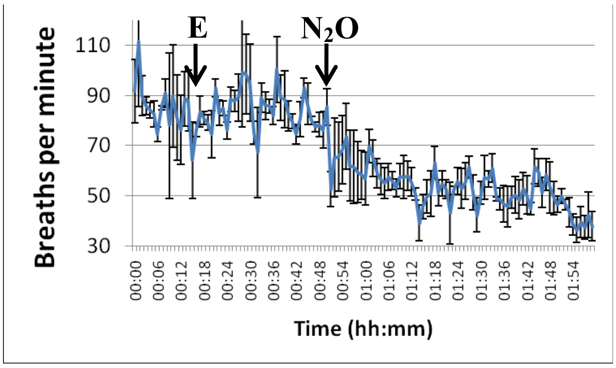

Figure 4.5: change in breathing rate during a CBV experiment with N_2O challenge (n=3). Error bars are of SEM. Arrows indicate administration times. E=endorem.

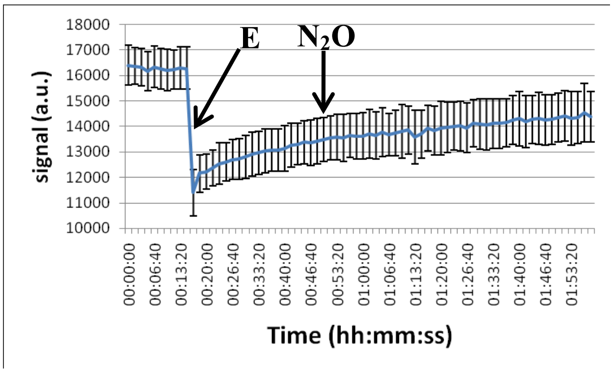

Figure 4.6: change in signal in the striatum during a CBV experiment with N_2O challenge (n=3). Error bars are of SEM. Arrows indicate administration times. E=endorem.

despite the fact that it also causes increases in CBF and CBV (Lorenz et al., 2002)- which in haemodynamic fMRI are considered proxies of increased neuronal activity. One consequence of this anaesthetic action is that breathing rate drops substantially. Figure 4.5 demonstrates this physiological effect. Prior to N_2O administration, the breathing rate holds steady at around 85 bpm. As soon as N_2O is provided, it drops substantially to just above 50bpm, thus demonstrating that N_2O is being provided at a high enough concentration to produce profound physiological changes, and hence one would hope changes in CBV too.

Figure 4.6 shows CBV timecourses of signal in the striatum during this experiment. The effect of the endorem administration is clear, with a sharp drop in signal. However, very surprisingly the N_2O has no noticeable effect on the timecourse.

4.3.3 Ghrelin Injection Does Not Affect CBV-Weighted Signal

Nitrous oxide administration is a very unusual pharmacological intervention. Although it was disappointing that it was not able to detect any CBV changes in the striatum, it is possible that this is more a function of using this stimulus than the failure of the technique.

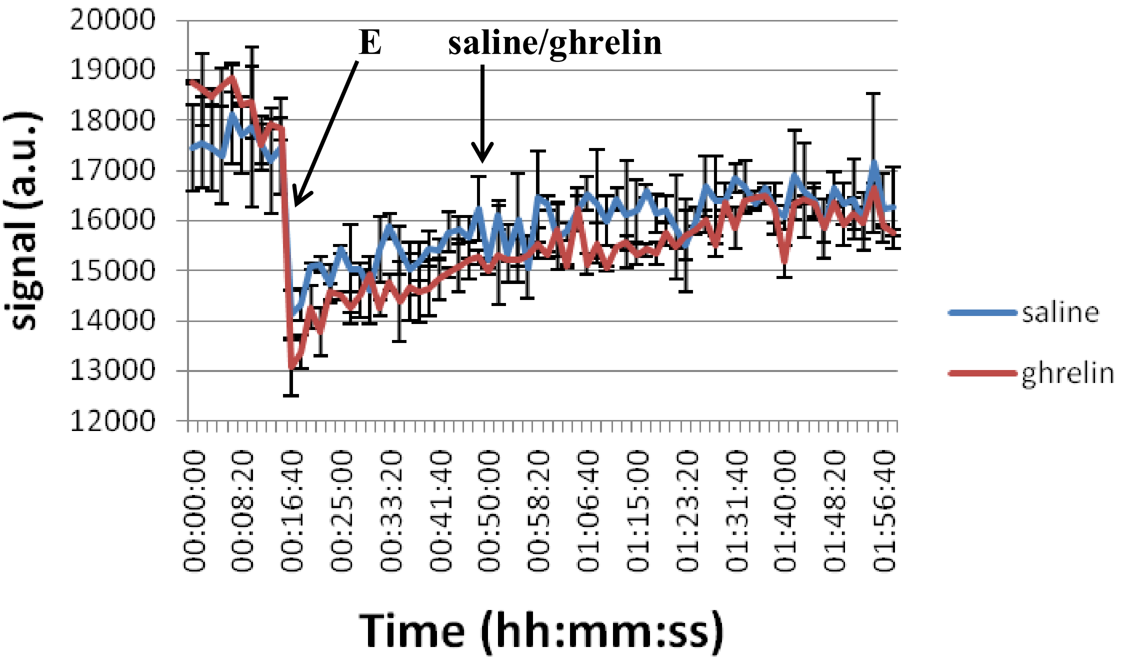

Figure 4.7: change in signal in the Arc_LHS during a CBV experiment with either saline or ghrelin administered i.p (n=3 per group). Error bars are of SEM. Arrows indicate injection times. E=endorem.

Hence despite the failure of the N_2O challenge, the effect of an i.p. ghrelin stimulus on CBV signal was tested, the results of which are shown in Figure 4.7 for an ROI covering the Arc_LHS (see Figure 4.3 for its location). The dose was that same as that used for the BOLD-fMRI study (0.3nmol g^{-1}). Unfortunately, as can be seen, ghrelin administration had no obvious effect on the CBV signal compared to one of saline. The timecourse was considerably less steady and noisier than that for the N_2O challenge experiment. This is probably a consequence of using the Arc_LHS ROI, which has a far smaller volume than that of the striatum.

4.4 Discussion

This series of studies aimed to use haemodynamic fMRI to observe responses to hormones involved in energy balance in rodents. Unlike MEMRI, haemodynamic methods have a definite potential for longitudinal use at frequent intervals since the toxic contrast agent $MnCl_2$ does not have to be administered.

4.4.1 Effects of Protocol Choices on Observing a BOLD Response

The first attempt involved observing the BOLD response to administration of the potent orexigenic hormone ghrelin and the anorexigenic hormone exendin-4. The BOLD effect is the simplest to observe in terms of both the MR acquisition, and also no exogenous contrast agent needs to be administered- the blood itself is the contrast agent. The protocol used here was unusual for rodent fMRI in four ways- it used mice rather than rats, spin rather than gradient-echoes, very high resolution (especially through-plane) and isoflurane anaesthesia rather than α-chloralose or urethane. Each of these could have inhibited the ability to see a change in BOLD signal, but can all be justified.

The first unusual aspect that requires justification is the choice of mice over rats. Rats are used in the vast majority of rodent fMRI studies- their larger size (but not so large as to be inconvenient) produces a greater MR signal and makes surgery for physiological monitoring, maintenance and substance administration more practically possible than in mice. Previously, there were only four published mouse BOLD fMRI studies, two of which involved hindpaw electrical somatosensory stimulation (Ahrens and Dubowitz, 2001; Nair and Duong, 2004), and the other two olfactory stimulation (Xu et al., 2003, 2005). Only three studies existed for CBV fMRI, the first a pharmacological proof of principle using bicuculline administration (Mueggler et al., 2001), then in the background of an Alzheimer's disease (AD) model (Mueggler et al., 2002) and one of hindpaw stimulation also in a background of an AD model (Mueggler et al., 2003), all from the same laboratory. There have also been two mouse CBV mapping studies (Moreno et al., 2006; Wu et al., 2003). The AD studies indicate a crucial motive to use mice despite the practical difficulties- there are far more mouse models of disease, especially genetic models, than for rats, and this includes the field of obesity and appetite (Speakman et al., 2008). Recently, mouse haemodynamic fMRI has been extended beyond simple blunt stimuli into more subtle pharmacological studies, specifically the effect of serotonergic (5-HTergic) agents on a mouse behavioural model of early life stress (Razoux et al., 2008), and a genetic one of a 5-HT$_{1A}$ receptor inactivation (Gozzi et al., 2008), although these were CBV-based studies rather than BOLD.

The second is the use of spin- rather than gradient-echoes. Spin-echo has in the past been primarily advocated for field strengths typical of clinical settings such as 1.5 and 3T, where GE BOLD is highly susceptible to draining vein and large vessel effects (Duyn et al., 1994; Frahm et al., 1994; Hoogenraad et al., 2001; Lai et al., 1993; Oja et al., 1999; Olman et al., 2007; Song et al., 1996). However, these effects continue to the higher field strengths typical of animal studies (Duong et al., 2003; Lee et al., 1999; Yacoub et al., 2005), hence despite the greater BOLD responses produced by gradient-echoes, spin-echoes were used here, an approach advocated elsewhere (Steward et al., 2005).

The part of the protocol with the least precedent is the use of such high spatial resolution. The in-plane resolution of 200μm is in the range of most previous studies; it is the through-plane resolution that was particularly high- most studies have not reduced slice thickness much below 1mm. This is mainly for reasons of SNR, since signal can drop off with reduced slice thickness with a rapidity that does not affect in-plane resolution. However, increased SNR achieved through lowered spatial resolution can be outweighed by the reduced CNR caused by increased partial volume artefacts. Dissecting pathways involved in appetite-related responses requires being able to resolve different hypothalamic nuclei. Their small size and irregular shape would make a slice thickness of 1mm very inefficient, since many of the voxels would now include non-parenchymal matter. Hence despite the lack of precedent and lowered SNR, there is a need to use high spatial resolution to enable the method to be scientifically useful.

The final unusual part of the protocol is the use of isoflurane anaesthesia rather than α-chloralose or urethane, which are commonly used anaesthetics for neurophysiological studies (Flecknell, 1996). This orthodoxy dates back to a 1992 study indicating that functional-metabolic coupling in the brain was better maintained under α-chloralose anaesthesia than with many other anaesthetics (Ueki et al., 1992). This situation is thought to be a consequence of α-chloralose inducing a lowered baseline state of brain activity (Hyder et al., 2002; Maandag et al., 2007), although it must be stressed these studies only used one functional model- electrical forepaw stimulation (Hyder et al., 1994). Also note that no similar work has been carried out with urethane. Unfortunately since α-chloralose causes acidosis and involuntary excitement and urethane is a potent carcinogen (Flecknell, 1996), neither can be used for longitudinal studies. This substantially limits scientific usefulness, and so other agents must be considered.

A promising candidate is the α_2-adrenoreceptor agonist medetomidine whose only downsides are substantial diuresis and interference with studies of adrenoreceptors (Weber et al., 2006). Unfortunately in our hands this anaesthetic was unable to maintain anaesthesia in mice or rats. Three C57BL/6 mice weighing around 25g each were tested with medetomidine, each over the course of 2 hours. The first was scanned under a similar protocol to Weber et al. (2006)- initial induction with isoflurane (not halothane since this is carcinogenic and not readily available), followed by a 100μg kg^{-1} hr^{-1} i.p. infusion (not s.c. since this is technically difficult in mice, and no bolus was given since i.p. administration has much faster kinetics than s.c.). The isoflurane was then turned off; however any attempt to reduce the concentration below 0.25-0.5% caused the mouse to wake up. Injection of 2-3 boli of 50μg kg^{-1} each followed by a 10-fold increase in the infusion rate to 1mg kg^{-1} hr^{-1} eventually prevented the mouse waking up, but it still had a pedal pinch reflex and hence was not fully anaesthetised. In a second mouse, after initial induction with isoflurane, a 200μg kg^{-1} bolus was followed up with a 400μg kg^{-1} hr^{-1} i.p. infusion (a four-fold increase over that use by Weber et al. (2006) and using the faster i.p. route rather than s.c.). 15 minutes after the start, it was possible to completely turn off the isoflurane without the mouse waking up. However, the mouse still displayed spontaneous blinking of the eyelids, and hence was not fully anaesthetised. A third mouse was tried with a similar protocol to the second, but further increasing the initial bolus and infusion doses to 250μg kg^{-1} and 500μg kg^{-1} hr^{-1} respectively. This mouse stayed still, but again was not fully anaesthetised after withdrawing isoflurane, with occasional twitching of the tail, hindleg and eyelids. In addition at all the doses used here there was substantial diuresis, with the mice losing 2-3g weight in fluid. It would not be surprising that mice require a different dose level to rats; what is surprising is that such large increases in dose failed to produce anaesthesia. These increases were also well above the recommended range in mice of 30-100μg kg^{-1} s.c. (Lukasik and Gillies, 2003) just for an induction bolus. Interestingly, an independent attempt to replicate the protocol of Weber et al. (2006) in three rats of similar weight and the same strain failed to produce anaesthesia (B. Alonso, *pers comm*). Based on these difficulties, determining the best dose range for medetomidine would have required large numbers of animals, and was not considered worthwhile given the primary purpose of this study was to observe haemodynamic responses to appetite-related stimuli.

Two other anaesthetics were also considered- firstly propofol, which has been used successfully in animal BOLD-fMRI experiments before using electrical forepaw (Kennan et al., 1998; Scanley et al., 1997) and hindpaw stimulation (Lahti et al., 1999). Unfortunately propofol is formulated in soy bean oil as it cannot dissolve easily in water (see Banaszczyk et al. (2002) and references therein); this gives it a nutritional load, and hence it is not suitable for experiments studying energy balance. The second anaesthetic tried was saffan, which has no history of use in fMRI. Unfortunately, in 3 C57BL/6 mice of around 25g each, at the recommended dose of 10-15mg kg^{-1} i.v. (Lukasik and Gillies, 2003), there was a substantial level of apnoea. Given these problems with using other anaesthetics, and that isoflurane and halothane have been used successfully in BOLD fMRI before (Austin et al., 2005; Masamoto et al., 2007), it was considered reasonable to use them here.

The two main problems in the BOLD experiment conducted here were signal noise and drift- therefore the limiting factors are imaging at high spatial resolution and using mice rather than the use of spin-echoes and isoflurane anaesthesia. Drift is thought to be caused by scanner instability rather than physiological changes (Smith et al., 1999). This is a difficult problem to solve. Noise levels could be reduced by using a higher SNR sequence such as EPI, but this would require compromises in spatial resolution due to hardware limitations. Given that the problems with BOLD appear intractable, it is best to use a method such as CBV-weighted MR whose signal changes are much larger than BOLD (Chen et al., 2001; Mandeville et al., 2004) and so should overwhelm drift and noise.

4.4.2 Factors Influencing Observation of a CBV Response

The failure of the CBV experiments to observe a response to either nitrous oxide or ghrelin was very surprising. There was so little response it was not considered worth converting the CBV timecourses to rCBV using the formula:

$$rCBV(t) = \frac{\ln(\frac{S(t)}{S_{POST}})}{\ln(\frac{S_{POST}}{S_{PRE}})}$$

(t=time, S(t) is signal at time t, S_{POST} is post-contrast baseline signal, and S_{PRE} is the pre-contrast baseline signal)
or detrending the timecourse (Schwarz et al., 2003).

As with BOLD, there were some unusual aspects to the CBV protocol used here that could have prevented any chance of observing CBV responses. Unlike BOLD there were only two rather than four, since the choice of MR sequence and anaesthesia were based on a recommended protocol that has been used successfully before (Mandeville et al., 2004, 2007). Imaging mice at high spatial resolution was justified earlier. So other areas need to be explored to explain why these experiments failed.

Low sample sizes were used on the assumption that CBV experiments would produce such large responses that even in individual animals they should be visible. However, there is substantial inter-individual variability in response even in experiments where physiological parameters such as breathing and heart rate are strictly controlled (Schwarz et al., 2007). Thus performing this experiment on more animals may be productive.

A more contentious point is the level of physiological monitoring that is worthwhile. The monitoring of blood pressure, gases and acidity requires the catheterization and blockage of major blood vessels, hence the experiment becomes terminal due to the blood supply to several tissues being cut off. This prevents longitudinal studies, and since cerebral blood pressure is well regulated over a large range of input pressure (Gozzi et al., 2007; Zaharchuk et al., 1999), at least monitoring this parameter is not essential to successfully observing a CBV response.

Experiments with appetite hormones usually require supporting evidence that the hormones used are active- i.e. can change feeding behaviour. No such studies were carried out here, though the ghrelin used was from a batch that had induced increased feeding in other studies.

Regardless of the ghrelin's quality, there is still the question of why the nitrous oxide stimulus did not produce a CBV response. One final possibility is poor contrast agent administration and washout. The doses used here are based on CBV-optimization data from rats (Lu et al., 2007; Mandeville et al., 2004). However, for reasons of availability the contrast agent used was not a USPIO but a SPIO. These have higher relaxivities than USPIOs but also a greater washout (Wang et al., 2001; Weissleder et al., 1990). Despite this, good contrast or CBV-weighting was still available at the point where nitrous oxide or ghrelin was administered. However, in successful mouse phMRI experiments that used SPIOs the doses used have been much higher than here, 3.75μl g^{-1} of undiluted Endorem in 22-26g mice (Gozzi et al., 2008) rather than the 4.1μl 2-fold diluted Endorem used here (2.05μl g^{-1} undiluted; 1.8-fold more) and 150μl undiluted Endorem in 25-40g mice (Razoux et al. (2008); 2.25-fold more). This implies that CBV experiments in mice require higher contrast agent doses than in rats; however another possible reason is that these two studies used spin-echoes which are less sensitive than gradient-echoes to SPIO contrast, and so need higher doses to produce the same contrast level. Against this is that the group which used the 3.75μl g^{-1} Endorem dose in mice uses 2.67μl g^{-1} for experiments in rats (Gozzi et al., 2007), similar to the 2.05μl g^{-1} dose used here in mice and doses recommended elsewhere, but for rats (Lu et al., 2007; Mandeville et al., 2004). Thus for CBV experiments in mice it may be necessary to use a higher contrast agent dose than used here.

4.4.3 Concluding Remarks

Although ghrelin and exendin-4 are considered potent agents in the field of energy balance, in the field of neuroscience as a whole they are not exceptional. Pharmacological MRI experiments often concentrate on agents that are involved in depression disorders, and produce large responses in either BOLD or CBV experiments (Martin and Sibson, 2008). A recent study using a ghrelin stimulus found only tentative responses in rats despite tight control of animal physiology (Gozzi et al., 2007). It may be that appetite hormones induce haemodynamic responses that are too weak to be observed with current protocols and technology. Seen in this context, it is not surprising that with the low sample sizes, noisy images and uncontrolled animal physiology experienced in these experiments, a BOLD or CBV response to either ghrelin or exendin-4 could not be observed.

The lack of response to nitrous oxide is puzzling, and no explanation can be offered as to why this happened.

Chapter 5

Overall Discussion and Future Work

5.1 Summary of Developments

This thesis had three primary aims. The first was to make any possible improvements to the MEMRI protocol and test their efficacy before implementation in dissecting the mechanisms of appetite control. The second was the adaptation and implementation of image processing techniques widely used in haemodynamic fMRI for the analysis of infusion MEMRI data. The third was to see if it was possible to observe a haemodynamic response to appetite modulating hormones.

The first aim was covered in Chapter 2, where a series of modifications- covering the MR acquisition, $MnCl_2$ infusion and an anaesthesia-free alternative- were explored. One of the tested acquisition methods, fsems, provided higher spatial resolution and Mn sensitivity than the previous sems protocol, with no compromise in temporal resolution. Another possible positive development was adjusting the dose of Mn to fat-free rather than whole body mass to account for mice with varied adiposity levels. Unfortunately appropriate mice (i.e. of the same strain but fed different diets) on which to test this method were not available. Due to time limitations it was not possible to implement any of these modifications in an experiment designed to investigate mechanisms of appetite control.

Chapter 3 covered the second aim, and was the most productive study. Spatial normalization and voxel-voxel statistics increased the speed and objectivity of MEMRI analysis to a great level not possible when using ROIs placed individually on datasets.

The third aim was covered in Chapter 4. Unfortunately neither BOLD-weighted or CBV-weighted fMRI were able to observe a response to potent appetite-modulating hormones.

5.2 Limitations of Methods and Techniques Used

One characteristic of many of the experiments performed here has been low samples size, typically with n<8. This was based on previous precedents, especially in appetite MEMRI, where typical sample sizes ranged from 4 to 6 (Chaudhri et al., 2006; Kuo et al., 2006, 2007; Parkinson et al., 2009; So et al., 2007). For normally-distributed biological data it is recommended to use sample sizes of n≥30 if possible (Crawley, 2005). This is logistically difficult for animal experiments, so a compromise has to be reached. Given the variability of responses observed in these experiments, especially for the infusion MEMRI data, e.g. the fed vs fasted comparisons in Figure 2.9 on page 74, it would have been wise to increase the number of animals used rather than terminate the experiment with a low sample size. The effect of sample size on fMRI statistics is not a well-explored area for animal fMRI in general, including MEMRI. Based on human BOLD-fMRI data, sample sizes of at least 20 are required to generate robust and reproducible responses (see Thirion et al. (2007) and references therein). A large volume of animal MEMRI data was already available in the research group, and indeed some of this was used to generate the MEMRI signal change models shown in Figure 3.4 on page 92, and a separate dataset to demonstrate the efficacy of the spatial normalization procedure (see Figure 3.6 on page 94. A potential use of these datasets would have been to simulate the interaction between sample size and MEMRI signal response magnitude on the output of statistical maps and ROI data. The results of such an analysis would have been invaluable for determining the sample sizes that could have been used in the MEMRI experiments conducted here, and should be used in the future.

Such datasets were not available for performing simulations of haemodynamic studies. However, there is a much larger literature on animal haemodynamic fMRI than on MEMRI. The Discussion of the Chapter 4 went into extensive detail about how the protocol choices made here affected the likelihood of observing a response to gut hormones. The overall conclusion was that it was not surprising that no responses were observed to the acute stimuli of ghrelin or exendin-4 injection given the combination of protocol choices made. This conclusion was based on results derived from the literature. An especially important point is the use of isoflurane as an anaesthetic. Although this enables recovery experiments, its few successful uses have often involved large increases in the magnitude of the stimuli used in order to generate the same response as that seen in experiments using anaesthesia with α-chloralose (Masamoto et al., 2007). A more careful consideration of the pre-existing literature and more extensive consultation with experts in the field may have yielded the same conclusions as this thesis without having to perform the experiments.

A substantial amount of the time used to produce this thesis was occupied with formulating and refining the spatial normalization procedure demonstrated in Chapter 3. Originally this was not supposed to occupy a large amount of time; the majority of time was to be devoted to using MEMRI to investigate the mechanisms of energy balance. A more effective use of time may have been to collaborate with experts in fMRI analysis software who may have been able to more efficiently adapt the pre-existing fMRI analysis suites to MEMRI timecourses. This would have freed up time for such activities as increasing the sample sizes used in the experiments here, or as mentioned before, using MEMRI to investigate the mechanisms of energy balance.

5.3 Future Work and Prospects for Animal fMRI

The ideal scenario for functional MRI is to be able to observe neuronal activity in the whole brain at high temporal and spatial resolution with minimal intervention and without bias.

Improving spatial and temporal resolution is conceptually relatively simple. The MR acquisition protocols used in fMRI are no different to those used in other areas of MR. Hence any general developments made in MR sequence design or hardware such as parallel imaging (Pruessmann et al., 1999) can be applied to fMRI.

Minimal intervention is a greater problem. It is difficult to conceive how MRI could operate on freely-moving animals, so they have to be immobilised. This effectively means anaesthesia since it is much less stressful than the alternatives of physical restraint or neuromuscular blockade (Peeters et al., 2001). Anaesthesia of course alters neuronal activity (Franks, 2008), so we now have a compromised situation where our tool of observation is substantially affecting the situation it is meant to be observing. Unfortunately there are no known ways out of this conundrum, aside from using the static MEMRI method described in Chapter 2, but which has no temporal resolution. It just has to be hoped that anaesthesia is not a substantial confound. This is conceivable, since anaesthesia can be likened to sleep (Franks, 2008), and many neuronal processes operate during sleep reasonably close to how they would during unconsciousness. For MEMRI there is an intervention problem additional to anaesthesia - $MnCl_2$ toxicity. As with anaesthesia one can hope that this is not such a substantial confound as to make any experiments using it fatally flawed. However, unlike with the anaesthesia confound there is a conceivable solution to this problem- finding an alternative to $MnCl_2$ which is much less toxic or not toxic at all. What this agent might be and how it would be developed is not clear though. Such an agent would likely have to permeate both the BBB, plus the various voltage-gated channels for Ca^{2+} Na^+ and K^+ that, depending upon the neuron type, are present and open during action potentials.

The most intractable problem in fMRI is that of bias- no currently available fMRI method measures activity evenly across the brain. There are many underlying causes of this. The most widespread contributor is that there is a great variance in T_1 (Kuo et al., 2005) and T_2 times (Ahrens and Dubowitz, 2001; Grüne et al., 1999a,b; Kuo et al., 2005) across the brain. Hence any given MRI sequence will be unevenly sensitive to signal changes in different brain regions in a manner dependent on the *TR* (in the case of T_1) and *TE* (for T_2) of the sequence used. Fortunately this bias is predictable and can be factored out of images using information from T_1 and T_2 maps. However this tends not to be done due to the resulting signal loss and because appropriate maps acquired at the correct field strength and spatial resolution are not necessarily available.

MEMRI and haemodynamic methods also suffer from their own specific bias problems. In the case of the MEMRI infusion protocol used here, Mn does not enter the brain evenly- it is biased towards the ventricles (Aoki et al., 2004), and so early on in the infusion the detection of changes in neuronal activity is biased towards these regions. There are two ways to solve this problem. The first is to continue the $MnCl_2$ infusion until a steady state of Mn influx and efflux across the brain is reached, and then start fMRI measurements. Exactly how this would be achieved without a toxic overdose is unclear. In addition, in the absence of BBB compromise it may take upwards of 24 hours before such a state is achieved, posing substantial welfare and life support demands. If a less toxic alternative to $MnCl_2$ was available, this solution would be more viable, especially if the agent reached an infusion equilibrium position more rapidly than $MnCl_2$ does. An even better method would use a hypothetical agent whose location stays static but whose relaxivity changes in response to Ca^{2+} concentration. In this case as long as the agent was evenly spread throughout the brain, or the bias in its spread was known, experiments could be conducted soon after anaesthesia induction. Such agents are under active development (Angelovski et al., 2008; Dhingra et al., 2008a,b; Mishra et al., 2008).

Haemodynamic methods suffer bias due to their relatively indirect observation mechanism- under many circumstances the haemodynamic response to neuronal activity can be attenuated, obliterated and/or decoupled- such as in the presence of caffeine (Chen and Parrish, 2009). This in itself is an interesting effect to observe, though it still leaves us with the unsolved problem of how to measure the electrical activity of neurons. An additional problem is that although ideally we want to observe haemodynamics in the capillaries, much of the signal is derived from larger vessels located further away (Lee et al., 1999, 2002), thus shifting the location of any apparent activity change. This can be ameliorated by using higher field strengths and MR sequences that attenuate large vessel signal, though the more stringent hardware requirements and reduced signal means this approach is not widely implemented.

The challenge to fMRI lies in resolving and implementing solutions to all these biases. If they cannot be resolved, fMRI will not be able to give us any more information useful to the neuroscientist than more orthodox methods such as electrophysiology can. Many of the experiments conducted in this thesis can be considered to be attempting to reduce bias, and future work should continue in this direction.

Bibliography

G. K. Aguirre, J. A. Detre, E. Zarahn, and D. C. Alsop. Experimental design and the relative sensitivity of BOLD and perfusion fMRI. *Neuroimage*, 15:488–500, Mar 2002. 41, 103, 110

R. S. Ahima, C. Bjorbaek, S. Osei, and J. S. Flier. Regulation of neuronal and glial proteins by leptin: implications for brain development. *Endocrinology*, 140:2755–2762, Jun 1999. 82

E. T. Ahrens and D. J. Dubowitz. Peripheral somatosensory fMRI in mouse at 11.7 T. *NMR Biomed*, 14:318–324, Aug 2001. 114, 124

G. Angelovski, P. Fouskova, I. Mamedov, S. Canals, E. Toth, and N. K. Logothetis. Smart magnetic resonance imaging agents that sense extracellular calcium fluctuations. *Chembiochem*, 9:1729–1734, Jul 2008. 125

I. Aoki, C. Tanaka, T. Takegami, T. Ebisu, M. Umeda, M. Fukunaga, K. Fukuda, A. C. Silva, A. P. Koretsky, and S. Naruse. Dynamic activity-induced manganese-dependent contrast magnetic resonance imaging (DAIM MRI). *Magn Reson Med*, 48:927–933, Dec 2002. 44, 48, 50

I. Aoki, Y. J. Wu, A. C. Silva, R. M. Lynch, and A. P. Koretsky. In vivo detection of neuroarchitecture in the rodent brain using manganese-enhanced MRI. *Neuroimage*, 22: 1046–1059, Jul 2004. 47, 99, 124

A. Apostolou, L. Saidt, and W. R. Brown. Effect of overnight fasting of young rats on water consumption, body weight, blood sampling, and blood composition. *Lab. Anim. Sci.*, 26: 959–960, Dec 1976. 80

M. Aschner, T. R. Guilarte, J. S. Schneider, and W. Zheng. Manganese: recent advances in understanding its transport and neurotoxicity. *Toxicol. Appl. Pharmacol.*, 221:131–147, Jun 2007. 43, 44, 45

J. Ashburner, J. L. Andersson, and K. J. Friston. High-dimensional image registration using symmetric priors. *Neuroimage*, 9:619–628, Jun 1999. 97

V. C. Austin, A. M. Blamire, K. A. Allers, T. Sharp, P. Styles, P. M. Matthews, and N. R. Sibson. Confounding effects of anesthesia on functional activation in rodent brain: a study of halothane and alpha-chloralose anesthesia. *Neuroimage*, 24:92–100, Jan 2005. 117

M. G. Banaszczyk, A. T. Carlo, V. Millan, A. Lindsey, R. Moss, D. J. Carlo, and S. S. Hendler. Propofol phosphate, a water-soluble propofol prodrug: in vivo evaluation. *Anesth. Analg.*, 95:1285–1292, Nov 2002. 117

W. A. Banks. The source of cerebral insulin. *Eur. J. Pharmacol.*, 490:5–12, Apr 2004. 46

W. A. Banks, A. J. Kastin, W. Huang, J. B. Jaspan, and L. M. Maness. Leptin enters the brain by a saturable system independent of insulin. *Peptides*, 17:305–311, 1996. 46

M. Barth and E. Moser. Proton NMR relaxation times of human blood samples at 1.5 T and implications for functional MRI. *Cell. Mol. Biol. (Noisy-le-grand)*, 43:783–791, Jul 1997. 42

C. F. Beckmann and S. M. Smith. Probabilistic independent component analysis for functional magnetic resonance imaging. *IEEE Trans Med Imaging*, 23:137–152, Feb 2004. 89, 91

C. F. Beckmann and S. M. Smith. Tensorial extensions of independent component analysis for multisubject FMRI analysis. *Neuroimage*, 25:294–311, Mar 2005. 89, 91, 99

J. W. Belliveau, D. N. Kennedy, R. C. McKinstry, B. R. Buchbinder, R. M. Weisskoff, M. S. Cohen, J. M. Vevea, T. J. Brady, and B. R. Rosen. Functional mapping of the human visual cortex by magnetic resonance imaging. *Science*, 254:716–719, Nov 1991. 39

Y. Benjamini and Y. Hochberg. Controlling the false discovery rate: a practical and powerful approach to multiple testing. *Journal of the Royal Statistical Society, Series B*, 57:289–300, 1995. 90

J. Bolinder, D. A. Kerckhoffs, E. Moberg, E. Hagstrm-Toft, and P. Arner. Rates of skeletal muscle and adipose tissue glycerol release in nonobese and obese subjects. *Diabetes*, 49: 797–802, May 2000. 39

G. A. Bray and D. A. York. Hypothalamic and genetic obesity in experimental animals: an autonomic and endocrine hypothesis. *Physiol. Rev.*, 59:719–809, Jul 1979. 55, 73, 82

D. Burdakov, S. M. Luckman, and A. Verkhratsky. Glucose-sensing neurons of the hypothalamus. *Philos. Trans. R. Soc. Lond., B, Biol. Sci.*, 360:2227–2235, Dec 2005. 20

K. R. Burnett, E. J. Goldstein, G. L. Wolf, S. Sen, and A. C. Mamourian. The oral administration of MnCl2: a potential alternative to IV injection for tissue contrast enhancement in magnetic resonance imaging. *Magn Reson Imaging*, 2:307–314, 1984. 44

R. F. Busse. Flip angle calculation for consistent contrast in spoiled gradient echo imaging. *Magn Reson Med*, 53:977–980, Apr 2005. 36

A. A. Butler and R. D. Cone. Knockout models resulting in the development of obesity. *Trends Genet.*, 17:S50–54, Oct 2001. 22

R. B. Buxton, E. C. Wong, and L. R. Frank. Dynamics of blood flow and oxygenation changes during brain activation: the balloon model. *Magn Reson Med*, 39:855–864, Jun 1998. 42

L. A. Campfield, F. J. Smith, Y. Guisez, R. Devos, and P. Burn. Recombinant mouse OB protein: evidence for a peripheral signal linking adiposity and central neural networks. *Science*, 269: 546–549, Jul 1995. 82

O. B. Chaudhri, J. R. Parkinson, Y. T. Kuo, M. R. Druce, A. H. Herlihy, J. D. Bell, W. S. Dhillo, S. A. Stanley, M. A. Ghatei, and S. R. Bloom. Differential hypothalamic neuronal activation following peripheral injection of GLP-1 and oxyntomodulin in mice detected by manganese-enhanced magnetic resonance imaging. *Biochem. Biophys. Res. Commun.*, 350: 298–306, Nov 2006. 49, 50, 51, 53, 56, 62, 68, 81, 122

X. J. Chen, N. Kovacevic, N. J. Lobaugh, J. G. Sled, R. M. Henkelman, and J. T. Henderson. Neuroanatomical differences between mouse strains as shown by high-resolution 3D MRI. *Neuroimage*, 29:99–105, Jan 2006. 86, 97

Y. Chen and T. B. Parrish. Caffeine dose effect on activation-induced BOLD and CBF responses. *Neuroimage*, 46:577–583, Jul 2009. 125

Y. C. Chen, J. B. Mandeville, T. V. Nguyen, A. Talele, F. Cavagna, and B. G. Jenkins. Improved mapping of pharmacologically induced neuronal activation using the IRON technique with superparamagnetic blood pool agents. *J Magn Reson Imaging*, 14:517–524, Nov 2001. 41, 110, 117

J. O. Cleary, A. N. Price, D. L. Thomas, P. J. Scambler, V. Kyriakopoulou, K. McCue, J. E. Schneider, R. J. Ordidge, and M. F. Lythgoe. Cardiac phenotyping in ex vivo murine embryos using microMRI. *NMR Biomed*, 22:857–866, Jul 2009. 81

D. A. Cory, D. J. Schwartzentruber, and B. H. Mock. Ingested manganese chloride as a contrast agent for magnetic resonance imaging. *Magn Reson Imaging*, 5:65–70, 1987. 44

R. W. Cox. AFNI: software for analysis and visualization of functional magnetic resonance neuroimages. *Comput. Biomed. Res.*, 29:162–173, Jun 1996. 48, 88

R. W. Cox, J. Ashburner, H. Breman, K. Fissell, C. Haselgrove, C. J. Holmes, J. L. Lancaster, D. E. Rex, S. M. Smith, J. B. Woodward, and S. C. Strother. A (Sort of) New Image Data Format Standard: NIfTI-1. In *Human Brain Mapping*, 2004. 58, 105, 106

M. J. Crawley. *Statistics: An Introduction Using R.* John Wiley & Sons, 1st edition, 2005. 122

J. Crossgrove and W. Zheng. Manganese toxicity upon overexposure. *NMR Biomed*, 17: 544–553, Dec 2004. 45

H. F. Cserr, M. DePasquale, C. Nicholson, C. S. Patlak, K. D. Pettigrew, and M. E. Rice. Extracellular volume decreases while cell volume is maintained by ion uptake in rat brain during acute hypernatremia. *J. Physiol. (Lond.)*, 442:277–295, Oct 1991. 80

Department of Health. Health Survey for England. Technical report, Department of Health, 2004. 19

K. Dhingra, P. Fouskov, G. Angelovski, M. E. Maier, N. K. Logothetis, and E. Tth. Towards extracellular Ca2+ sensing by MRI: synthesis and calcium-dependent 1H and 17O relaxation studies of two novel bismacrocyclic Gd3+ complexes. *J. Biol. Inorg. Chem.*, 13:35–46, Jan 2008a. 125

K. Dhingra, M. E. Maier, M. Beyerlein, G. Angelovski, and N. K. Logothetis. Synthesis and characterization of a smart contrast agent sensitive to calcium. *Chem. Commun. (Camb.)*, pages 3444–3446, Aug 2008b. 125

A. E. Dorr, J. P. Lerch, S. Spring, N. Kabani, and R. M. Henkelman. High resolution three-dimensional brain atlas using an average magnetic resonance image of 40 adult C57Bl/6J mice. *Neuroimage*, 42:60–69, Aug 2008. 61, 88, 89, 98, 106

P. Drapeau and D. A. Nachshen. Manganese fluxes and manganese-dependent neurotransmitter release in presynaptic nerve endings isolated from rat brain. *J. Physiol. (Lond.)*, 348:493–510, Mar 1984. 43

T. Q. Duong, D. S. Kim, K. Uurbil, and S. G. Kim. Spatiotemporal dynamics of the BOLD fMRI signals: toward mapping submillimeter cortical columns using the early negative response. *Magn Reson Med*, 44:231–242, Aug 2000a. 43, 104

T. Q. Duong, A. C. Silva, S. P. Lee, and S. G. Kim. Functional MRI of calcium-dependent synaptic activity: cross correlation with CBF and BOLD measurements. *Magn Reson Med*, 43:383–392, Mar 2000b. 44, 50

T. Q. Duong, E. Yacoub, G. Adriany, X. Hu, K. Ugurbil, and S. G. Kim. Microvascular BOLD contribution at 4 and 7 T in the human brain: gradient-echo and spin-echo fMRI with suppression of blood effects. *Magn Reson Med*, 49:1019–1027, Jun 2003. 43, 115

J. H. Duyn, C. T. Moonen, G. H. van Yperen, R. W. de Boer, and P. R. Luyten. Inflow versus deoxyhemoglobin effects in BOLD functional MRI using gradient echoes at 1.5 T. *NMR Biomed*, 7:83–88, Mar 1994. 43, 115

G. Elizondo, C. J. Fretz, D. D. Stark, S. M. Rocklage, S. C. Quay, D. Worah, Y. M. Tsang, M. C. Chen, and J. T. Ferrucci. Preclinical evaluation of MnDPDP: new paramagnetic hepatobiliary contrast agent for MR imaging. *Radiology*, 178:73–78, Jan 1991. 45

J. K. Elmquist, C. F. Elias, and C. B. Saper. From lesions to leptin: hypothalamic control of food intake and body weight. *Neuron*, 22:221–232, Feb 1999. 19

I. S. Farooqi, S. A. Jebb, G. Langmack, E. Lawrence, C. H. Cheetham, A. M. Prentice, I. A. Hughes, M. A. McCamish, and S. O'Rahilly. Effects of recombinant leptin therapy in a child with congenital leptin deficiency. *N. Engl. J. Med.*, 341:879–884, Sep 1999. 22

M. P. Federle, J. L. Chezmar, D. L. Rubin, J. C. Weinreb, P. C. Freeny, R. C. Semelka, J. J. Brown, J. A. Borello, J. K. Lee, R. Mattrey, A. H. Dachman, S. Saini, B. Harmon, M. Fenstermacher, R. E. Pelsang, S. E. Harms, D. G. Mitchell, H. H. Halford, M. W. Anderson, C. D. Johnson, I. R. Francis, J. G. Bova, P. J. Kenney, D. L. Klippenstein, G. S. Foster, and D. A. Turner. Safety and efficacy of mangafodipir trisodium (MnDPDP) injection for hepatic MRI in adults: results of the U.S. multicenter phase III clinical trials (safety). *J Magn Reson Imaging*, 12:186–197, Jul 2000. 45

P. A. Flecknell. *Laboratory animal anaesthesia : a practical introduction for research workers and technicians*. Academic Press, 2nd edition, 1996. 88, 104, 115

D. Fornasiero, J. C. Bellen, R. J. Baker, and B. E. Chatterton. Paramagnetic complexes of manganese(II), iron(III), and gadolinium(III) as contrast agents for magnetic resonance imaging. The influence of stability constants on the biodistribution of radioactive aminopolycarboxylate complexes. *Invest Radiol*, 22:322–327, Apr 1987. 44

P. T. Fox, M. A. Mintun, E. M. Reiman, and M. E. Raichle. Enhanced detection of focal brain responses using intersubject averaging and change-distribution analysis of subtracted PET images. *J. Cereb. Blood Flow Metab.*, 8:642–653, Oct 1988. 48, 84, 96

J. Frahm, K. D. Merboldt, W. Hnicke, A. Kleinschmidt, and H. Boecker. Brain or vein–oxygenation or flow? On signal physiology in functional MRI of human brain activation. *NMR Biomed*, 7:45–53, Mar 1994. 43, 115

J. Frahm, J. Baudewig, K. Kallenberg, A. Kastrup, K. D. Merboldt, and P. Dechent. The post-stimulation undershoot in BOLD fMRI of human brain is not caused by elevated cerebral blood volume. *Neuroimage*, 40:473–481, Apr 2008. 42

N. P. Franks. General anaesthesia: from molecular targets to neuronal pathways of sleep and arousal. *Nat. Rev. Neurosci.*, 9:370–386, May 2008. 52, 123, 124

J. M. Friedman. Modern science versus the stigma of obesity. *Nat. Med.*, 10:563–569, Jun 2004. 19

K. J. Friston. Testing for anatomically specified regional effects. *Hum Brain Mapp*, 5:133–136, 1997. 90

K. J. Friston, C. D. Frith, P. F. Liddle, and R. S. Frackowiak. Comparing functional (PET) images: the assessment of significant change. *J. Cereb. Blood Flow Metab.*, 11:690–699, Jul 1991. 48, 84, 97

K. J. Friston, J. Ashburner, C. D. Frith, J. B. Poline, J. D. Heather, and R. S. J. Frackowiak. Spatial registration and normalization of images. *Hum. Brain Mapp.*, 3:165–189, 1995a. 48, 84, 97

K. J. Friston, A. P. Holmes, K. J. Worsley, J. B. Poline, C. D. Frith, and R. S. J. Frackowiak. Statistical Parametric Maps in Functional Imaging: A General Linear Approach. *Hum. Brain Mapp.*, 2:189–210, 1995b. 48, 84, 97

J. S. Gati, R. S. Menon, K. Ugurbil, and B. K. Rutt. Experimental determination of the BOLD field strength dependence in vessels and tissue. *Magn Reson Med*, 38:296–302, Aug 1997. 43

C. E. Gavin, K. K. Gunter, and T. E. Gunter. Manganese and calcium efflux kinetics in brain mitochondria. Relevance to manganese toxicity. *Biochem. J.*, 266:329–334, Mar 1990. 47

C. E. Gavin, K. K. Gunter, and T. E. Gunter. Mn2+ sequestration by mitochondria and inhibition of oxidative phosphorylation. *Toxicol. Appl. Pharmacol.*, 115:1–5, Jul 1992. 47

C. R. Genovese, N. A. Lazar, and T. Nichols. Thresholding of statistical maps in functional neuroimaging using the false discovery rate. *Neuroimage*, 15:870–878, Apr 2002. 90

C. F. Geraldes, A. D. Sherry, R. D. Brown, and S. H. Koenig. Magnetic field dependence of solvent proton relaxation rates induced by Gd3+ and Mn2+ complexes of various polyaza macrocyclic ligands: implications for NMR imaging. *Magn Reson Med*, 3:242–250, Apr 1986. 44

A. P. Goldstone. The hypothalamus, hormones, and hunger: alterations in human obesity and illness. *Prog. Brain Res.*, 153:57–73, 2006. 23

A. Gozzi, L. Ceolin, A. Schwarz, T. Reese, S. Bertani, V. Crestan, and A. Bifone. A multimodality investigation of cerebral hemodynamics and autoregulation in pharmacological MRI. *Magn Reson Imaging*, 25:826–833, Jul 2007. 118, 119

A. Gozzi, A. J. Schwarz, V. Crestan, T. Tsetsenis, E. Audero, L. Lo Iacono, C. T. Gross, and A. Bifone. Linking genes to brain function: expression of serotonin 5-HT1A receptors in specific neuronal populations results in divergent phMRI responses to the selective agonist 8-OH-DPAT. In *Proceedings of the International Society for Magnetic Resonance in Medicine*, 2008. 114, 119

M. Grüne, F. Pillekamp, W. Schwindt, and M. Hoehn. Gradient echo time dependence and quantitative parameter maps for somatosensory activation in rats at 7 T. *Magn Reson Med*, 42:118–126, Jul 1999a. 124

M. Grüne, F. A. van Dorsten, W. Schwindt, L. Olh, and M. Hoehn. Quantitative T*(2) and T'(2) maps during reversible focal cerebral ischemia in rats: separation of blood oxygenation from nonsusceptibility-based contributions. *Magn Reson Med*, 42:1027–1032, Dec 1999b. 124

H. Gu, E. A. Stein, and Y. Yang. Nonlinear responses of cerebral blood volume, blood flow and blood oxygenation signals during visual stimulation. *Magn Reson Imaging*, 23:921–928, Nov 2005. 42

H. Gu, H. Lu, F. Q. Ye, E. A. Stein, and Y. Yang. Noninvasive quantification of cerebral blood volume in humans during functional activation. *Neuroimage*, 30:377–387, Apr 2006. 41

J. L. Halaas, K. S. Gajiwala, M. Maffei, S. L. Cohen, B. T. Chait, D. Rabinowitz, R. L. Lallone, S. K. Burley, and J. M. Friedman. Weight-reducing effects of the plasma protein encoded by the obese gene. *Science*, 269:543–546, Jul 1995. 82

T. J. Hallam and T. J. Rink. Agonists stimulate divalent cation channels in the plasma membrane of human platelets. *FEBS Lett.*, 186:175–179, Jul 1985. 43

A. Hammers, M. J. Koepp, R. Hurlemann, M. Thom, M. P. Richardson, D. J. Brooks, and J. S. Duncan. Abnormalities of grey and white matter [11C]flumazenil binding in temporal lobe epilepsy with normal MRI. *Brain*, 125:2257–2271, Oct 2002. 80

A. Hammers, M. J. Koepp, M. P. Richardson, R. Hurlemann, D. J. Brooks, and J. S. Duncan. Grey and white matter flumazenil binding in neocortical epilepsy with normal MRI. A PET study of 44 patients. *Brain*, 126:1300–1318, Jun 2003. 80

E. H. Haselhoff. Optimization of flip angle for T1 dependent contrast: a closed form solution. *Magn Reson Med*, 38:518–519, Sep 1997. 36

R. A. Heckemann, J. V. Hajnal, P. Aljabar, D. Rueckert, and A. Hammers. Automatic anatomical brain MRI segmentation combining label propagation and decision fusion. *Neuroimage*, 33:115–126, Oct 2006. 97

J. P. Herman, M. M. Ostrander, N. K. Mueller, and H. Figueiredo. Limbic system mechanisms of stress regulation: hypothalamo-pituitary-adrenocortical axis. *Prog. Neuropsychopharmacol. Biol. Psychiatry*, 29:1201–1213, Dec 2005. 64, 73

A. H. Hielscher. Optical tomographic imaging of small animals. *Curr. Opin. Biotechnol.*, 16: 79–88, Feb 2005. 21

G. E. Hoffman, W. S. Lee, M. S. Smith, R. Abbud, M. M. Roberts, A. G. Robinson, and J. G. Verbalis. c-Fos and Fos-related antigens as markers for neuronal activity: perspectives from neuroendocrine systems. *NIDA Res. Monogr.*, 125:117–133, 1993a. 21

G. E. Hoffman, M. S. Smith, and J. G. Verbalis. c-Fos and related immediate early gene products as markers of activity in neuroendocrine systems. *Front Neuroendocrinol*, 14:173–213, Jul 1993b. 21

F. G. Hoogenraad, P. J. Pouwels, M. B. Hofman, J. R. Reichenbach, M. Sprenger, and E. M. Haacke. Quantitative differentiation between BOLD models in fMRI. *Magn Reson Med*, 45: 233–246, Feb 2001. 43, 115

M. S. Huda, J. P. Wilding, and J. H. Pinkney. Gut peptides and the regulation of appetite. *Obes Rev*, 7:163–182, May 2006. 20

F. Hyder, K. L. Behar, M. A. Martin, A. M. Blamire, and R. G. Shulman. Dynamic magnetic resonance imaging of the rat brain during forepaw stimulation. *J. Cereb. Blood Flow Metab.*, 14:649–655, Jul 1994. 115

F. Hyder, D. L. Rothman, and R. G. Shulman. Total neuroenergetics support localized brain activity: implications for the interpretation of fMRI. *Proc. Natl. Acad. Sci. U.S.A.*, 99: 10771–10776, Aug 2002. 115

A. M. Ingalls, M. M. Dickie, and G. D. Snell. Obese, a new mutation in the house mouse. *J. Hered.*, 41:317–318, Dec 1950. 55, 73

P. A. Jansson, A. Larsson, U. Smith, and P. Lnnroth. Glycerol production in subcutaneous adipose tissue in lean and obese humans. *J. Clin. Invest.*, 89:1610–1617, May 1992. 39

P. A. Jansson, A. Larsson, and P. N. Lnnroth. Relationship between blood pressure, metabolic variables and blood flow in obese subjects with or without non-insulin-dependent diabetes mellitus. *Eur. J. Clin. Invest.*, 28:813–818, Oct 1998. 39

B. G. Jenkins, Y.-C. I. Chen, and J. B. Mandeville. *Biomedical imaging in experimental neuroscience*, chapter Pharmacological Magnetic Resonance Imaging (phMRI). CRC Press, 1993. 41, 42, 110

Y. S. Kang and J. C. Gore. Studies of tissue NMR relaxation enhancement by manganese. Dose and time dependences. *Invest Radiol*, 19:399–407, 1984. 44

R. P. Kennan, B. E. Scanley, R. B. Innis, and J. C. Gore. Physiological basis for BOLD MR signal changes due to neuronal stimulation: separation of blood volume and magnetic susceptibility effects. *Magn Reson Med*, 40:840–846, Dec 1998. 117

A. Klein, J. Andersson, B. A. Ardekani, J. Ashburner, B. Avants, M. C. Chiang, G. E. Christensen, D. L. Collins, J. Gee, P. Hellier, J. H. Song, M. Jenkinson, C. Lepage, D. Rueckert, P. Thompson, T. Vercauteren, R. P. Woods, J. J. Mann, and R. V. Parsey. Evaluation of 14 nonlinear deformation algorithms applied to human brain MRI registration. *Neuroimage*, 46:786–802, Jul 2009. 97

D. Kleinfeld and O. Griesbeck. From art to engineering? The rise of in vivo mammalian electrophysiology via genetically targeted labeling and nonlinear imaging. *PLoS Biol.*, 3: e355, Oct 2005. 21

M. Kojima and K. Kangawa. Ghrelin: structure and function. *Physiol. Rev.*, 85:495–522, Apr 2005. 20, 76, 103, 107

M. Kojima, H. Hosoda, Y. Date, M. Nakazato, H. Matsuo, and K. Kangawa. Ghrelin is a growth-hormone-releasing acylated peptide from stomach. *Nature*, 402:656–660, Dec 1999. 22, 76, 103

N. Kovacevi, J. T. Henderson, E. Chan, N. Lifshitz, J. Bishop, A. C. Evans, R. M. Henkelman, and X. J. Chen. A three-dimensional MRI atlas of the mouse brain with estimates of the average and variability. *Cereb. Cortex*, 15:639–645, May 2005. 86, 97

M. L. Kringelbach. Food for thought: hedonic experience beyond homeostasis in the human brain. *Neuroscience*, 126:807–819, 2004. 23

G. Krüger, A. Kastrup, and G. H. Glover. Neuroimaging at 1.5 T and 3.0 T: comparison of oxygenation-sensitive magnetic resonance imaging. *Magn Reson Med*, 45:595–604, Apr 2001. 43

Y. T. Kuo, A. H. Herlihy, P. W. So, K. K. Bhakoo, and J. D. Bell. In vivo measurements of T1 relaxation times in mouse brain associated with different modes of systemic administration of manganese chloride. *J Magn Reson Imaging*, 21:334–339, Apr 2005. 53, 66, 124

Y. T. Kuo, A. H. Herlihy, P. W. So, and J. D. Bell. Manganese-enhanced magnetic resonance imaging (MEMRI) without compromise of the blood-brain barrier detects hypothalamic neuronal activity in vivo. *NMR Biomed*, 19:1028–1034, Dec 2006. 16, 49, 50, 51, 53, 56, 62, 64, 68, 72, 79, 80, 81, 88, 93, 95, 122

Y. T. Kuo, J. R. Parkinson, O. B. Chaudhri, A. H. Herlihy, P. W. So, W. S. Dhillo, C. J. Small, S. R. Bloom, and J. D. Bell. The temporal sequence of gut peptide CNS interactions tracked in vivo by magnetic resonance imaging. *J. Neurosci.*, 27:12341–12348, Nov 2007. 15, 49, 50, 51, 53, 54, 56, 62, 68, 72, 76, 81, 103, 105, 107, 122

K. M. Lahti, C. F. Ferris, F. Li, C. H. Sotak, and J. A. King. Comparison of evoked cortical activity in conscious and propofol-anesthetized rats using functional MRI. *Magn Reson Med*, 41:412–416, Feb 1999. 117

S. Lai, A. L. Hopkins, E. M. Haacke, D. Li, B. A. Wasserman, P. Buckley, L. Friedman, H. Meltzer, P. Hedera, and R. Friedland. Identification of vascular structures as a major source of signal contrast in high resolution 2D and 3D functional activation imaging of the motor cortex at 1.5T: preliminary results. *Magn Reson Med*, 30:387–392, Sep 1993. 43, 115

T. K. Lam, R. Gutierrez-Juarez, A. Pocai, and L. Rossetti. Regulation of blood glucose by hypothalamic pyruvate metabolism. *Science*, 309:943–947, Aug 2005. 20

J. H. Lee, A. C. Silva, H. Merkle, and A. P. Koretsky. Manganese-enhanced magnetic resonance imaging of mouse brain after systemic administration of MnCl2: dose-dependent and temporal evolution of T1 contrast. *Magn Reson Med*, 53:640–648, Mar 2005. 46, 68, 81

S. P. Lee, A. C. Silva, K. Ugurbil, and S. G. Kim. Diffusion-weighted spin-echo fMRI at 9.4 T: microvascular/tissue contribution to BOLD signal changes. *Magn Reson Med*, 42:919–928, Nov 1999. 42, 43, 115, 125

S. P. Lee, A. C. Silva, and S. G. Kim. Comparison of diffusion-weighted high-resolution CBF and spin-echo BOLD fMRI at 9.4 T. *Magn Reson Med*, 47:736–741, Apr 2002. 43, 125

J. Licinio, S. Caglayan, M. Ozata, B. O. Yildiz, P. B. de Miranda, F. O'Kirwan, R. Whitby, L. Liang, P. Cohen, S. Bhasin, R. M. Krauss, J. D. Veldhuis, A. J. Wagner, A. M. DePaoli,

S. M. McCann, and M. L. Wong. Phenotypic effects of leptin replacement on morbid obesity, diabetes mellitus, hypogonadism, and behavior in leptin-deficient adults. *Proc. Natl. Acad. Sci. U.S.A.*, 101:4531–4536, Mar 2004. 22

L. Lin, G. Chen, K. Xie, K. A. Zaia, S. Zhang, and J. Z. Tsien. Large-scale neural ensemble recording in the brains of freely behaving mice. *J. Neurosci. Methods*, 155:28–38, Jul 2006. 21

Y. J. Lin and A. P. Koretsky. Manganese ion enhances T1-weighted MRI during brain activation: an approach to direct imaging of brain function. *Magn Reson Med*, 38:378–388, Sep 1997. 44, 46, 48, 50, 53, 75

C. H. Liu, D. N. Greve, G. Dai, J. J. Marota, and J. B. Mandeville. Remifentanil administration reveals biphasic phMRI temporal responses in rat consistent with dynamic receptor regulation. *Neuroimage*, 34:1042–1053, Feb 2007. 105

T. T. Liu and G. G. Brown. Measurement of cerebral perfusion with arterial spin labeling: Part 1. Methods. *J Int Neuropsychol Soc*, 13:517–525, May 2007. 41

I. H. Lorenz, C. Kolbitsch, C. Hrmann, T. J. Luger, M. Schocke, W. Eisner, P. L. Moser, H. Schubert, C. Kremser, and A. Benzer. The influence of nitrous oxide and remifentanil on cerebral hemodynamics in conscious human volunteers. *Neuroimage*, 17:1056–1064, Oct 2002. 110, 112

O. V. Lounasmaa, M. Hmlinen, R. Hari, and R. Salmelin. Information processing in the human brain: magnetoencephalographic approach. *Proc. Natl. Acad. Sci. U.S.A.*, 93:8809–8815, Aug 1996. 21

H. Lu and P. C. van Zijl. Experimental measurement of extravascular parenchymal BOLD effects and tissue oxygen extraction fractions using multi-echo VASO fMRI at 1.5 and 3.0 T. *Magn Reson Med*, 53:808–816, Apr 2005. 43

H. Lu, X. Golay, J. J. Pekar, and P. C. Van Zijl. Functional magnetic resonance imaging based on changes in vascular space occupancy. *Magn Reson Med*, 50:263–274, Aug 2003. 41

H. Lu, C. A. Scholl, Y. Zuo, E. A. Stein, and Y. Yang. Quantifying the blood oxygenation level dependent effect in cerebral blood volume-weighted functional MRI at 9.4T. *Magn Reson Med*, 58:616–621, Sep 2007. 42, 119

V. M. Lukasik and R. J. Gillies. Animal anaesthesia for in vivo magnetic resonance. *NMR Biomed*, 16:459–467, Dec 2003. 116, 117

X. Ma, J. Bruning, and F. M. Ashcroft. Glucagon-like peptide 1 stimulates hypothalamic proopiomelanocortin neurons. *J. Neurosci.*, 27:7125–7129, Jul 2007. 103

N. J. Maandag, D. Coman, B. G. Sanganahalli, P. Herman, A. J. Smith, H. Blumenfeld, R. G. Shulman, and F. Hyder. Energetics of neuronal signaling and fMRI activity. *Proc. Natl. Acad. Sci. U.S.A.*, 104:20546–20551, Dec 2007. 115

C. M. Mack, C. X. Moore, C. M. Jodka, S. Bhavsar, J. K. Wilson, J. A. Hoyt, J. L. Roan, C. Vu, K. D. Laugero, D. G. Parkes, and A. A. Young. Antiobesity action of peripheral exenatide (exendin-4) in rodents: effects on food intake, body weight, metabolic status and side-effect measures. *Int J Obes (Lond)*, 30:1332–1340, Sep 2006. 105, 107

S. Mahankali, Y. Liu, Y. Pu, J. Wang, C. W. Chen, P. T. Fox, and J. H. Gao. In vivo fMRI demonstration of hypothalamic function following intraperitoneal glucose administration in a rat model. *Magn Reson Med*, 43:155–159, Jan 2000. 48

J. B. Mandeville, J. J. Marota, B. E. Kosofsky, J. R. Keltner, R. Weissleder, B. R. Rosen, and R. M. Weisskoff. Dynamic functional imaging of relative cerebral blood volume during rat forepaw stimulation. *Magn Reson Med*, 39:615–624, Apr 1998. 42

J. B. Mandeville, J. J. Marota, C. Ayata, G. Zaharchuk, M. A. Moskowitz, B. R. Rosen, and R. M. Weisskoff. Evidence of a cerebrovascular postarteriole windkessel with delayed compliance. *J. Cereb. Blood Flow Metab.*, 19:679–689, Jun 1999. 42

J. B. Mandeville, B. G. Jenkins, Y. C. Chen, J. K. Choi, Y. R. Kim, D. Belen, C. Liu, B. E. Kosofsky, and J. J. Marota. Exogenous contrast agent improves sensitivity of gradient-echo functional magnetic resonance imaging at 9.4 T. *Magn Reson Med*, 52:1272–1281, Dec 2004. 42, 105, 117, 118, 119

J. B. Mandeville, F. P. Leite, and J. J. Marota. Spin-echo MRI underestimates functional changes in microvascular cerebral blood plasma volume using exogenous contrast agent. *Magn Reson Med*, 58:769–776, Oct 2007. 105, 110, 118

J. J. Marota, J. B. Mandeville, R. M. Weisskoff, M. A. Moskowitz, B. R. Rosen, and B. E. Kosofsky. Cocaine activation discriminates dopaminergic projections by temporal response: an fMRI study in Rat. *Neuroimage*, 11:13–23, Jan 2000. 105

C. Martin and N. R. Sibson. Pharmacological MRI in animal models: a useful tool for 5-HT research? *Neuropharmacology*, 55:1038–1047, Nov 2008. 103, 119

C. Martin, J. Martindale, J. Berwick, and J. Mayhew. Investigating neural-hemodynamic coupling and the hemodynamic response function in the awake rat. *Neuroimage*, 32:33–48, Aug 2006. 42

K. Masamoto, T. Kim, M. Fukuda, P. Wang, and S. G. Kim. Relationship between neural, vascular, and BOLD signals in isoflurane-anesthetized rat somatosensory cortex. *Cereb. Cortex*, 17:942–950, Apr 2007. 117, 123

M. L. McManus, K. B. Churchwell, and K. Strange. Regulation of cell volume in health and disease. *N. Engl. J. Med.*, 333:1260–1266, Nov 1995. 80

D. W. McRobbie, E. A. Moore, M. J. Graves, and M. R. Prince. *MRI: From Picture to Proton*. Cambridge University Press, 1st edition, 2003. 23

U. Meiri and R. Rahamimoff. Neuromuscular transmission: inhibition by manganese ions. *Science*, 176:308–309, Apr 1972. 43

M. H. Mendonça-Dias, E. Gaggelli, and P. C. Lauterbur. Paramagnetic contrast agents in nuclear magnetic resonance medical imaging. *Semin Nucl Med*, 13:364–376, Oct 1983. 44

M. E. Meyer, O. Yu, B. Eclancher, D. Grucker, and J. Chambron. NMR relaxation rates and blood oxygenation level. *Magn Reson Med*, 34:234–241, Aug 1995. 42

A. Mishra, P. Fouskov, G. Angelovski, E. Balogh, A. K. Mishra, N. K. Logothetis, and E. Tth. Facile synthesis and relaxation properties of novel bispolyazamacrocyclic Gd3+ complexes:

an attempt towards calcium-sensitive MRI contrast agents. *Inorg Chem*, 47:1370–1381, Feb 2008. 125

C. T. Montague, I. S. Farooqi, J. P. Whitehead, M. A. Soos, H. Rau, N. J. Wareham, C. P. Sewter, J. E. Digby, S. N. Mohammed, J. A. Hurst, C. H. Cheetham, A. R. Earley, A. H. Barnett, J. B. Prins, and S. O'Rahilly. Congenital leptin deficiency is associated with severe early-onset obesity in humans. *Nature*, 387:903–908, Jun 1997. 22

H. Moreno, F. Hua, T. Brown, and S. Small. Longitudinal mapping of mouse cerebral blood volume with MRI. *NMR Biomed*, 19:535–543, Aug 2006. 114

P. J. Morgane, J. R. Galler, and D. J. Mokler. A review of systems and networks of the limbic forebrain/limbic midbrain. *Prog. Neurobiol.*, 75:143–160, Feb 2005. 64, 73

H. Morita, T. Ogino, Y. Seo, N. Fujiki, K. Tanaka, A. Takamata, S. Nakamura, and M. Murakami. Detection of hypothalamic activation by manganese ion contrasted T(1)-weighted magnetic resonance imaging in rats. *Neurosci. Lett.*, 326:101–104, Jun 2002. 15, 54

G. J. Morton, D. E. Cummings, D. G. Baskin, G. S. Barsh, and M. W. Schwartz. Central nervous system control of food intake and body weight. *Nature*, 443:289–295, Sep 2006. 20

T. Mueggler, D. Baumann, M. Rausch, and M. Rudin. Bicuculline-induced brain activation in mice detected by functional magnetic resonance imaging. *Magn Reson Med*, 46:292–298, Aug 2001. 114

T. Mueggler, C. Sturchler-Pierrat, D. Baumann, M. Rausch, M. Staufenbiel, and M. Rudin. Compromised hemodynamic response in amyloid precursor protein transgenic mice. *J. Neurosci.*, 22:7218–7224, Aug 2002. 114

T. Mueggler, D. Baumann, M. Rausch, M. Staufenbiel, and M. Rudin. Age-dependent impairment of somatosensory response in the amyloid precursor protein 23 transgenic mouse model of Alzheimer's disease. *J. Neurosci.*, 23:8231–8236, Sep 2003. 114

P. Mystkowski, E. Shankland, S. A. Schreyer, R. C. LeBoeuf, R. S. Schwartz, D. E. Cummings, M. Kushmerick, and M. W. Schwartz. Validation of whole-body magnetic resonance spectroscopy as a tool to assess murine body composition. *Int. J. Obes. Relat. Metab. Disord.*, 24:719–724, Jun 2000. 60, 83

T. R. Nagy, D. Krzywanski, J. Li, S. Meleth, and R. Desmond. Effect of group vs. single housing on phenotypic variance in C57BL/6J mice. *Obes. Res.*, 10:412–415, May 2002. 51

G. Nair and T. Q. Duong. Echo-planar BOLD fMRI of mice on a narrow-bore 9.4 T magnet. *Magn Reson Med*, 52:430–434, Aug 2004. 114

K. Narita, F. Kawasaki, and H. Kita. Mn and Mg influxes through Ca channels of motor nerve terminals are prevented by verapamil in frogs. *Brain Res.*, 510:289–295, Mar 1990. 43

J. Neelavalli and E. M. Haacke. A simplified formula for T1 contrast optimization for short-TR steady-state incoherent (spoiled) gradient echo sequences. *Magn Reson Imaging*, 25:1397–1401, Dec 2007. 36

Y. Ni, C. Petr, H. Bosmans, Y. Miao, D. Grant, A. L. Baert, and G. Marchal. Comparison of manganese biodistribution and MR contrast enhancement in rats after intravenous injection of MnDPDP and MnCl2. *Acta Radiol*, 38:700–707, Jul 1997. 51

D. C. Noll, F. E. Boada, and W. F. Eddy. A spectral approach to analyzing slice selection in planar imaging: optimization for through-plane interpolation. *Magn Reson Med*, 38:151–160, Jul 1997. 105

S. Ogawa, T. M. Lee, and B. Barrere. The sensitivity of magnetic resonance image signals of a rat brain to changes in the cerebral venous blood oxygenation. *Magn Reson Med*, 29: 205–210, Feb 1993a. 42, 102

S. Ogawa, R. S. Menon, D. W. Tank, S. G. Kim, H. Merkle, J. M. Ellermann, and K. Ugurbil. Functional brain mapping by blood oxygenation level-dependent contrast magnetic resonance imaging. A comparison of signal characteristics with a biophysical model. *Biophys. J.*, 64: 803–812, Mar 1993b. 43, 102

J. M. Oja, J. Gillen, R. A. Kauppinen, M. Kraut, and P. C. van Zijl. Venous blood effects in spin-echo fMRI of human brain. *Magn Reson Med*, 42:617–626, Oct 1999. 43, 115

C. A. Olman, S. Inati, and D. J. Heeger. The effect of large veins on spatial localization with GE BOLD at 3 T: Displacement, not blurring. *Neuroimage*, 34:1126–1135, Feb 2007. 43, 115

L. Østergaard. Principles of cerebral perfusion imaging by bolus tracking. *J Magn Reson Imaging*, 22:710–717, Dec 2005. 39, 103

D. G. Parkes, R. Pittner, C. Jodka, P. Smith, and A. Young. Insulinotropic actions of exendin-4 and glucagon-like peptide-1 in vivo and in vitro. *Metab. Clin. Exp.*, 50:583–589, May 2001. 103, 107

J. R. Parkinson, O. B. Chaudhri, Y. T. Kuo, B. C. Field, A. H. Herlihy, W. S. Dhillo, M. A. Ghatei, S. R. Bloom, and J. D. Bell. Differential patterns of neuronal activation in the brainstem and hypothalamus following peripheral injection of GLP-1, oxyntomodulin and lithium chloride in mice detected by manganese-enhanced magnetic resonance imaging (MEMRI). *Neuroimage*, 44:1022–1031, Feb 2009. 48, 49, 50, 51, 53, 56, 62, 68, 81, 122

R. G. Pautler. In vivo, trans-synaptic tract-tracing utilizing manganese-enhanced magnetic resonance imaging (MEMRI). *NMR Biomed*, 17:595–601, Dec 2004. 44

R. G. Pautler, A. C. Silva, and A. P. Koretsky. In vivo neuronal tract tracing using manganese-enhanced magnetic resonance imaging. *Magn Reson Med*, 40:740–748, Nov 1998. 44

G. Paxinos and K. B. J. Franklin. *The mouse brain in stereotaxic coordinates*. Elsevier Academic Press, compact 2nd edition, 2004. 23, 53, 95, 106

R. R. Peeters, I. Tindemans, E. De Schutter, and A. Van der Linden. Comparing BOLD fMRI signal changes in the awake and anesthetized rat during electrical forepaw stimulation. *Magn Reson Imaging*, 19:821–826, Jul 2001. 75, 123

N. J. Pelc. Optimization of flip angle for T1 dependent contrast in MRI. *Magn Reson Med*, 29: 695–699, May 1993. 36

M. A. Pelleymounter, M. J. Cullen, M. B. Baker, R. Hecht, D. Winters, T. Boone, and F. Collins. Effects of the obese gene product on body weight regulation in ob/ob mice. *Science*, 269: 540–543, Jul 1995. 82

J. B. Poline, S. C. Strother, G. Dehaene-Lambertz, G. F. Egan, and J. L. Lancaster. Motivation and synthesis of the FIAC experiment: Reproducibility of fMRI results across expert analyses. *Hum Brain Mapp*, 27:351–359, May 2006. 87

K. P. Pruessmann, M. Weiger, M. B. Scheidegger, and P. Boesiger. SENSE: sensitivity encoding for fast MRI. *Magn Reson Med*, 42:952–962, Nov 1999. 123

B. K. Puri, H. J. Lewis, N. Saeed, and N. J. Davey. Volumetric change of the lateral ventricles in the human brain following glucose loading. *Exp. Physiol.*, 84:223–226, Jan 1999. 80

D. Purves. *Neuroscience*. Sinauer Associates, 2nd edition, 2001. 37, 44, 64, 73

W. S. Rasband. ImageJ. National Institutes of Health, 1997-2008. 58, 106

H. E. Raybould. Mechanisms of CCK signaling from gut to brain. *Curr Opin Pharmacol*, 7: 570–574, Dec 2007. 20

F. Razoux, H. Russig, T. Mueggler, C. Baltes, I. M. Mansuy, , and M. Rudin. Early life stress impairs serotonergic neurotransmission specifically in the prefrontal cortex revealed by pharmacological fMRI in mice. In *Proceedings of the International Society for Magnetic Resonance in Medicine*, 2008. 114, 119

D. R. Reed, A. A. Bachmanov, and M. G. Tordoff. Forty mouse strain survey of body composition. *Physiol. Behav.*, 91:593–600, Aug 2007. 51

C. Rorden, H. O. Karnath, and L. Bonilha. Improving lesion-symptom mapping. *J Cogn Neurosci*, 19:1081–1088, Jul 2007. 106

M. Rudin and A. Sauter. Noninvasive determination of regional cerebral blood flow in rats using dynamic imaging with Gd(DTPA). *Magn Reson Med*, 22:32–46, Nov 1991. 39, 102

T. Sakurai, A. Amemiya, M. Ishii, I. Matsuzaki, R. M. Chemelli, H. Tanaka, S. C. Williams, J. A. Richardson, G. P. Kozlowski, S. Wilson, J. R. Arch, R. E. Buckingham, A. C. Haynes, S. A. Carr, R. S. Annan, D. E. McNulty, W. S. Liu, J. A. Terrett, N. A. Elshourbagy, D. J. Bergsma, and M. Yanagisawa. Orexins and orexin receptors: a family of hypothalamic neuropeptides and G protein-coupled receptors that regulate feeding behavior. *Cell*, 92: 573–585, Feb 1998. 22

B. E. Scanley, R. P. Kennan, S. Cannan, P. Skudlarski, R. B. Innis, and J. C. Gore. Functional magnetic resonance imaging of median nerve stimulation in rats at 2.0 T. *Magn Reson Med*, 37:969–972, Jun 1997. 117

A. J. Schwarz, T. Reese, A. Gozzi, and A. Bifone. Functional MRI using intravascular contrast agents: detrending of the relative cerebrovascular (rCBV) time course. *Magn Reson Imaging*, 21:1191–1200, Dec 2003. 15, 42, 54, 118

A. J. Schwarz, B. Whitcher, A. Gozzi, T. Reese, and A. Bifone. Study-level wavelet cluster analysis and data-driven signal models in pharmacological MRI. *J. Neurosci. Methods*, 159: 346–360, Jan 2007. 118

Y. B. Shah and C. A. Marsden. The application of functional magnetic resonance imaging to neuropharmacology. *Curr Opin Pharmacol*, 4:517–521, Oct 2004. 103

R. Sharma, S. Saini, P. R. Ros, P. F. Hahn, W. C. Small, E. E. de Lange, A. E. Stillman, R. R. Edelman, V. M. Runge, E. K. Outwater, M. Morris, and M. Lucas. Safety profile of ultrasmall superparamagnetic iron oxide ferumoxtran-10: phase II clinical trial data. *J Magn Reson Imaging*, 9:291–294, Feb 1999. 42

Q. Shen, H. Ren, and T. Q. Duong. CBF, BOLD, CBV, and CMRO(2) fMRI signal temporal dynamics at 500-msec resolution. *J Magn Reson Imaging*, 27:599–606, Mar 2008. 42

Sigma-Aldrich Company Ltd. Material Safety Data Sheet. Technical report, Sigma-Aldrich Company Ltd., 2006. 45

A. C. Silva, J. H. Lee, I. Aoki, and A. P. Koretsky. Manganese-enhanced magnetic resonance imaging (MEMRI): methodological and practical considerations. *NMR Biomed*, 17:532–543, Dec 2004. 22, 44, 45, 102

A. M. Smith, B. K. Lewis, U. E. Ruttimann, F. Q. Ye, T. M. Sinnwell, Y. Yang, J. H. Duyn, and J. A. Frank. Investigation of low frequency drift in fMRI signal. *Neuroimage*, 9:526–533, May 1999. 117

S. M. Smith. Fast robust automated brain extraction. *Hum Brain Mapp*, 17:143–155, Nov 2002. 87

S. M. Smith, M. Jenkinson, M. W. Woolrich, C. F. Beckmann, T. E. Behrens, H. Johansen-Berg, P. R. Bannister, M. De Luca, I. Drobnjak, D. E. Flitney, R. K. Niazy, J. Saunders, J. Vickers, Y. Zhang, N. De Stefano, J. M. Brady, and P. M. Matthews. Advances in functional and structural MR image analysis and implementation as FSL. *Neuroimage*, 23 Suppl 1: S208–219, 2004. 48, 87, 89

P. W. So, W. S. Yu, Y. T. Kuo, C. Wasserfall, A. P. Goldstone, J. D. Bell, and G. Frost. Impact of resistant starch on body fat patterning and central appetite regulation. *PLoS ONE*, 2:e1309, 2007. 49, 50, 51, 53, 56, 62, 68, 81, 122

A. W. Song, E. C. Wong, S. G. Tan, and J. S. Hyde. Diffusion weighted fMRI at 1.5 T. *Magn Reson Med*, 35:155–158, Feb 1996. 43, 115

G. Soria, D. Wiedermann, C. Justicia, P. Ramos-Cabrer, and M. Hoehn. Reproducible imaging of rat corticothalamic pathway by longitudinal manganese-enhanced MRI (L-MEMRI). *Neuroimage*, 41:668–674, Jul 2008. 47

J. Speakman, C. Hambly, S. Mitchell, and E. Krl. The contribution of animal models to the study of obesity. *Lab. Anim.*, 42:413–432, Oct 2008. 114

M. Spiller, R. D. Brown, S. H. Koenig, and G. L. Wolf. Longitudinal proton relaxation rates in rabbit tissues after intravenous injection of free and chelated Mn2+. *Magn Reson Med*, 8: 293–313, Nov 1988. 51

J. A. Stark, K. E. Davies, S. R. Williams, and S. M. Luckman. Functional magnetic resonance imaging and c-Fos mapping in rats following an anorectic dose of m-chlorophenylpiperazine. *Neuroimage*, 31:1228–1237, Jul 2006. 48

J. A. Stark, S. McKie, K. E. Davies, S. R. Williams, and S. M. Luckman. 5-HT(2C) antagonism blocks blood oxygen level-dependent pharmacological-challenge magnetic resonance imaging signal in rat brain areas related to feeding. *Eur. J. Neurosci.*, 27:457–465, Jan 2008. 48

H. Steinmetz, G. Frst, and H. J. Freund. Variation of perisylvian and calcarine anatomic landmarks within stereotaxic proportional coordinates. *AJNR Am J Neuroradiol*, 11: 1123–1130, 1990. 97

C. A. Steward, C. A. Marsden, M. J. Prior, P. G. Morris, and Y. B. Shah. Methodological considerations in rat brain BOLD contrast pharmacological MRI. *Psychopharmacology (Berl.)*, 180:687–704, Aug 2005. 103, 115

A. Strobel, T. Issad, L. Camoin, M. Ozata, and A. D. Strosberg. A leptin missense mutation associated with hypogonadism and morbid obesity. *Nat. Genet.*, 18:213–215, Mar 1998. 22

L. K. Summers, J. S. Samra, S. M. Humphreys, R. J. Morris, and K. N. Frayn. Subcutaneous abdominal adipose tissue blood flow: variation within and between subjects and relationship to obesity. *Clin. Sci.*, 91:679–683, Dec 1996. 39

E. Tabuchi, T. Yokawa, H. Mallick, T. Inubushi, T. Kondoh, T. Ono, and K. Torii. Spatio-temporal dynamics of brain activated regions during drinking behavior in rats. *Brain Res.*, 951:270–279, Oct 2002. 48

A. Takeda, J. Sawashita, and S. Okada. Manganese concentration in rat brain: manganese transport from the peripheral tissues. *Neurosci. Lett.*, 242:45–48, Feb 1998. 51

The FIL Methods Group. SPM5. The Functional Imaging Laboratory, IoN, UCL, 2005. 48, 88

B. Thirion, P. Pinel, S. Mriaux, A. Roche, S. Dehaene, and J. B. Poline. Analysis of a large fMRI cohort: Statistical and methodological issues for group analyses. *Neuroimage*, 35: 105–120, Mar 2007. 122

P. Trayhurn and C. Bing. Appetite and energy balance signals from adipocytes. *Philos. Trans. R. Soc. Lond., B, Biol. Sci.*, 361:1237–1249, Jul 2006. 20

M. Tschöp, D. L. Smiley, and M. L. Heiman. Ghrelin induces adiposity in rodents. *Nature*, 407:908–913, Oct 2000. 22, 76, 103, 105, 107

R. Turner, A. Howseman, G. E. Rees, O. Josephs, and K. Friston. Functional magnetic resonance imaging of the human brain: data acquisition and analysis. *Exp Brain Res*, 123: 5–12, Nov 1998. 48, 84, 90

M. Ueki, G. Mies, and K. A. Hossmann. Effect of alpha-chloralose, halothane, pentobarbital and nitrous oxide anesthesia on metabolic coupling in somatosensory cortex of rat. *Acta Anaesthesiol Scand*, 36:318–322, May 1992. 115

C. Vaisse, K. Clement, B. Guy-Grand, and P. Froguel. A frameshift mutation in human MC4R is associated with a dominant form of obesity. *Nat. Genet.*, 20:113–114, Oct 1998. 23

N. van Bruggen and T. Roberts. *Biomedical imaging in experimental neuroscience*. CRC Press, 2002. 21, 22, 36

A. Van der Linden, N. Van Camp, P. Ramos-Cabrer, and M. Hoehn. Current status of functional MRI on small animals: application to physiology, pathophysiology, and cognition. *NMR Biomed*, 20:522–545, Aug 2007. 50, 102

V. Van Meir, M. Verhoye, P. Absil, M. Eens, J. Balthazart, and A. Van der Linden. Differential effects of testosterone on neuronal populations and their connections in a sensorimotor brain nucleus controlling song production in songbirds: a manganese enhanced-magnetic resonance imaging study. *Neuroimage*, 21:914–923, Mar 2004. 47

P. C. van Zijl, S. M. Eleff, J. A. Ulatowski, J. M. Oja, A. M. Ulu, R. J. Traystman, and R. A. Kauppinen. Quantitative assessment of blood flow, blood volume and blood oxygenation effects in functional magnetic resonance imaging. *Nat. Med.*, 4:159–167, Feb 1998. 42

R. P. Vertes. Interactions among the medial prefrontal cortex, hippocampus and midline thalamus in emotional and cognitive processing in the rat. *Neuroscience*, 142:1–20, Sep 2006. 64, 73

Y. Z. Wadghiri, J. A. Blind, X. Duan, C. Moreno, X. Yu, A. L. Joyner, and D. H. Turnbull. Manganese-enhanced magnetic resonance imaging (MEMRI) of mouse brain development. *NMR Biomed*, 17:613–619, Dec 2004. 44

Y. X. Wang, S. M. Hussain, and G. P. Krestin. Superparamagnetic iron oxide contrast agents: physicochemical characteristics and applications in MR imaging. *Eur Radiol*, 11:2319–2331, 2001. 119

T. Watanabe, O. Natt, S. Boretius, J. Frahm, and T. Michaelis. In vivo 3D MRI staining of mouse brain after subcutaneous application of MnCl2. *Magn Reson Med*, 48:852–859, Nov 2002. 44

R. Weber, P. Ramos-Cabrer, D. Wiedermann, N. van Camp, and M. Hoehn. A fully noninvasive and robust experimental protocol for longitudinal fMRI studies in the rat. *Neuroimage*, 29: 1303–1310, Feb 2006. 116

D. S. Weigle, T. R. Bukowski, D. C. Foster, S. Holderman, J. M. Kramer, G. Lasser, C. E. Lofton-Day, D. E. Prunkard, C. Raymond, and J. L. Kuijper. Recombinant ob protein reduces feeding and body weight in the ob/ob mouse. *J. Clin. Invest.*, 96:2065–2070, Oct 1995. 82

R. Weissleder, G. Elizondo, J. Wittenberg, C. A. Rabito, H. H. Bengele, and L. Josephson. Ultrasmall superparamagnetic iron oxide: characterization of a new class of contrast agents for MR imaging. *Radiology*, 175:489–493, May 1990. 110, 119

D. B. West, W. A. Prinz, A. A. Francendese, and M. R. Greenwood. Adipocyte blood flow is decreased in obese Zucker rats. *Am. J. Physiol.*, 253:R228–233, Aug 1987. 39

D. S. Williams, J. A. Detre, J. S. Leigh, and A. P. Koretsky. Magnetic resonance imaging of perfusion using spin inversion of arterial water. *Proc. Natl. Acad. Sci. U.S.A.*, 89:212–216, Jan 1992. 41

G. L. Wolf and L. Baum. Cardiovascular toxicity and tissue proton T1 response to manganese injection in the dog and rabbit. *AJR Am J Roentgenol*, 141:193–197, Jul 1983. 45

E. C. Wong, R. B. Buxton, and L. R. Frank. Implementation of quantitative perfusion imaging techniques for functional brain mapping using pulsed arterial spin labeling. *NMR Biomed*, 10:237–249, 1997. 41

World Health Organisation. *Obesity: preventing and managing a global epidemic*, chapter Economic costs of overweight and obesity. World Health Organisation, 2004. 19

K. J. Worsley, S. Marrett, P. Neelin, A. C. Vandal, K. J. Friston, and A. C. Evans. A Unified Statistical Approach for Determining Significant Signals in Images of Cerebral Activation. *Hum. Brain Mapp.*, 4:58–73, 1996. 90

E. X. Wu, K. K. Wong, M. Andrassy, and H. Tang. High-resolution in vivo CBV mapping with MRI in wild-type mice. *Magn Reson Med*, 49:765–770, Apr 2003. 114

K. Wynne and S. R. Bloom. The role of oxyntomodulin and peptide tyrosine-tyrosine (PYY) in appetite control. *Nat Clin Pract Endocrinol Metab*, 2:612–620, Nov 2006. 20

K. Wynne, S. Stanley, B. McGowan, and S. Bloom. Appetite control. *J. Endocrinol.*, 184: 291–318, Feb 2005. 20, 22

F. Xu, N. Liu, I. Kida, D. L. Rothman, F. Hyder, and G. M. Shepherd. Odor maps of aldehydes and esters revealed by functional MRI in the glomerular layer of the mouse olfactory bulb. *Proc. Natl. Acad. Sci. U.S.A.*, 100:11029–11034, Sep 2003. 114

F. Xu, M. Schaefer, I. Kida, J. Schafer, N. Liu, D. L. Rothman, F. Hyder, D. Restrepo, and G. M. Shepherd. Simultaneous activation of mouse main and accessory olfactory bulbs by odors or pheromones. *J. Comp. Neurol.*, 489:491–500, Sep 2005. 114

E. Yacoub, P. F. Van De Moortele, A. Shmuel, and K. Uurbil. Signal and noise characteristics of Hahn SE and GE BOLD fMRI at 7 T in humans. *Neuroimage*, 24:738–750, Feb 2005. 115

Y. Yang, H. Gu, and E. A. Stein. Simultaneous MRI acquisition of blood volume, blood flow, and blood oxygenation information during brain activation. *Magn Reson Med*, 52: 1407–1417, Dec 2004. 42

G. S. Yeo, I. S. Farooqi, S. Aminian, D. J. Halsall, R. G. Stanhope, and S. O'Rahilly. A frameshift mutation in MC4R associated with dominantly inherited human obesity. *Nat. Genet.*, 20:111–112, Oct 1998. 23

T. Yokawa, E. Tabuchi, M. Takezawa, T. Ono, and K. Torii. Recognition and neural plasticity responding to deficient nutrient intake scanned by a functional MRI in the brain of rats with L-lysine deficiency. *Obes. Res.*, 3 Suppl 5:685S–688S, Dec 1995. 48

A. A. Young, B. R. Gedulin, S. Bhavsar, N. Bodkin, C. Jodka, B. Hansen, and M. Denaro. Glucose-lowering and insulin-sensitizing actions of exendin-4: studies in obese diabetic (ob/ob, db/db) mice, diabetic fatty Zucker rats, and diabetic rhesus monkeys (Macaca mulatta). *Diabetes*, 48:1026–1034, May 1999. 103

X. Yu, Y. Z. Wadghiri, D. H. Sanes, and D. H. Turnbull. In vivo auditory brain mapping in mice with Mn-enhanced MRI. *Nat. Neurosci.*, 8:961–968, Jul 2005. 46, 50, 52, 53, 55, 75, 77, 83

X. Yu, D. H. Sanes, O. Aristizabal, Y. Z. Wadghiri, and D. H. Turnbull. Large-scale reorganization of the tonotopic map in mouse auditory midbrain revealed by MRI. *Proc. Natl. Acad. Sci. U.S.A.*, 104:12193–12198, Jul 2007. 46, 50, 52, 53, 55, 75, 83

X. Yu, J. Zou, J. S. Babb, G. Johnson, D. H. Sanes, and D. H. Turnbull. Statistical mapping of sound-evoked activity in the mouse auditory midbrain using Mn-enhanced MRI. *Neuroimage*, 39:223–230, Jan 2008. 46, 48, 50, 52, 53, 55, 75

G. Zaharchuk, J. B. Mandeville, A. A. Bogdanov, R. Weissleder, B. R. Rosen, and J. J. Marota. Cerebrovascular dynamics of autoregulation and hypoperfusion. An MRI study of CBF and changes in total and microvascular cerebral blood volume during hemorrhagic hypotension. *Stroke*, 30:2197–2204, Oct 1999. 118

P. Zaninotto, H. Wardle, E. Stamatkis, J. Mindell, and Head J. Forecasting obesity to 2010. Technical report, National Centre for Social Research and Department of Epidemiology and Public Health at the Royal Free and University College Medical School, 2006. 19

Y. Zhang, R. Proenca, M. Maffei, M. Barone, L. Leopold, and J. M. Friedman. Positional cloning of the mouse obese gene and its human homologue. *Nature*, 372:425–432, Dec 1994. 82